Universität
Rostock
Traditio et Innovatio

Masterarbeit
“Rotor dynamics of a magnetically levitated centrifugal pump impeller in operation using bond graphs”

Rotordynamik eines magnetisch gelagerten Kreiselpumpenlaufrades im Betrieb mittels Bondgraphen

eingereicht am 20.09.2021

von

Nada Abroug | Rostock | nada.abroug@uni-rostock.de

Matrikel-Nr.: 215 200 003

Erstgutachter:
Prof. Dr.-Ing. Frank-Hendrik Wurm
Lehrstuhl für Strömungsmaschinen
Albert-Einstein-Str. 2
18059 Rostock

Zweitgutachter:
Dr.-Ing. Andre Laß
Lehrstuhl für Strömungsmaschinen
Friedrich-Barnewitz-Str. 11
18119 Rostock

https://doi.org/10.18453/rosdok_id00005309

Lehrstuhl für Strömungsmaschinen
Fakultät für Maschinenbau und Schiffstechnik

Acknowledgement

I would like to deeply thank my thesis-mentor Dr.-Ing. Andre Lass for his patience, guidance and supervision throughout this thesis. I am also grateful for the experience I have had as a Hiwi and a student at the institute of Turbomachinery at the university of Rostock.

Contents

Acronyms

AMB	Active magnetic bearing
BDF	Backward differentiation formula
BFF	Body-fixed frame
BW	Backward-whirl
DoF	Degree of Freedom
IF	Inertial frame
EOM	Equations of motion
FW	Forward-whirl
FFT	Fast Fourier-transformation
ODS	Operating deflection shape
VAD	Ventricular-assist device

Nomenclature

d	Damping coefficient
e	Static eccentricity
e_R	Magnetic eccentricity during operation
e_S	Magnetic eccentricity: offset from the stator center
$E(t)$	Energy
$e(t)$	Generalized effort variable
$f(t)$	Generalized flow variable
$F(t), f$	Force
G	Center of gravity of the rigid rotor
i	Electrical current
I_{xx}, I_{yy}, I_{zz}	Main moments of inertia
I_{xx}	Moment of inertia about the x-axis
I_{yy}	Moment of inertia about the y-axis
I_{zz}	Moment of inertia about the z-axis
I_d	Transversal moment of inertia in an axial-symmetric rotor
$\vec{i}, \vec{j}, \vec{k}$	Unitary vectors in the body-fixed frame
$\vec{I}, \vec{J}, \vec{K}$	Unitary vectors in the inertial-frame
k	Stiffness coefficient
L	Angular momentum
L_1, L_2	Distances to the front and back bearings
M	Moment force
m	Mass
M_x	Angular momentum along the x-axis
M_y	Angular momentum along the y-axis

n	Rotational speed
$O-xyz$	Inertial-frame of reference
$O-x_1y_1z_1$	Intermediate frame of reference
$O-x_2y_2z_2$	Intermediate frame of reference
$O-x'y'z'$	Body-fixed frame
p	Linear momentum
$P(t)$	Power
$p(t)$	Generalized momentum
p_0	Initial momentum
$q(t)$	Generalized displacement
q_0	Initial displacement
q	Generalized coordinate
Q	Generalized forces
Q_β	Generalized moment of forces for the body-base translation
Q_r	Generalized forces for the body-base translation
r	Inertial position vector
S	Geometrical center of the rotor
t	Time
t_0	Initial time point
δt	Infinitesimal time span
T	Kinetic energy
T_2	Rotational kinetic energy
v	Translational velocity vector in the inertial-frame
$\dot{v}$	Acceleration vector
v'	Translational velocity in the body-fixed frame
v_s	Translational velocity vector of the body's geometrical center
V	Volume of a rigid body
x_1, x_2, y_1, y_2	Lateral deflections at the bearings
$\dot{x}_1, \dot{x}_2, \dot{y}_1, \dot{y}_2$	Translational velocities at the bearings

x, y, z	Translational displacements in the inertial-frame
$\dot{x}, \dot{x}, \dot{z}$	Translational velocities in the inertial-frame
x', y', z'	Translational displacements in the body-fixed frame
$\dot{x}', \dot{x}', \dot{z}'$	Translational velocities in the body-fixed frame
X_G, Y_G, Z_G	Translational displacements of the center of gravity
$\dot{X}_G, \dot{Y}_G, \dot{Z}_G$	Translational velocities of the center of gravity
$\underline{\mathbf{C}}$	Forces coefficient matrix
$\underline{\mathbf{C}}_t$	Direction cosine matrix
$\underline{\mathbf{D}}$	Damping matrix
$\underline{\mathrm{F}}$	Force vector with reference to the inertial-frame
$\underline{\mathrm{F}}'$	Force vector with reference to the body-fixed frame
$\underline{\mathrm{I}}_0$	Ideal inertia tensor
$\underline{\mathrm{I}}$	Inertia tensor
$\underline{\mathbf{M}}$	Mass matrix
$\underline{\mathbf{R}}$	Rotation matrix
$\underline{\mathbf{T}}$	Transformation matrix
β	Set of Euler angles
$\dot{\beta}$	Set of rate of change of Euler angles
φ, ϑ, ψ	Euler angles
$\dot{\varphi}, \dot{\vartheta}, \dot{\psi}$	The rate of change of the Euler angles
ϕ, θ, ψ	Angular rotation around the x- , y- and z-axes
$\dot{\phi}, \dot{\theta}, \dot{\psi}$	angular velocities around the x- , y- and z-axes
γ	The angle by which the mass imbalance leads the whirling motion
μ	Dimensionless proportionality damping coefficient
Ω	Rotational or spin velocity
ω	Whirl speed
ω_0	Natural-free frequency
ω_c	Critical speed

ω	Rotational velocity in the inertial frame
ω'	Rotational velocity vector in the body-fixed frame
ρ	Density of a rigid body
τ	Tilt angle
τ_x, τ_y, τ_z	Torques acting around the x-, y- and z-axis
$\underline{\tau}$	Torque vector with reference to the inertial-frame
$\underline{\tau'}$	Torque vector with reference to the body-fixed frame

	Unit
Acceleration	m/s^2
Angle	rad
Angular acceleration	rad/s^2
Angular momentum	kgm^2/s
Angular velocity	rad/s
Damping coefficient	kgm^2/s^3
Distance, displacement	m
Electrical current	A
Energy	kgm^2/s^2
Force	kgm/s^2
Linear momentum	kgm/s
Moment of inertia	$kg \cdot m^2$
Power	kgm^2/s^3
Stiffness coefficient	kg/s^2
Time	s
Torque, moment of force	kgm^2/s^2
Translational velocity	m/s

1 Introduction

1.1 Research frame

Rotating machines of all sizes are indispensable in industrial applications. These machines consist mainly of two groups of parts: the rotating elements or rotor consisting of the bearings, the shaft and the rotor blades or disk, and the static supporting structure called in this case the stator. These machines are conceived to function impeccably at their designed operation points and for long durations. In order to achieve this, several design tasks must be performed including the analysis of dynamic behaviour under different operational conditions. Analyzing the dynamic behavior focuses on the rotating structure due to its distinguishing aspects and their ensuing effects. In particular, the out-of-balance (or unbalance) forces and moments, that are present in a spinning rotor due to imminent manufacturing flaws, are the leading cause of unwanted vibrations. These vibrations can result in undesirable events such as causing the rotor blades to bump into the stator. Excessive vibrations can lead to bearings wear and eventually device malfunctions and failure. Rotordynamics analysis aims at inspecting and predicting these events for ultimate design optimisation.

The material and mechanical properties of the shaft and rotor disk are significantly relevant in the study of rotordynamics. The type of the used bearings is also decisive in the observed dynamic behavior. Among the several bearings that are being employed in rotating machines, magnetic bearings come with a great advantage of supporting the rotor without contact to the stator during operation and thus ensuring lower losses due to friction. Despite the high cost, opting for magnetic bearings is on the rise. They are being used in centrifugal compressors and pumps with most concrete applications seen in third-generation ventricular-assist devices (VADs).

Since investigating the dynamic behaviour of these pumps is an imperative design task, numerical simulations come handy to compensate for costly and time-consuming experimental setups especially as the size of the pump decreases. On one hand, many finite-element method or beam theory-based softwares (most knowingly Dyrobes, Comsol Multiphysics, AxStream Rotordynamics) offer packages and modules or are entirely dedicated to the modelling of rotordynamics. Often, these softwares solve implemented rotordyanmics equations based on the specifications and parameters of the investigated rotor model. On the other hand, other softwares provide alternative concepts such as modeling dynamic systems using Bond-graphs. This approach have proven to be a powerful tool to model and solve multidisciplinary systems and problems. Bond-graphs provide a unique way of modelling structure dynamics through a graphical representation based on reducing a complex system into its equivalent lumped-element model. The rotordyanmics related equations are implemented and interpreted through the Bond-Graph equations, and the physics of the system must be captured through distinct and suitable elements of the Bond-Graph. This modeling approach is more compelling and requires also a broad understanding of rotordynamics.

1.2 Research approach and aim

The research presented in this thesis aims at providing a Bond Graph model of a rotor using 20-sim (Controllab Products B.V.). The parameters needed to characterize the rotor are obtained from the actual model[1]. At this first stage of analysis, the pump is dry running. This allows to determine the dynamic behavior by excluding the hydrodynamic forces acting on the rotor blades and the flow induced vibrations. In the core of the assignment, comes the modeling of the gyroscopic effects, which is characteristic in rotordynamics, as well as incorporating the imbalances and thus the unbalance forces and moments. While there are no direct guidelines or instructions provided into Bond-graph modeling of complex rotordynamics, the modeling process is based on literature recommendations primarily from Karnopp *et al.*[2] and work progress in the field presented by Pedersen[12]. Yamamoto *et al.*[10] and Friswell *et al.*[9] were among the principle references to the theory of rotordynamics in this work.
The outcome obtained will then be compared to the provided empirical results in order to assess the correctness and constraints of the Bond Graph modeling. Based on the complexity of the subject and on the selected modeling approach, the following questions, that are tackled along the work, arise:

- Can a magnetically levitated rotor be modeled by means of Bond Graphs?
- Based on comparison with the provided empirical results, to which extent is this modeling of rotordynamics efficient and reliable?
- Is it possible to establish a fundamental Bond Graph scheme for the modeling of dynamics of rotating machines?

---

[1] The rotor analyzed is a component of a magnetically levitated miniature prototype pump. Since it serves as a prototype of a product that is still in development phase, no further or detailed information about it can be disclosed. Nevertheless, this should not affect the understanding of this work in any way.

2 Theoretical framework

2.1 Fundamentals of Bond Graph

In Physics and by definition, the power P (in SI units it is measured in watts (joules per second) or specifically $[Kg \cdot m^2 \cdot s^{-3}]$) is a scalar quantity and accounts for the rate at which work is done or the amount of energy that is transferred or converted over time[1]. It can be noticed that in each field the power is a product of two characteristic variables. The Bond-graph method relies on that and produces a uniform definition of the power using two generalized variables:

- $e(t)$: the effort
- $f(t)$: the flow

In Bond graph, the Power is defined as $P(t) = e(t) \cdot f(t)$ in any field. This is summarized in the following Table 2.1:

Field	Power $P(t)$	Effort $e(t)$	Flow $f(t)$
Electric	$U \cdot i$	U: Voltage	i: electrical current
mechanical:			
translation	$F \cdot v$	F: force	v: linear velocity
rotation	$M \cdot \omega$	M: moment	ω: angular velocity
Hydraulic	$p \cdot \dot{V}$	p: pressure	$\dot{V}$: Volume flow rate
Thermodynamics	$T \cdot S$	T: Temperature	S: Entropy
Chemistry	-	chemical potential	Molar flow
Magnetic	-	Magneto-motive force	flux rate

Table 2.1: Power definitions for different fields and in bond graph.

The Bond graph consists of graphical elements that depict a process or subsystems linked together by lines representing power bonds. By convention, a power bond indicates the direction of power flow and is symbolized using a half arrow such as "⇀". While a full arrow "→" represents rather a transfer of information in form of a signal.

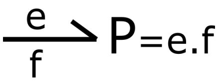

Figure 2.1: Acausal notation of effort and flow for a power bond.

The additional elements that constitute the system in a bond graph depend on the junctions that join these elements and on whether the power:

- flows in or out of the system.
- is generated, dissipated or stored.
- is transformed in another form of energy.

Basic elements and junctions

Basic 1-port elements

Dissipating element
This element is denoted with "**R**" as the first letter in the electrical component the resistor that dissipates energy into heat. The constitutive equation for this element is $e = R \cdot f$, which can also be established through the resistor component in an electrical system $U = R \cdot i \equiv e = R \cdot f$, or a mechanical system with a damper with damping coefficient $d \equiv R$ as $F = d \cdot v \equiv e = R \cdot f$.

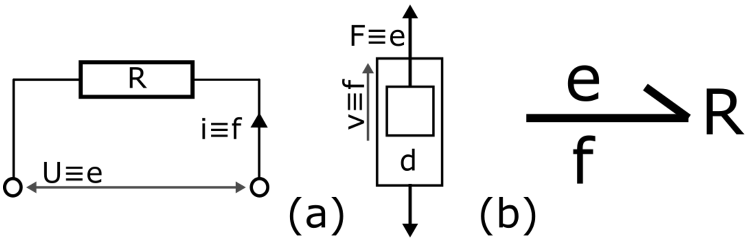

Figure 2.2: R-element: (a) examples and (b) bondgraph acausal representation.

Energy-storing elements
These elements stock the accumulated amount of Power $P(t)$ received over a time t, this is by definition the stored energy $E(t) = \int^{t} P(t)dt = \int^{t} e(t) \cdot f(t)dt$.
To distinguish between the different energy storing elements, two generalized variables are additionally considered:

- The generalized momentum $p(t) = \int_{t_0}^{t} e(t)dt + p_0$
- The generalized displacement $q(t) = \int_{t_0}^{t} f(t)dt + q_0$.

Where p_0 and q_0 are the initial momentum and initial displacement. This leads to determine the constitutive equations of the compliance-element "**C**" and the inertia-element "**I**".
For a compliance-element the constitutive equations for the generalized variables are $e(t) = \frac{1}{C} \cdot q(t) \Rightarrow q(t) = C \cdot e(t)$ and $f(t) = C \cdot \dfrac{\mathrm{d}e(t)}{\mathrm{d}t}$.
C represents the stiffness parameter for a spring element or the capacitance of an electrical capacitor.

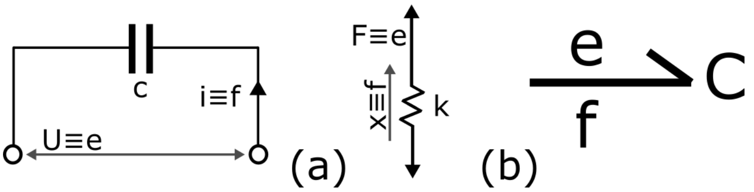

Figure 2.3: C-element: (a) examples and (b) bondgraph acausal representation.

As for an inertia-element, I is the moment of inertia of an object or its constant mass. The generalized momentum $p(t)$ is also defined as $p(t) = \int e(t)dt = I\cdot f(t)$, gives $f(t) = \frac{p(t)}{I}$ and thus $e(t) = \dfrac{\mathrm{d}p}{\mathrm{d}t} = I\cdot\dfrac{\mathrm{d}f(t)}{\mathrm{d}t}$.

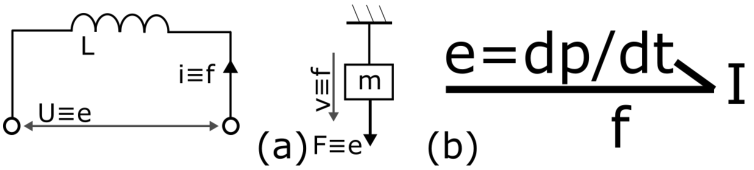

Figure 2.4: I-element: (a) examples and (b) Bond-graph acausal representation.

Source elements

The source elements are divided into source of flow S_f and source of effort S_e. Unlike the **R**-, **C**- and **I**-elements that receive energy and the power bond is directed towards them, source elements deliver energy into the system (for example a force acting on a mass or an electric generator as a source of effort, and a constant current source and volume flow rate as sources of flow) and thus the power bonds are directed outwards. The characteristics of these elements can be summarized in Table 2.2.

Element	Bond-graph representation	Defining general variables
Source of effort	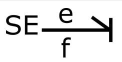	$e(t)$ given $f(t)$ arbitrary
source of flow	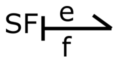	$f(t)$ given $e(t)$ arbitrary

Table 2.2: characteristics of the source elements.

Basic 2-port elements

Transformer element

The power bond flows into the transformer-element (TF-element) and is transformed in an ideal process and flows out into the next power bond. Examples of transformers are electrical transformers or simple gear trains. The constitutive equations are:

$$\begin{aligned} e_1(t)\cdot f_1(t) = e_2(t)\cdot f_2(t) \qquad & \text{where} \\ e_1(t) = m\cdot e_2(t) \quad \text{and} \quad & f_2(t) = m\cdot f_1(t) \end{aligned} \tag{2.1}$$

The constant m is a transformation factor also known as the modulus of the transformer that links the incoming flow to the out-coming flow and the incoming effort to the out-coming effort.

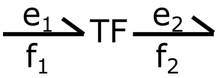

Figure 2.5: Bond-graph acausal representation of a 2-port transformer.

Gyrator element

Through a Gyrator-element the incoming effort and flow are respectively connected to the out-coming flow and effort using a gyrator ratio r. For instance, a DC-motor that converts electrical energy into mechanical energy can be modeled using a GY-element. the constitutive equations are:

$$\begin{aligned} e_1(t)\cdot f_1(t) = e_2(t)\cdot f_2(t) \qquad & \text{where} \\ e_1(t) = r\cdot f_2(t) \quad \text{and} \quad & e_2(t) = r\cdot f_1(t) \end{aligned} \tag{2.2}$$

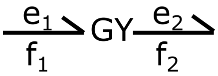

Figure 2.6: Bond-graph acausal representation of a 2-port Gyrator.

Modulated elements

When using the modulator forms of the basic 1-port and 2-port elements, the parameters as well as the ratios or modulus are no longer considered to be constants but depend on several factors and input information that are time dependent and calculated along the progress of the simulation.

Element	Basic designation	Modular form
Resistor	R	MR
Compliance	C	MC
Transformer	TF	MTF
Gyrator	GY	MGY
Source of effort	SE	MSE
Source of flow	SF	MSF

Table 2.3: Basic 1- and 2-port elements and their modular counterparts.

Basic 3-port junctions

When describing a system in Bond graph that is composed of several elements, it is required to couple these elements through coherent networks that correlate the power bonds at a node or an intersection. The elementary form of an intersection associates 3 power bonds and is called a junction.
These junctions do not store or dissipate energy and the following relation applies:

$$e_1 \cdot f_1 + e_2 \cdot f_2 + e_3 \cdot f_3 = 0 \tag{2.3}$$

Which indicates that two types of a 3-bond junction arise: the effort at the node are equal and the flows sum up to zero which is the case of a flow-junction (0-junction), or that the flows at the node are equal and the efforts add up to zero, this is the effort-junctions (1-junction).

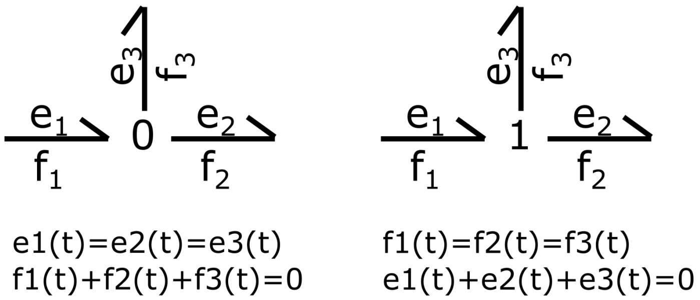

Figure 2.7: 3-port 0- and 1-junctions: acausal bondgraph representation and constitutive equations.

Causality in the power bond

Causality as a notion is the relation between cause and effect dictated in logical sequences. In bond graph modeled system, each element implements a single equation or a set of equations. In order to make use of this modeling approach and coherence, independent system parameters or variables and other system variables that are determined through the system properties must be related. Such information provided by causality is very important in Bond graph and has the following properties[3]:

- The power flow between two points or subsystems is displayed using a half arrow "⇀" as mentioned at the beginning.
- The power flow in the direction of the half arrow is positive.
- The direction of the half arrow indicates only the direction of the effort and flow product: the power.
- Flow and effort have always opposite directions.
- The element can only manipulate one of the generalized variables and receives the other as an information.

- A vertical causality-stroke is added in order to define the direction of the effort.

These properties are coarsely summarized in Figure 2.8

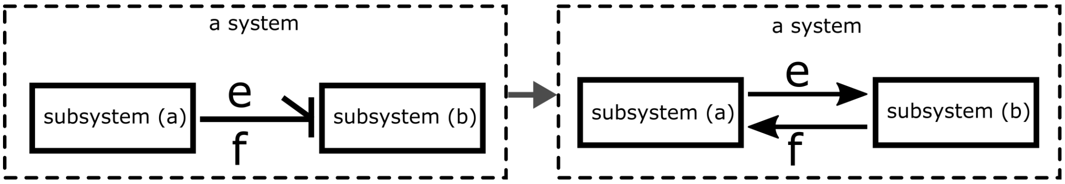

Figure 2.8: Effort-flow causality.

The source of effort and source of flow elements have always the same pre-defined causality display as presented in Table 2.2. For the rest of the basic 1-port elements, it can be opted to two possibilities to define the causality as an integral causality and a differential causality mainly for the energy-storing elements. The R-element dissipates energy thus it does not have a preference and have two even ways to present causality. By denoting $\phi_R = R$, $\phi_R^{-1} = 1/R$ and so on for C and I, the general causal relations are summarized in the next table:

Element	Bond-graph causal representations	General causal relations
Resistor	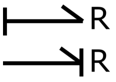	$e(t) = \phi_R(f(t))$ $f(t) = \phi_R^{-1}(e(t))$
Capacitor	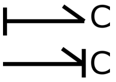	$e = \phi_C^{-1}(\int^t f(t)dt)$ $f = \phi_C \frac{de(t)}{dt}$
Inertia	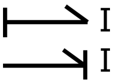	$e = \phi_I \frac{df(t)}{dt}$ $f = \phi_I^{-1}(\int^t e(t)dt)$
Transformer	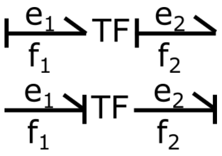	$e_1 = me_2$ and $f_2 = mf_1$ $e_2 = e_1/m$ and $f_1 = f_2/m$
Gyrator	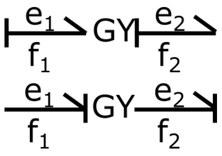	$e_1 = rf_2$ and $e_2 = rf_1$ $f_1 = e_2/r$ and $f_2 = e_1/m$

Table 2.4: Causal forms of 1- and 2-port elements.

A simple example is shortly presented below, Bond Graphs will be used to model a dynamic system that has both a rotational and a translation degree of freedom. The example is illustrated in Figure 2.9. The rigid body has a mass m and a moment of inertia J and is assumed to move only vertically along x and rotate around the center of the body c with an angular velocity $\dot{\varphi}$. A vertical froce $F(t)$ acts vertically upward at the center. At each end, the body has a spring-damper support with stiffness and damping coefficients c_1 and d_1 at point A, and stiffness and damping coefficients c_2 and d_2 at point B. The effect of gravity is omitted.

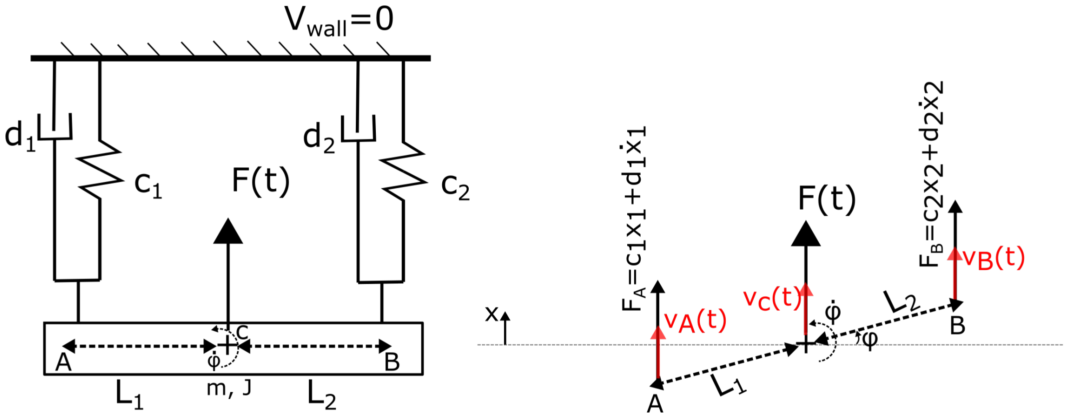

Figure 2.9: Example: the structure and its free-body diagram.

$$\text{At point A}: \; F_A = c_1 \cdot x_1 + d_1 \cdot \dot{x}_1$$
$$\text{At point B}: \; F_B = c_2 \cdot x_2 + d_2 \cdot \dot{x}_2$$

With x_1 and x_2 being the vertical displacement at points A and B.
The forces and moment forces at equilibrium:

$$\uparrow: \; F(t) + F_A + F_B = 0$$
$$\curvearrowleft: \; F_B \cdot L_2 - F_A \cdot L_1 = 0$$

In the inertia-elements, the linear and angular velocities at the body center can be determined:

$$v_c = \frac{p(t)}{m}$$
$$\dot{\varphi} = \frac{L(t)}{J}$$

Where $p(t)$ and $L(t)$ are the linear and angular momenta of the body. Each is directly obtained by using the property $p(t) = \int^t e(t)\,dt$.
In the rigid body, the velocity of any point with distance r from the center c that has the velocity v_c is $v_p = v_c + \dot{\varphi} \times r$. Applying this yields the velocities at point A and B:

$$\dot{x}_1 = v_A = v_c - \dot{\varphi} \cdot L_1$$
$$\dot{x}_2 = v_B = v_c + \dot{\varphi} \cdot L_2$$

This is established, in the Bond-graph model, by using a 0-junction joining the linear velocity at the center to the angular velocity, that was obtained from the inertia-element representing the moment of inertia, through transformer-elements (TF) with moduli $-L_1 cos(\phi(t))$ and $L_2 cos(\phi(t))$. The Bond Graph modeling is summarized and displayed in Figure 2.10.

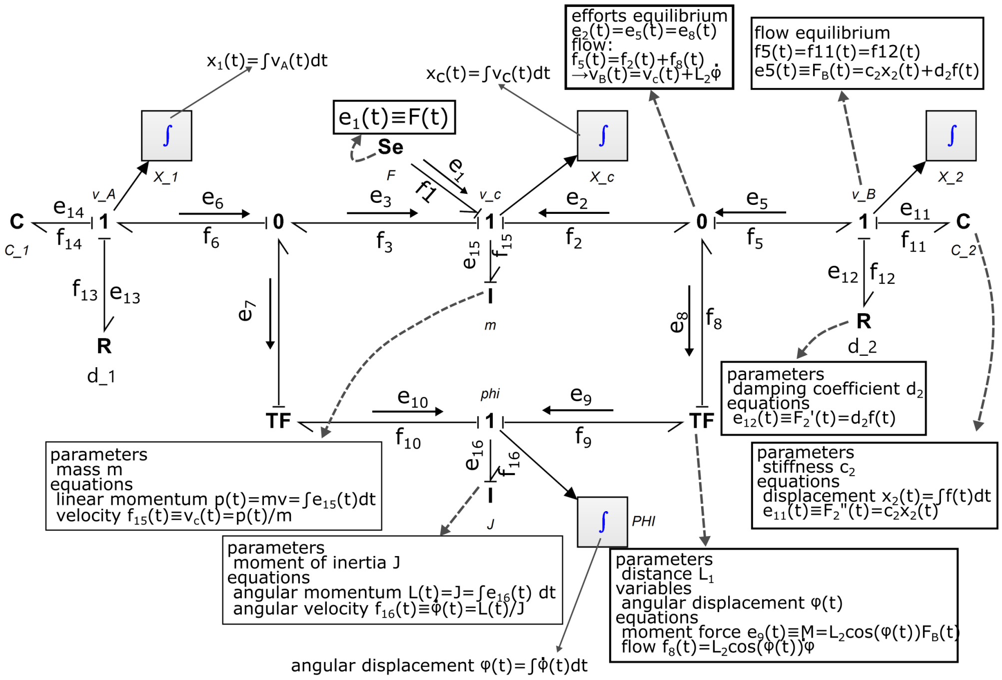

Figure 2.10: Commented Bond-graph model of the provided example.

2.2 Magnetic bearings in rotors

Bearings are the supporting and guiding elements of the rotor and they connect it to the stationary parts of the pump. Magnetic bearings can suspend a rotor without contact to the stator using magnetic forces which reduces the losses due to friction. While they come with high-costs, their applications have more advantages such as operating under high rotational speed, increased tolerance to corrosive agents and low maintenance.
There are two types of magnetic bearings for usage in rotors:

- Passive magnetic bearings (PMB) rely mostly on permanent magnets that levitate a body using attracting or repuslive froces. These permanent magnets have constant stiffness and damping properties.
- Active magnetic bearings (AMB) are electromagnets with an implemented feedback control-loop that allows to adjust the bearings characteristics such as damping and stiffness and thus precisely control the rotor position.

When using a set of magnetic bearings, the fundamental stability limitations described by Earnshaw's theorem (1842) should be satisfied[10], it states "A collection of point charges cannot be maintained in a stable stationary equilibrium configuration solely by the electrostatic interaction of the charges". This means that it is impossible to levitate a rigid body without contact in a static magnetic field produced solely by permanent magnets. Thus, a fully magnetically levitated rotor will require at least one degree of freedom to be actively controlled[4].
Magnetic bearings contribute to the dynamic unabalance in the rotor by causing unbalanced magnetic pull (UMP). UMP appears in electrical machines during operation when the magnetic field linking the rotor and stator is not perfectly symmetric[9]. It manifests by a deviation in the concentricity between the rotor and stator. This unbalance results from the whirling motion or bounce and tilt modes of the rotor relative to the stator. UMP arises also due to a misalignment of the radial bearings facing each other, which contributes to an asymmetric distribution of the magneto-motive forces producing thus a net magnetic force between the rotor and the stator.

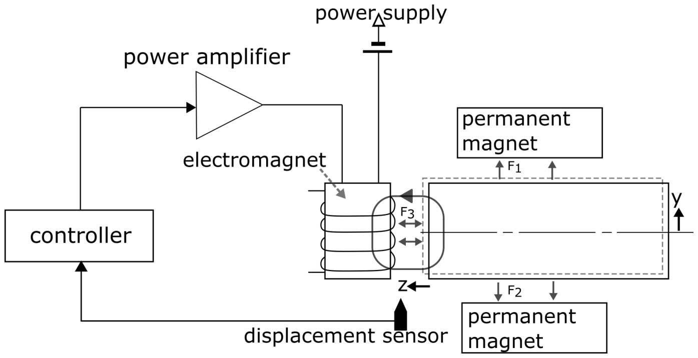

Figure 2.11: Magnetic levitation using 2 PMB and an axial AMB.

Magnetic bearings have a non-linear dynamic behavior that can manifest, for instance, through the non-linearity of the magnetic force to the displacement and coil current, hysteresis of the ferromagnetic core material and delayed actuator responses[5]. In modeling, this non-linearity is usually neglected and the magnetic and electromagnetic forces are linearized about the operating points by being modeled as linear function of the electrical current and the rotor-stator-gap. This linearization is summarized here below based on reference[5].

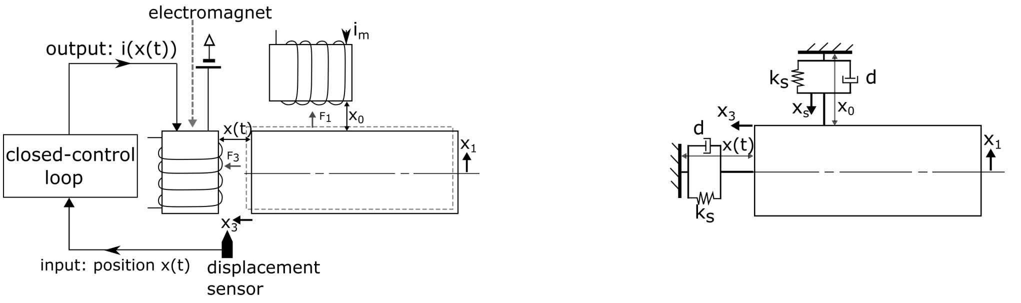

(a) Magnetic levitation. (b) Artificial stiffness and damping analogy.

Figure 2.12: Magnetic force linearization

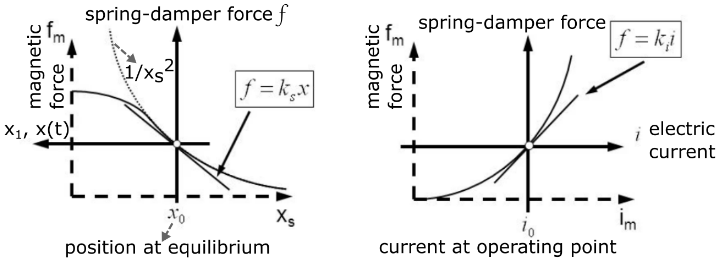

Figure 2.13: Magnetic force linearization at an operating point([5] modified).

The force behavior at an operating point (constant current) is:

$$f\big|_{i_m=i_0} = k_s \cdot x \text{ and } f\big|_{x_s=x_0} = k_i \cdot i \tag{2.4}$$

With $x = -x_s + x_0$ and $i = i_m - i_0$, the open loop equation is $f(x,i) = k_s \cdot x + k_i \cdot i$, and:

$$f(x,i) \equiv f = -k \cdot x - d \cdot \dot{x} = m\ddot{x} \tag{2.5}$$

Applying the same procedure for the closed-loop control, the output electrical current i as a function of the input position $x(t)$ is:

$$i(x) = \frac{-(k+k_s)\cdot x + d \cdot \dot{x}}{k \cdot i} \tag{2.6}$$

By substituting into equation 2.5 and arranging, the free equation of motion for the artificial mass-spring-damper modeling of magnetic bearings is obtained:

$$m\ddot{x} - f(x,i) \equiv m\ddot{x} + d\dot{x} + kx = 0 \tag{2.7}$$

2.3 Dynamics of a rigid rotor

Modeling rotor dynamics has been an ongoing task where several models were presented. Namely, the Rankine rotor model (1869) presented as a 2 DoF spring-mass system that can execute a lateral motion and thus represent the whirling orbits. Föppl model (1895) introduced an undamped rotor model as single disk mounted on a circular shaft supported by bearings at each end. Jeffcott (1919) reproduced the Föppl model by adding the damping effects. These last two models, despite the simplifications they underwent, feature real phenomena such as the gyroscopic effect, destabilizing effects from imbalances or impacts, and rotor behaviors at critical speeds. These features along many others such as cross-coupled forces make the vibration analysis of rotating machines distinct and intricate. For instance, destabilizing effects occur mainly due to imbalances in the rotor that cannot be avoided. They are responsible for the manifestation of unpredictable whirling motions that can be detrimental to the machine. Modeling these imbalances is crucial in order to predict the operating behaviors of the rotor and thus anticipate any form of failure.

When a rigid rotor that is spinning with an angular speed Ω is subjected to an impact, it executes a conical or parallel planar motion around its rotation axis. This planar motion of the rotor is called a whirling motion and has a whirling rate or speed ω. The whirling motion are mainly categorized, according to their precession direction, into forward whirls and backward whirls: a whirl that has the same direction as the shaft rotation is called a forward whirl (FW) and a precession in the opposite direction is called a backward whirl (BW). The FW and BW are affected by the tumbling and tilt motion of the rotor along the conservation of angular momentum due to the gyroscopic effects.

The frequencies of the free whirling motions are called natural whirling frequencies or Eigen-frequencies, and the related mode shapes are called natural whirling modes or Eigen-vectors. They are determined in an Eigenvalue problem where the whirling frequencies are obtained from the characteristic frequency equation and the Eigen-vectors are indefinite and require a certain procedure to be determined. Plotting the Eigenfrequencies versus the rotational speed of the rotor delivers the natural frequency diagram or the Campbell-diagram also called a whirl speed map. This helps determine the critical speeds ω_c and thus promote predicting resonance in the system as illustrated in Figure 2.15. The rotor is said to be in resonance when it vibrates at its whirling natural frequencies or critical speeds. This is particularly problematic since any unbalance force can cause the rotor to have a large vibration response that, eventually, might lead to device failure.

When the spinning rotor is subjected to unbalance forces and moments due to an offset of the center of gravity G from the geometrical center, or tilted principle axes of inertia from its axis of rotation, it undergoes a forced whirling motion. The forced whirling is a dynamic unbalance response called the "operating deflection shape" (ODS). In a rotating machine, two types of forced whirling can be observed. The most common type is the synchronous-whirling where the speed of the whirl ω is equal to the shaft speed Ω, and a non-synchronous whirl where the whirl speed and shaft speed are not equal, this type of whirling is destructive since it can cause massive undesired vibrations. Synchronous and non-synchronous whirls can be represented in Figure 2.14, by assuming that the mass imbalance leads the rotor whirl by an angle γ.

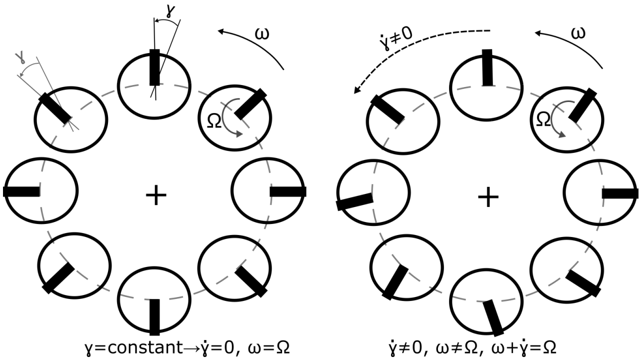

Figure 2.14: Synchronous whirl(left), non-synchronous whirl(right).

As for the unbalance response, there are three types of vibrations that occur in a rotor, torsional vibrations, axial vibrations and lateral vibrations. Torsional vibrations can be regarded as an oscillatory twisting of the shaft[11]. Unlike the axial and lateral vibrations, torsional ones are rarely coupled to the vibrations of the stator and supporting structure and their natural frequencies are independent from the rotational speed[9]. Axial vibrations are not a concern in this study case since the rotor is supported with axial AMB and thus, an active axial control ensures that these vibrations remain in a tolerable range. Subsequently and due to all the unbalances that the rotor experiences, lateral vibrations can become unstable, especially in resonance sites. The natural-frequencies of lateral vibrations are strongly influenced by the rotational speed and the properties of the supporting bearings. This last type of vibrations is the focus point of the unbalance response in this study.

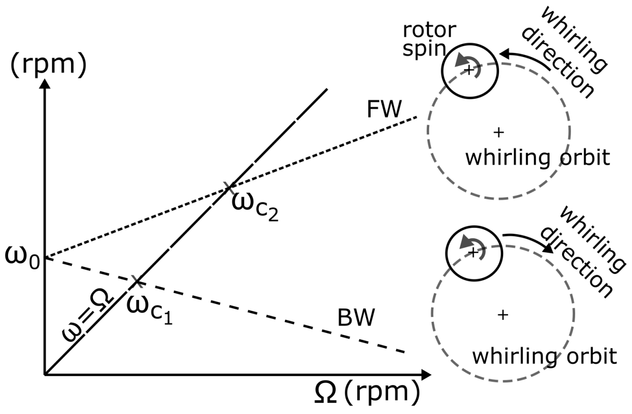

Figure 2.15: Campbell-diagram presenting a single whirl mode.

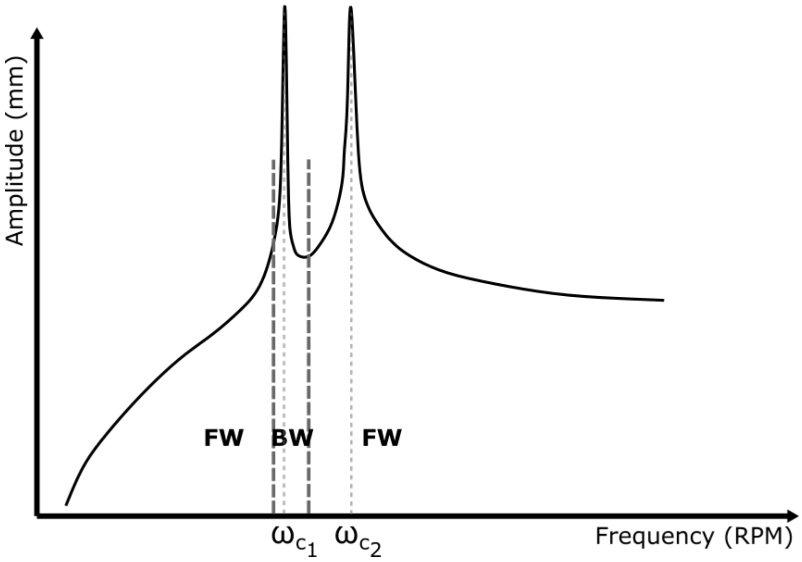

Figure 2.16: Mass unbalance response of an asymmetric Jeffcott rotor (qualitatively reproduced from[17] with modifications).

In order to analytically determine the whirling modes and frequencies, the equations of motion must be examined and solved in a definite coordinate system. The Eigenvalue problem arises through the process of solving for the non-trivial solution. The equations of motion can be derived using either Newton's second law, Lagrange's equations or through Newton-Euler equations. The equations of motions can be developed in two ways by describing the system either in a rotating coordinate system or in a static one.

In a rotating reference of frame, also called a body-fixed frame, the center of gravity has a fixed position and the apparent forces such as the centrifugal, Coriolis and Euler forces that arise due to the system being non-inertial must be taken into account. Using a body-fixed frame is advantageous when dealing with an asymmetric rotor. An asymmetric rotor presents transverse stiffness that differ from a section to another along the rotor's length. When defined directly in an inertial frame, this leads to equations of motion with coefficients that vary sinusoidally, this results in a system that is parametrically excited[9]. However, the body-fixed frame changes orientation and position as it rotates and thus cannot give actual information about the whirling orbits and the displacements of the center or at the bearings. Hence, the need to convert the system back in a definite inertial frame of reference, also denoted as the static coordinate system.

2.3.1 The gyroscopic effects

The gyroscopic effect is a crucial phenomenon in the dynamics of rotating machines. For a uniform axis-symmetric rotor spinning about the z-axis with a constant angular velocity Ω the angular momentum of the rotor about Oz is $I_{zz}\Omega$, where I_{zz} is the moment of inertia about the longitudinal axis. If the disk rotates about Oy with an angular velocity $\dot{\theta}$ over a period of time δt, the angle of rotation θ is $\theta = \dot{\theta}\delta t$. This will lead to a vector change in the direction of the angular momentum $I_{zz}\Omega$ along Ox. The magnitude of the angular momentum is $M_x\delta t$ which gives:

$$\begin{aligned} M_x &= I_{zz}\Omega\frac{\delta\theta}{\delta t} \\ \Rightarrow M_x &= I_{zz}\Omega\frac{d\theta}{dt} = I_{zz}\Omega\dot{\theta}\text{ , as } \delta t \to 0 \end{aligned} \tag{2.8}$$

Similarly, if the rotor rotates about Ox with an angular velocity $\dot{\phi}$ over a small period of time δt, the angle of rotation ϕ is $\phi = \dot{\phi}\delta t$. This results in changing the direction of the angular momentum along the negative direction of Oy[9] as presented in Figure 2.17, which can be expressed as:

$$\begin{aligned} -M_y &= I_{zz}\Omega\frac{\delta\phi}{\delta t} \\ \Rightarrow M_y &= -I_{zz}\Omega\frac{d\phi}{dt} = -I_{zz}\Omega\dot{\phi}\text{ , as } \delta t \to 0 \end{aligned} \tag{2.9}$$

Generally, while the rotor spins around the z-axis, it also rotates simultaneously about x- and y-axes. The instantaneous angular velocities around these axes produce the torques $I_{yy}\ddot{\theta}$ and $I_{xx}\ddot{\phi}$. For an axis-symmetric rotor $I_{xx} = I_{yy} = I_d$ The resultant moments M_x and M_y acting on the rotor becomes:

$$I_d\ddot{\phi} + I_{zz}\Omega\dot{\theta} = M_x \tag{2.10a}$$

$$I_d\ddot{\theta} - I_{zz}\Omega\dot{\phi} = M_y \tag{2.10b}$$

Where $I_{zz}\Omega\dot{\theta}$ and $-I_{zz}\Omega\dot{\phi}$ are the gyroscopic moments.

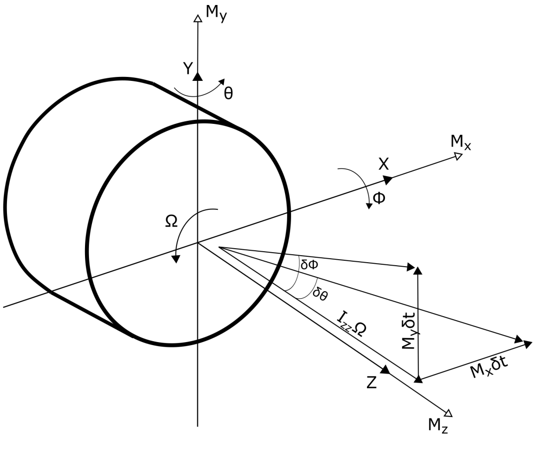

Figure 2.17: The gyroscopic effect.

2.3.2 Rotor unbalances

In rotors, unbalance is inevitable due to many causes such as manufacturing errors, structure deformations and wear. It occurs when the principle axis of inertia deviates from the axis of rotation and manifests in two main forms. One type of error produces a static unbalance, in this case the principle axis of inertia is displaced parallel to the axis of rotation and the center of gravity *G* of the rotor has an eccentricity *e* from the axis of rotation as illustrated in Figure 2.18. The second type of error produces a couple unbalance when the principle axis of inertia is tilted with a tilt angle τ (otherwise called a skew angle or swash) and intersects the axis of rotation at the center of gravity. It can be noticed that the static eccentricity can be represented by a single lumped mass whose eccentricity produces a centrifugal force proportional to the square of the rotational speed. On the other hand, the couple unbalance can be represented by two lumped masses acting as the center of gravity of the right and left halves of the rotor whose centrifugal forces work in opposite directions and thus resulting in a moment force proportional to the square of the rotational speed[10].

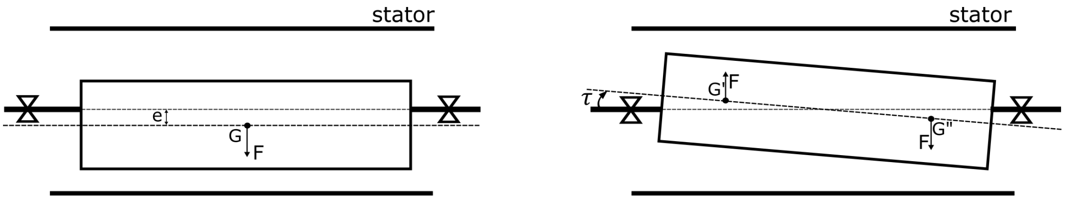

Figure 2.18: Representation of static eccentricity and tilt as lumped parameters.

The general form of unbalance occurring in a rotor is the dynamic unbalance. This type of unbalance is a combination of the static and couple unbalance and other forms of unbalances that might occur during operation. These unbalances are the main source of vibrations that occur in a rotor.

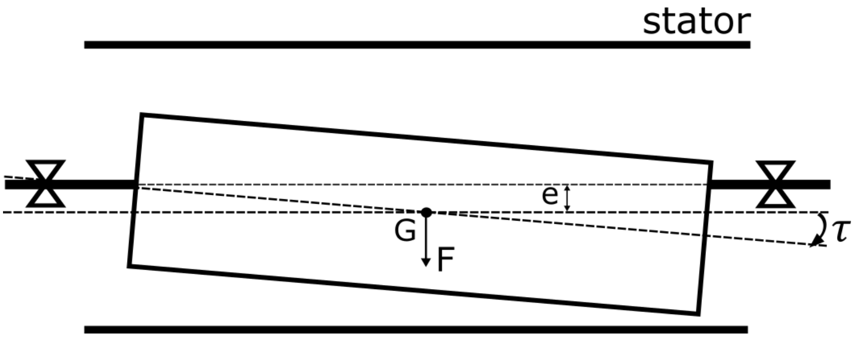

Figure 2.19: Representation of dynamic unbalance.

3 Numerical methods: modeling approach using Bond-Graphs

Several procedures and modeling schemes can be applied and carried out in order to reach a performing rotor model. A particular distinction between the models is whether to consider the motion solely in an inertial-frame or to also include the rotating frame and thus, the need to incorporate a frame transformation.

3.1 The rotor model

Based on the investigated rotor properties, several assumptions can be established:

- The rotor is rigid, the supporting bearings stiffness are very soft compared to the shaft stiffness and the shaft does not bend.
- The lateral bearings supports are isotropic: the horizontal and vertical stiffness coefficients are identical at each of the bearings and are denoted as the radial stiffness.
- The rotor is asymmetric which means that the distances between the rotor center and each of the bearings are not equal, and that the transverse stiffness and damping coefficients vary on each section along the length of the rotor.
- The effective mass m of the rotor represents the total mass.
- It is assumed that the whirling motions are only synchronous. This allows to consider that the whirling speed is equal to the spin speed of the rotor $\omega = \Omega$. ω and Ω can be used interchangeably to denote the spin speed of the rotor without ambiguity. Any other whirling frequency that might be mentioned will be denoted in reference to its mode to avoid confusion.

Another assumption that is rather questionable is whether to consider the rotor to be axis-symmetric, in this case the moments of inertia about the transversal axes are estimated to be equal. These assumptions allow to define and simplify the case in order to numerically model it. The rotor model can be reduced to the mass-spring-damper representation displayed in Figure 3.1.

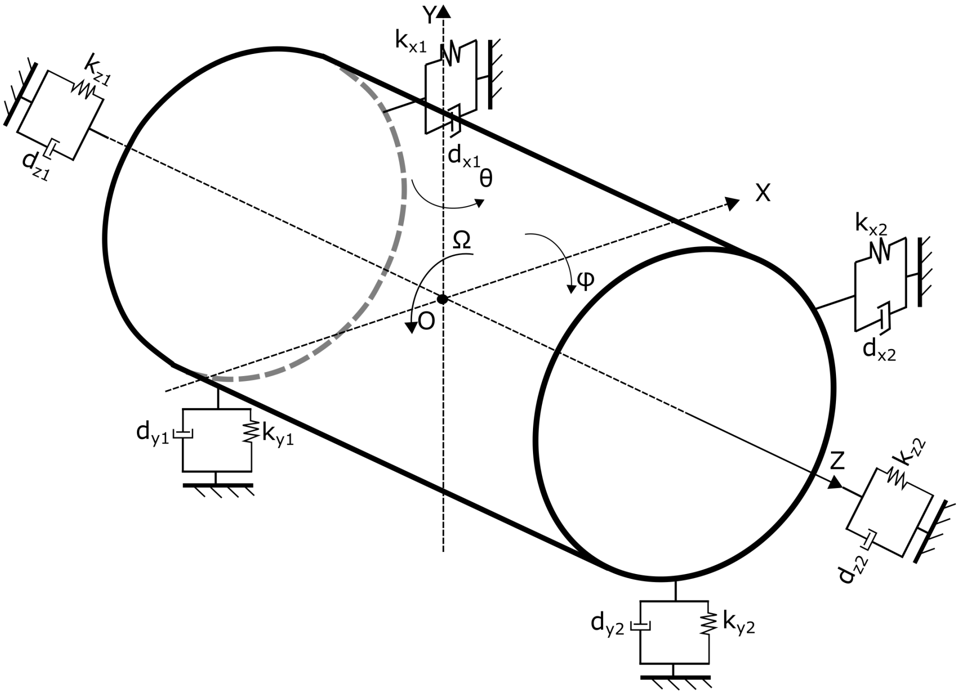

Figure 3.1: 6 DoF mass-spring-damper model of the rigid rotor.

The rotor will be modeled using mostly 3D power bonds. This allows to depict all the degree of freedom of the system in each bond.

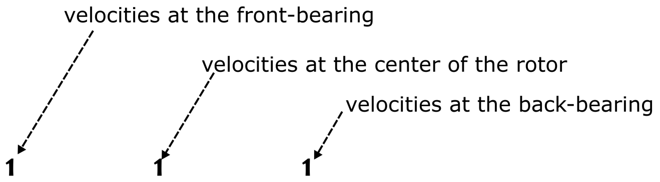

Figure 3.2: Bond-Graph layout of 1-elements representing the velocities at the rotor center and the bearings.

Using a PowerMux "|", the velocities at the bearings, as presented in Figure 3.2, can be split into translational and angular velocities as shown in Figure 3.3.

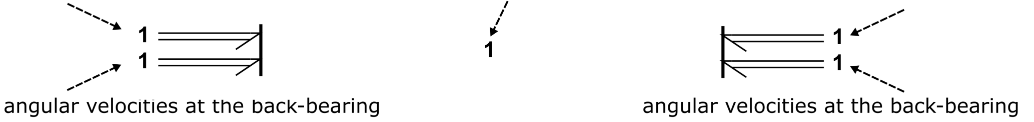

Figure 3.3: Bond-Graph layout of 1-elements representing the velocities at the center and the bearings using a PowerMux.

3.1.1 Modeling the rotor bearings

At first, the motion at the bearings can be modeled. The motion at the center of the rotor is modeled in the next sections. v_s and ω are respectively the linear and angular velocity of rotor center defined as $v_s^T = [\dot{x}\ \dot{y}\ \dot{z}]$ and $\omega^T = [\omega_x\ \omega_y\ \omega_z] \equiv [\dot{\phi}\ \dot{\theta}\ \Omega]$.

Since the rotor is a rigid body, the angular velocities $\omega_1^T = [\omega_{x1}\ \omega_{y1}\ \omega_{z1}]$ and $\omega_2^T = [\omega_{x2}\ \omega_{y2}\ \omega_{z2}]$ at the front and back-bearings are assumed to be equal to the angular velocities at the center of the rotor.
The linear motion of the bearings can be defined in terms of their positions with respect to the center.

Motion of the front-bearing:

$$\begin{aligned} x_1 &= x - L_1\phi \\ y_1 &= y + L_1\theta \\ z_1 &= z \end{aligned} \tag{3.1}$$

Motion of the back-bearing:

$$\begin{aligned} x_2 &= x + L_2\phi \\ y_2 &= y - L_2\theta \\ z_2 &= z \end{aligned} \tag{3.2}$$

The linear velocities at the bearings are thus:

At the front-bearing:

$$\begin{aligned} \dot{x}_1 &= \dot{x} - L_1\dot{\theta} \\ \dot{y}_1 &= \dot{y} + L_1\dot{\phi} \\ \dot{z}_1 &= \dot{z} \end{aligned} \tag{3.3}$$

At the back-bearing:

$$\begin{aligned} \dot{x}_2 &= \dot{y} + L_2\dot{\theta} \\ \dot{y}_2 &= \dot{y} - L_2\dot{\phi} \\ \dot{z}_2 &= \dot{z} \end{aligned} \tag{3.4}$$

This allows to describe the velocities in matrix form:

$$\begin{bmatrix} \dot{x}_1 \\ \dot{y}_1 \\ \dot{z}_1 \\ \omega_{x1} \\ \omega_{y1} \\ \omega_{z1} \end{bmatrix} = \begin{bmatrix} 1 & 0 & 0 & 0 & -L_1 & 0 \\ 0 & 1 & 0 & L_1 & 0 & 0 \\ 0 & 0 & 1 & 0 & 0 & 0 \\ 0 & 0 & 0 & 1 & 0 & 0 \\ 0 & 0 & 0 & 0 & 1 & 0 \\ 0 & 0 & 0 & 0 & 0 & 1 \end{bmatrix} \begin{bmatrix} \dot{x} \\ \dot{y} \\ \dot{z} \\ \omega_x \\ \omega_y \\ \omega_z \end{bmatrix} \tag{3.5}$$

and:

$$\begin{bmatrix} \dot{x}_2 \\ \dot{y}_2 \\ \dot{z}_2 \\ \omega_{x2} \\ \omega_{y2} \\ \omega_{z2} \end{bmatrix} = \begin{bmatrix} 1 & 0 & 0 & 0 & L_2 & 0 \\ 0 & 1 & 0 & -L_2 & 0 & 0 \\ 0 & 0 & 1 & 0 & 0 & 0 \\ 0 & 0 & 0 & 1 & 0 & 0 \\ 0 & 0 & 0 & 0 & 1 & 0 \\ 0 & 0 & 0 & 0 & 0 & 1 \end{bmatrix} \begin{bmatrix} \dot{x} \\ \dot{y} \\ \dot{z} \\ \omega_x \\ \omega_y \\ \omega_z \end{bmatrix} \tag{3.6}$$

The transformation matrices for both bearings are defined respectively as $\underline{\mathrm{m}}_1$ and $\underline{\mathrm{m}}_2$. They can be applied as the modulus of the transformation elements (TF) that link each bearing to the center.

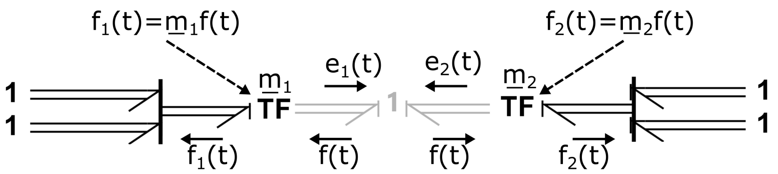

Figure 3.4: Bond Graph layout of the velocities at the bearings.

Additionally, two types of magnetic eccentricities can be observed at the magnetic bearings. An initial lateral offset e_S with reference to the origin of the centerline of the stator that exists due to the UMP in the static magnetic field. A second eccentricity e_R can be observed during operation. This eccentricity appears due to an occurring magnetic restoring force that acts in the direction of reducing the rotor eccentricity or offset[7]. They are qualitatively shown in Figure 3.5, and are defined as:

$$e_S = \begin{bmatrix} e_{S_x} \\ e_{S_y} \\ 0 \end{bmatrix} \quad \text{and} \quad e_R = \begin{bmatrix} |e_R|cos(\Omega t) \\ |e_R|sin(\Omega t) \\ 0 \end{bmatrix} \tag{3.7}$$

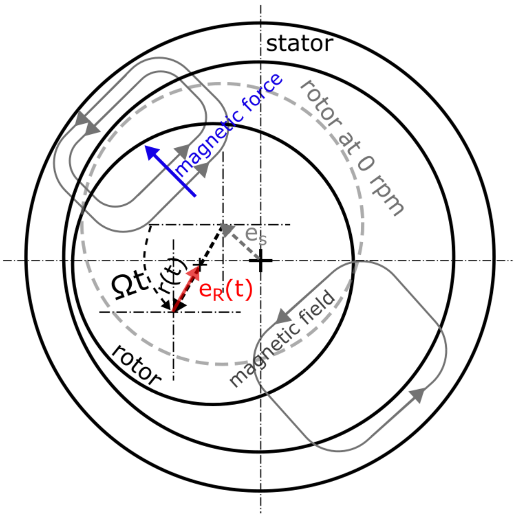

Figure 3.5: Qualitative representation of unsymmetrical flux distribution causing eccentricity e_S (grey) at 0 (rpm), and eccentricity e_R (red) during operation due to magnetic restoring force ($r(t)$ is the instantaneous position of the bearing's center).

These eccentricities can be added directly into the stiffness element (MC) at each of the bearings where the stiffness matrix is defined for the translational DoF as:

$$\underline{\mathbf{K}} = \begin{bmatrix} k_{radial} \\ k_{radial} \\ k_{axial} \end{bmatrix} = \begin{bmatrix} k_x \\ k_y \\ k_z \end{bmatrix} \tag{3.8}$$

This can be represented for both bearings

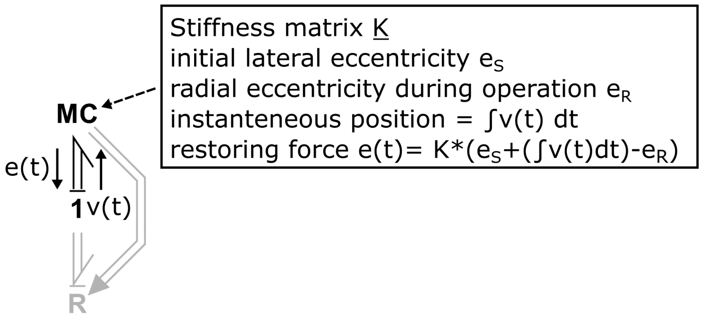

Figure 3.6: Stiffness element at the bearings.

Since no data were given about the damping coefficients, and since these coefficients are harder to measure and to predict in models, directly applying viscous damping coefficients is not practical. It is more reasonable to rather use the stiffness-proportional damping $\underline{\mathbf{D}}$ whose proportionality coefficient μ is set as a random parameter that can be adjusted along the modeling by means of trial and error. The stiffness proportional coefficient damping matrix:

$$\underline{\mathbf{D}} = \mu\underline{\mathbf{K}} \tag{3.9}$$

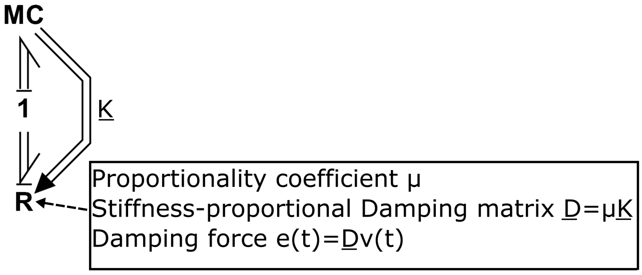

Figure 3.7: R-element at the bearings.

As for the rotational motion at the bearings, the stiffness elements are only attributed the angular stiffness $\underline{\mathbf{K}}_{tilt}^{T} = [k_R\ k_R\ 0]$. The rotational motion of the bearings do not have a proper damping since this damping is assumed to be related to the gyroscopic effect that will be modeled later on.
A two-port 0-junction can be added for more legibility. The bearings can thus be modeled as outlined in Figure 3.8.

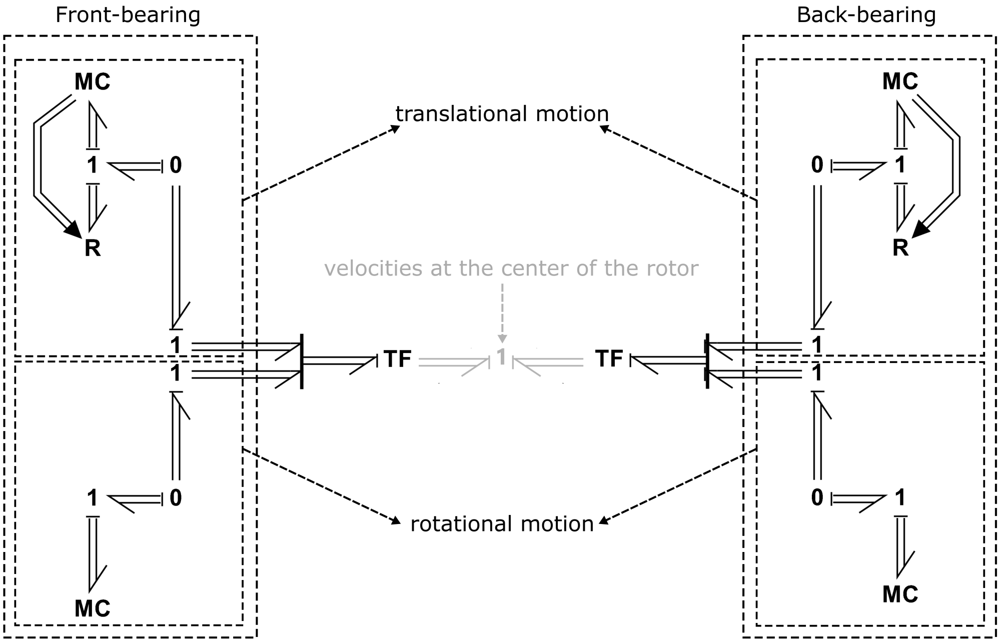

Figure 3.8: Bond Graph modelling of the bearings motion.

3.1.2 Rotor models in the inertial-frame

At first, the rotor and its dynamics are modeled through simple approaches in an inertial reference of frame.

Rotor unbalances

Modeling unbalances in a rotor is one of the most important tasks. The layout of the lateral deflection can be viewed in Figure 3.9. S is the geometrical center that lies on the rotational axis. Generally and during operation, $S(x, y)$ is deflected in the $xy-$plane, this radial deflection of S defines the ODS.

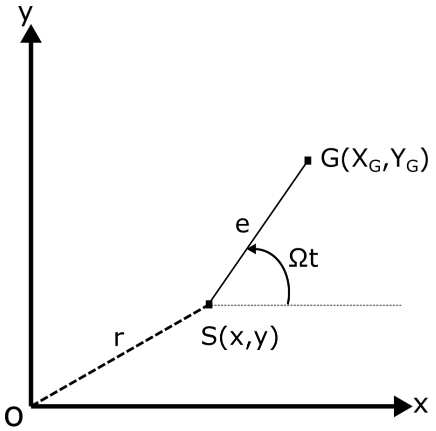

Figure 3.9: Lateral deflection - general layout.

Considering the displacement of the rotor center of gravity $G(X_G, Y_G)$ along the x- and y-axis. The static eccentricity is defined as $e = |SG|$. The rotor has a constant rotational speed Ω. The instantaneous angle between $\vec{SG}$ and the x-axis is defined as Ωt. As for X_G and Y_G their time derivatives can be defined as:

$$\begin{aligned} X_G &= x + ecos(\Omega t) \\ \Rightarrow \dot{X}_G &= x - e\Omega sin(\Omega t) \\ \Rightarrow \ddot{X}_G &= \ddot{x} - e\Omega^2 cos(\Omega t) \\ \text{and } \; Y_G &= y + esin(\Omega t) \\ \Rightarrow \dot{Y}_G &= x + e\Omega cos(\Omega t) \\ \Rightarrow \ddot{Y}_G &= \ddot{y} - e\Omega^2 sin(\Omega t) \end{aligned} \tag{3.10}$$

Moreover, when the couple unbalance is considered, the principle axis of inertia of the rotor is tilted from the axis of rotation with a skew angle τ. Besides, at a constant rotational speed Ω, the rotor axis swings with the angles ϕ and θ around the x- and y-axes. Therefore, the angular positions ϕ_x and θ_y of the rotor are:

$$\begin{aligned} \phi_x &= \phi - \tau cos(\Omega t) \\ \Rightarrow \dot{\phi}_x &= \dot{\phi} + \tau\Omega sin(\Omega t) \\ \Rightarrow \ddot{\phi}_x &= \ddot{\phi} + \tau\Omega^2 cos(\Omega t) \end{aligned} \tag{3.11}$$

And

$$\begin{aligned} \theta_y &= \theta + \tau sin(\Omega t) \\ \Rightarrow \dot{\theta}_y &= \dot{\theta} + \tau \Omega cos(\Omega t) \\ \Rightarrow \ddot{\theta}_y &= \ddot{\theta} - \tau \Omega^2 sin(\Omega t) \end{aligned} \tag{3.12}$$

The equations of motion

The simplest method to derive the equations of motion is by applying Newton's second law. From the free-body diagram presented in Figure 3.10, the resultant forces and moments acting on the rotor due to the bearings are:

$$\begin{aligned} m\ddot{x} &= f_x = -(f_{x1} + f_{x2}) \\ m\ddot{y} &= f_y = -(f_{y1} + f_{y2}) \\ m\ddot{z} &= f_z = f_{z2} - f_{z1} \\ I_d\ddot{\theta}_x + I_{zz}\Omega\dot{\theta}_y &= L_2 f_{y2} - L_1 f_{y1} \\ I_d\ddot{\theta}_y - I_{zz}\Omega\dot{\theta}_x &= L_1 f_{x1} - L_2 f_{x2} \\ I_{zz}\ddot{\omega}_z &= \tau_z \end{aligned} \tag{3.13}$$

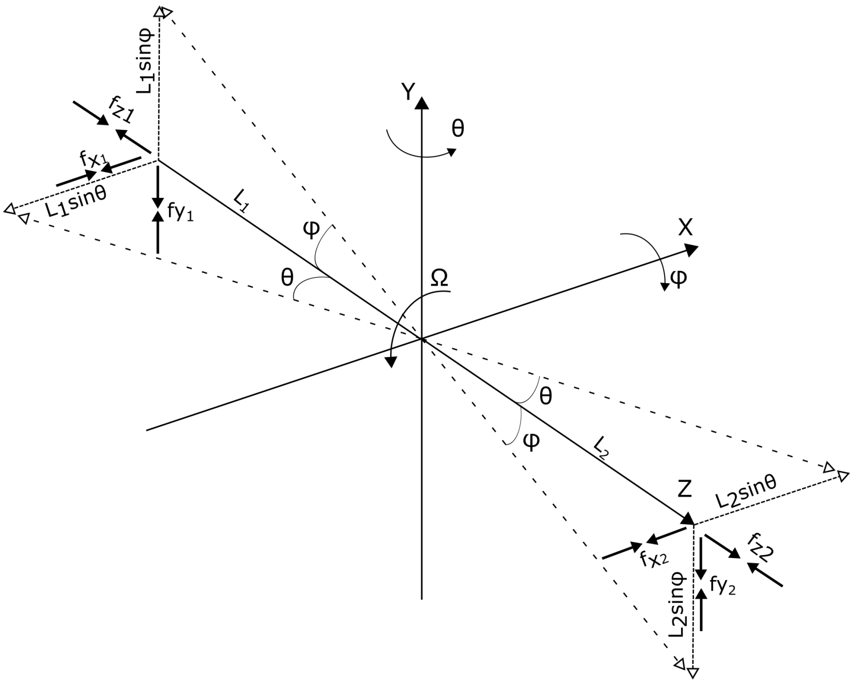

Figure 3.10: Free-body layout of the rigid rotor model on flexible bearings.

For a rigid rotor with isotropic support bearings, the radial stiffness coefficients denoted by k and radial damping coefficients d, as well as, the axial stiffness and damping coefficients, are respectively at the front-bearing k_{x1}, K_{y1}, k_{z1}, d_{x1}, d_{y1}

and d_{z1}, and at the back-bearing k_{x2}, K_{y2}, k_{z2}, d_{x2}, d_{y2} and d_{z2}. This yields:

$$\begin{aligned}
f_{x1} &= k_{x1}(x - L_1\theta) + d_{x_1}(\dot{x} - L_1\dot{\theta})\\
f_{x2} &= k_{x2}(x + L_2\theta) + d_{x_2}(\dot{x} + L_2\dot{\theta})\\
f_{y1} &= k_{y1}(y + L_1\phi) + d_{y_1}(\dot{y} + L_1\dot{\phi})\\
f_{y2} &= k_{y2}(y - L_2\phi) + d_{y_2}(\dot{y} - L_2\dot{\phi})\\
f_{z1} &= k_{z1}z + d_{z1}\dot{z}\\
f_{z2} &= k_{z2}z + d_{z2}\dot{z}
\end{aligned} \tag{3.14}$$

The translational, coupling and tilt damping and stiffness coefficients have consecutively the indices T, C and R.
In x-direction:

$$\begin{aligned}
K_{xT} &= K_{x1} + K_{x2}\\
K_{xC} &= -L_1 \cdot K_{x1} + L_2 \cdot K_{x2}\\
K_{xR} &= L_1^2 \cdot K_{x1} + L_2^2 \cdot K_{x2}\\
d_{xT} &= d_{x1} + d_{x2}\\
d_{xC} &= -L_1 \cdot d_{x1} + L_2 \cdot d_{x2}\\
d_{xR} &= L_1^2 \cdot d_{x1} + L_2^2 \cdot d_{x2}
\end{aligned} \tag{3.15}$$

And in y-direction:

$$\begin{aligned}
K_{yT} &= K_{y1} + K_{y2}\\
K_{yC} &= -L_1 \cdot K_{y1} + L_2 \cdot K_{y2}\\
K_{yR} &= L_1^2 \cdot K_{y1} + L_2^2 \cdot K_{y2}\\
d_{yT} &= d_{y1} + d_{y2}\\
d_{yC} &= -L_1 \cdot d_{y1} + L_2 \cdot d_{y2}\\
d_{yR} &= L_1^2 \cdot d_{y1} + L_2^2 \cdot d_{y2}
\end{aligned} \tag{3.16}$$

For an axis-symmetric rotor with a constant rotational speed Ω and where the axial displacement is negligible in comparison to that in the lateral plane, a simplification can be made to reduce the EOM to 4 DoF that deal with the lateral motion of the rotor. The equations of motion in terms of the displacement of the center of gravity G and the rotor angular position:

$$\begin{aligned}
m\ddot{X}_G = f_x &= -(f_{x1} + f_{x2})\\
m\ddot{Y}_G = f_y &= -(f_{y1} + f_{y2})\\
I_d\ddot{\phi}_x + I_{zz}\Omega\dot{\theta}_y &= L_2 f_{y2} - L_1 f_{y1}\\
I_d\ddot{\theta}_y - I_{zz}\Omega\dot{\phi}_x &= L_1 f_{x1} - L_2 f_{x2}
\end{aligned} \tag{3.17}$$

Utilizing Equations 3.14 to substitute the resultant forces due to the bearings, one obtains:

$$\begin{aligned}
m\ddot{X}_G + d_{xT}\dot{x} + d_{xC}\dot{\theta} + k_{xT}x + K_{xC}\theta &= 0\\
m\ddot{Y}_G + d_{yT}\dot{y} - d_{yC}\dot{\phi} + K_{yT}y - K_{yC}\phi &= 0\\
I_d\ddot{\phi}_x + I_{zz}\Omega\dot{\theta}_y - d_{yC}\dot{y} + d_{yR}\dot{\phi} - k_{yC}y + k_{yR}\phi &= 0\\
I_d\ddot{\theta}_y - I_{zz}\Omega\dot{\phi}_x + d_{xC}\dot{x} + d_{xR}\dot{\theta} + k_{xC}x + k_{xR}\theta &= 0
\end{aligned} \tag{3.18}$$

By substituting equations 3.10-3.12 into 3.18:

$$m\ddot{x} + d_{xT}\dot{x} + d_{xC}\dot{\theta} + k_{xT}x + K_{xC}\theta = me\Omega^2 cos(\Omega t) \tag{3.19a}$$

$$m\ddot{y} + d_{yT}\dot{y} - d_{yC}\dot{\phi} + K_{yT}y - K_{yC}\phi = me\Omega^2 sin(\Omega t) \tag{3.19b}$$

$$I_d\ddot{\phi} + I_{zz}\Omega\dot{\theta} - d_{yC}\dot{y} + d_{yR}\dot{\phi} - k_{yC}y + k_{yR}\phi = (Izz - I_d)\tau\Omega^2 cos(\Omega t) \tag{3.19c}$$

$$I_d\ddot{\theta} - I_{zz}\Omega\dot{\phi} + d_{xC}\dot{x} + d_{xR}\dot{\theta} + k_{xC}x + k_{xR}\theta = (I_d - Izz)\tau\Omega^2 sin(\Omega t) \tag{3.19d}$$

These are the equations of motion due to the out-of-balance forces and moments.

Implementing the equations of motion into Bond-graph modeling

Next comes applying the rational of Bond-graph and the EOM into the modeling. First, the inertia-elements (I) of the rotor can be established. The constitutive equation of the I-elements can be used to determine the velocity in each direction as explained in Figure 3.11.

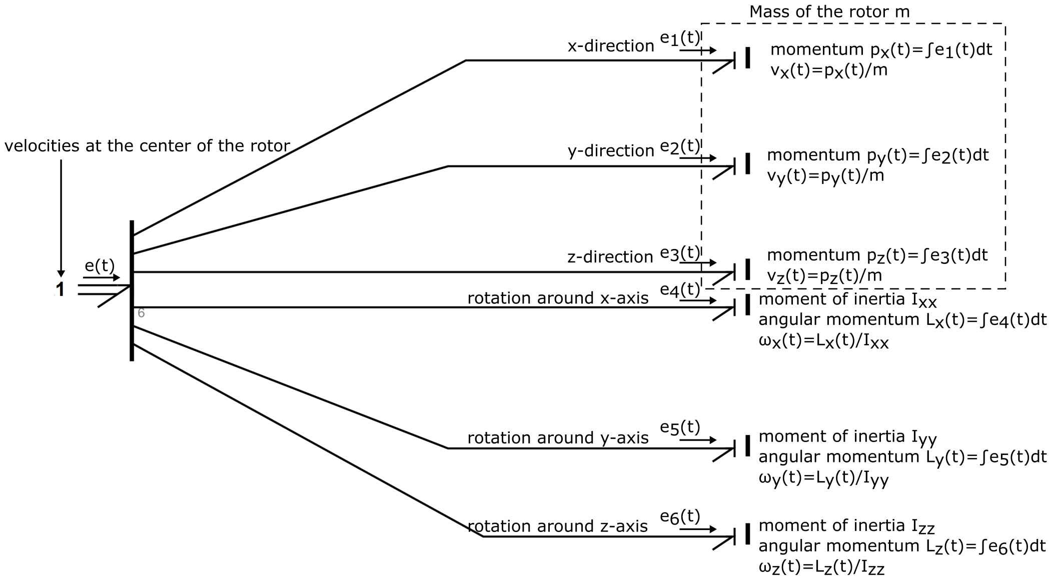

Figure 3.11: Inertia elements of the rotor.

In a second step, the gyroscopic effects are added. The term $I_{zz}\Omega$ is a cross-coupled damping coefficient since it appears in the damping terms or matrix, however it acts like stiffness[11]. Since this effect does not dissipate energy, it does not need to be modeled using an R-element. A modulated gyrator (MGY) is a better choice. There are two ways to add the gyroscopic effect in Bond graph. The first one, is evidently by coupling equations 3.19c and 3.19d.

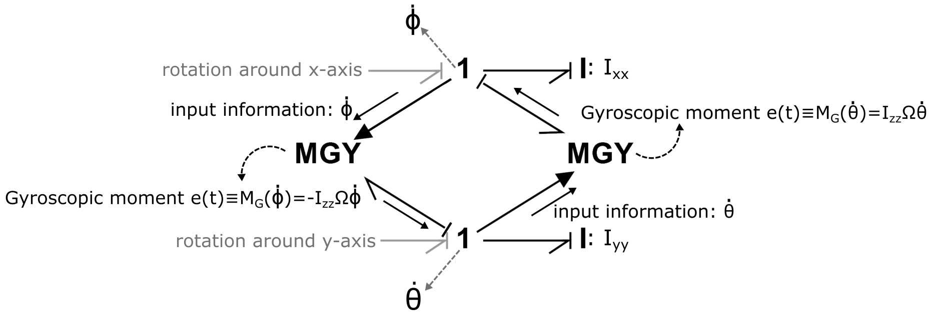

Figure 3.12: Modeling the gyrator effect.

The second method is as stated in Karnopp *et al.*[2] using the gyrator ring constructions where the modular gyrator elements (MGY) represent the cross-coupled product terms with time-varying moduli.

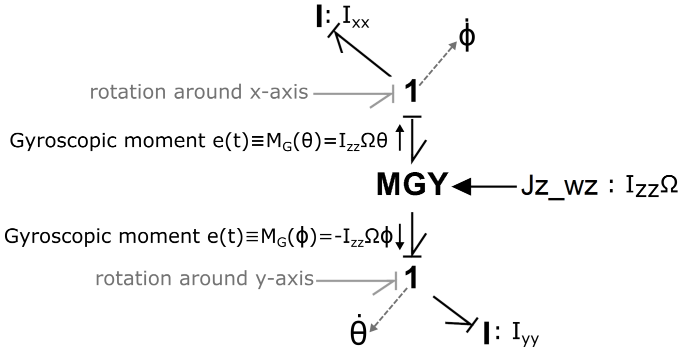

Figure 3.13: Modeling the gyrator effect using a gyrator-ring structure.

Later on , the equations of motion 3.19 can be formulated as the sum of all forces acting on the rotor to be zero. Let this be shown for the translation and rotation about the x-axis:

$$\underbrace{m\ddot{x}}_{e_1(t)} + \underbrace{d_{xT}\dot{x} + d_{xC}\dot{\theta} + k_{xT}x + K_{xC}\theta}_{e_1'(t)} + \underbrace{(-me\Omega^2 cos(\Omega t))}_{e_1''(t)} = 0$$

$$\underbrace{I_d\ddot{\phi}}_{e_4(t)} + \underbrace{I_{zz}\Omega\dot{\theta}}_{e_4'(t)} - \underbrace{d_{yC}\dot{y} + d_{yR}\dot{\phi} - k_{yC}y + k_{yR}\phi}_{e_4''(t)} + \underbrace{(-(Izz - I_d)\tau\Omega^2 cos(\Omega t))}_{e_4'''(t)} = 0$$

Through this formulation, 1-junctions can be set to describe each line of the equations of motion. For instance, for the translation and rotation about the x-axis.

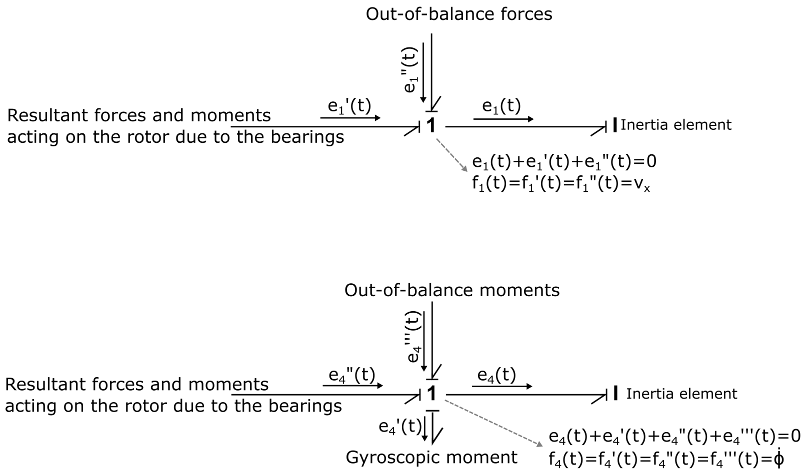

Figure 3.14: Explicit application of the EOM into Bond-graph model.

These 1-junctions can be further applied to the translation in- and the rotation about the y-direction by modeling the out-of-balance forces and moments in modular source of efforts (**MSe**), the final Bond Graph layout of the rotor center can be confined in a sub-model for more clarity, and connected to the 1-junction representing the velocity at the rotor center through (port 1).

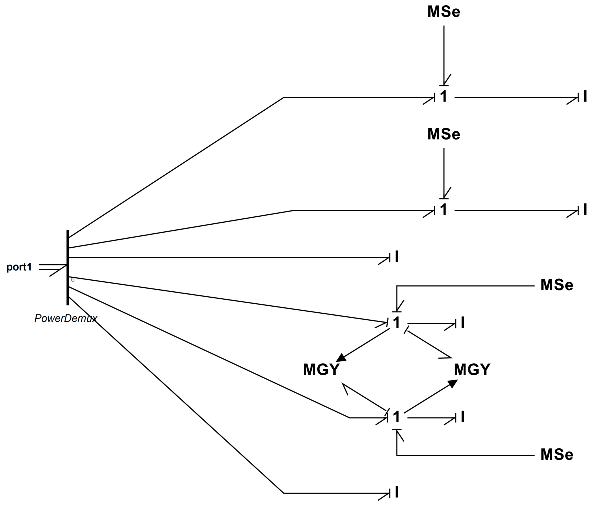

Figure 3.15: Bond-Graph of model (A): submodel of the rotor center displaying the unbalance forces and moments (see Figures A.1 and A.2).

Mukherjee *et al.*[8] provides a model of a spinning shaft depicting the mass eccentricity and its angular orientation by using a 0-junction. For that, the velocities of the mass eccentricity are directly considered in the lateral plane. The position of the center of gravity is determined with reference to the geometrical center S . Equations 3.10 can be re-written as:

$$\begin{aligned} & X_G = ecos(\Omega t) \\ & \Rightarrow \dot{X}_G = -e\Omega sin(\Omega t) \\ \text{and } & Y_G = esin(\Omega t) \\ & \Rightarrow \dot{Y}_G = e\Omega cos(\Omega t) \end{aligned} \tag{3.20}$$

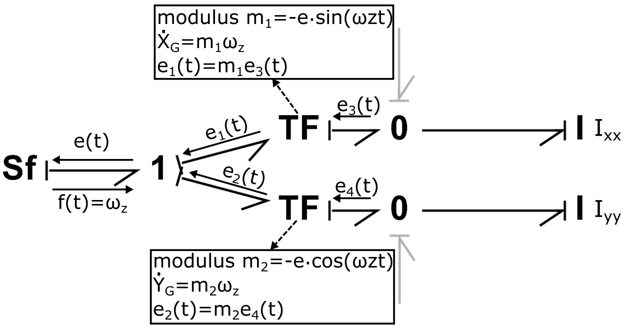

Figure 3.16: Adding the mass imbalance through the scalar 0-element in Bond-graph.

Due to the gyroscopic couples, applying the same approach for the angular displacement can be tricky. In this case, the same procedure applied earlier can be employed here once again.

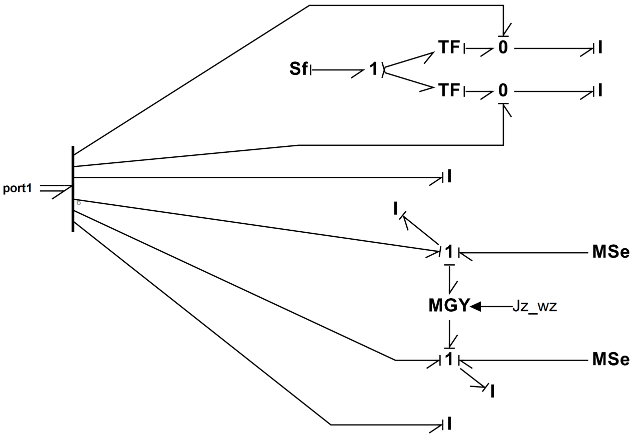

Figure 3.17: Bond-Graph of model (B): submodel of the rotor center displaying the unbalance forces and moments (see Figures A.1 and A.3).

Another point that should be considered is the existence of tilt. Accordingly, the inertia of the rotor center needs to be altered. For simplicity, the tilt can be assumed to initially exist in the yz-plane. The unbalanced inertia tensor can thus be represented as a rotated state of the ideal inertia tensor.

$$\begin{aligned}\underline{I} &= R_x\, \underline{I}_0\, R_x^T \\ &= \begin{bmatrix} 1 & 0 & 0 \\ 0 & cos(\tau) & -sin(\tau) \\ 0 & sin(\tau) & cos(\tau) \end{bmatrix} \begin{bmatrix} I_{xx} & 0 & 0 \\ 0 & I_{yy} & 0 \\ 0 & 0 & I_{zz} \end{bmatrix} \begin{bmatrix} 1 & 0 & 0 \\ 0 & cos(\tau) & sin(\tau) \\ 0 & -sin(\tau) & cos(\tau) \end{bmatrix} \\ &= \begin{bmatrix} I_{xx} & 0 & 0 \\ 0 & I_{yy}cos^2(\tau) & \frac{1}{2}(I_{yy}-I_{zz})sin(2\tau) \\ 0 & \frac{1}{2}(I_{yy}-I_{zz})sin(2\tau) & I_{zz}cos^2(\tau) \end{bmatrix}\end{aligned} \tag{3.21}$$

Where R_x is the elementary rotation matrix around the x-axis. The tilted y- and z-axes of the rotor acquire respectively the moments of inertia $I_{yy}cos^2(\tau)$ and $I_{zz}cos^2(\tau)$.

A model variation (C) is obtained by further tuning the model to acquire a Newton-Euler equations form, where the mass of the rotor and its moments of inertia are split into two separate inertia-elements. For simplification and since the rotor investigated is a rigid one, the rotational displacement of the bearings can be omitted and the tilt stiffness is added at the rotor center. In the inertial-frame, the Newton's second law of motion is applied at the geometrical center of the rotor:

$$\begin{aligned} F_x &= m\ddot{x} \\ F_y &= m\ddot{y} \\ F_z &= m\ddot{z} \end{aligned} \tag{3.22}$$

Which provides a trimmed mass matrix as:

$$\begin{bmatrix} m & 0 & 0 \\ 0 & m & 0 \\ 0 & 0 & m \end{bmatrix} \tag{3.23}$$

The unbalanced inertia tensor $\underline{I}$ is applied as obtained in equation 3.21.

$$\underline{I} = \begin{bmatrix} I_{xx} & 0 & 0 \\ 0 & I_{yy}cos^2(\tau) & \frac{1}{2}(I_{yy}-I_{zz})sin(2\tau) \\ 0 & \frac{1}{2}(I_{yy}-I_{zz})sin(2\tau) & I_{zz}cos^2(\tau) \end{bmatrix}$$

The inertia-elements can be replaced by the IC-field in order to add the centrifugal forces through the unbalance forces, the gyroscopic effects and the unbalance moments, as well as to avoid increasing the number of bonds which proved to cause conflicts at the 1-elements. The gyroscopic and unbalance moments add up as follows:

$$\begin{bmatrix} (I_{zz}-I_d)\tau\Omega^2 cos(\Omega t) \\ (I_d-I_{zz})\tau\Omega^2 sin(\Omega t) \\ 0 \end{bmatrix} - \begin{bmatrix} I_{zz}\omega_z\dot{\theta} \\ -I_{zz}\omega_z\dot{\phi} \\ 0 \end{bmatrix} \tag{3.24}$$

The transformer-elements (TF) relating the bearings to the rotor center in this case have the modulus $m_1 = -[r_{B1}]$ and $m_2 = -[r_{B2}]$ where $[r_{B1}]$ and $[r_{B2}]$ are the skew-symmetric matrix of respectively the front- and back-bearings position relative to the rotor center in the inertial-frame. At the 0-elements, the relations provided in equations 3.3 and 3.4 hold. The modeling is visible and explained in Figure 3.18.

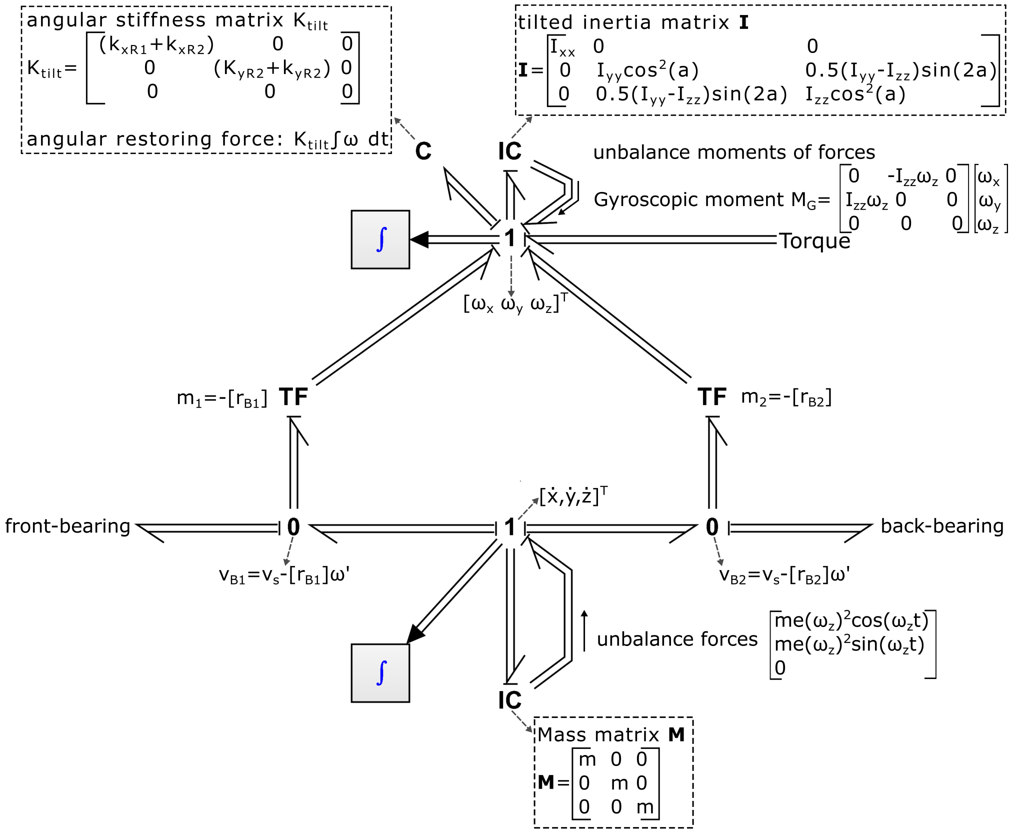

Figure 3.18: Bond-Graph layout of the model (C) (see Figure A.4).

3.1.3 Rotor modeling by including the rotating frame of reference

It can be noticed that using Newton's second law to generate the equations of motion is practical for simple rotors. However, using the energy method this time is advantageous in order to not only establish the equations of motion in the general form but also to generate a form that is favorable for application in Bond-Graphs.
While the general Lagrange's equations allows to describe the rotor without an explicit determination of the forces acting on it, it should be further extended to take into consideration that the rotor undergoes finite rotations. Therefore, transforming the general Lagrange's equations into the quasi-Lagrange's equations is more optimal in order to include the fictitious forces that occur in the rotating reference of frame.

First, a mathematical manipulation using a skew of a vector is shortly presented. with $[a]$ is the skew of a vector $a^T = [a_x\ a_y\ a_z]$:

$$[a] = \begin{bmatrix} 0 & -a_z & a_y \\ a_z & 0 & -a_x \\ -a_y & a_x & 0 \end{bmatrix}$$

The following properties apply: $[a]^T = -[a]$ and $a \times b = [a]b = [b]^T a = -[b]a$, where $b^T = [b_x\ b_y\ b_z]$. A skew of a matrix allows to manipulate the matrix to avoid size conflicts in multiplications.

A detailed transformation into the quasi-Lagrange's equations is presented in references[14] and [13], and in a more simplified form in[15]. For convenience, the transformation is briefly here presented based on the mentioned references. The general Lagrange's equations have the standard form:

$$\frac{d}{dt}(\frac{\partial L}{\partial \dot{q}}) - \frac{\partial L}{\partial q} + \frac{\partial V}{\partial q} = Q \tag{3.25}$$

Where q is the general coordinates, Q represents the generalized forces and the scalar Lagrangian function is $L = T - V$, T is the kinetic energy and V is the potential energy. By separating into the rotational and translational parts, the base-body rotation is:

$$\frac{d}{dt}\frac{\partial L}{\partial \dot{\beta}} - \frac{\partial L}{\partial \beta} = Q_\beta \tag{3.26}$$

And the base-body translation, with r being the inertial position vector:

$$\frac{d}{dt}\frac{\partial L}{\partial v} - \frac{\partial L}{\partial r} = Q_r \tag{3.27}$$

Where Q_β and Q_r are the generalized forces in respectively the body-base rotation and translation. With $\underline{\mathbf{R}}$ being the rotation matrix that will be presented in details in a coming step, the conversion into the quasi-coordinates is performed through the following transformation:

$$\underline{\mathbf{T}} = \frac{1}{2}\left(\begin{bmatrix} \underline{\mathbf{R}} & 0 \\ 0 & \underline{\mathbf{C}}_t \end{bmatrix} \begin{bmatrix} \beta \\ v \end{bmatrix} \right)^T \begin{bmatrix} \underline{\mathbf{I}} & [r] \\ r & m\underline{\mathbf{E}} \end{bmatrix} \begin{bmatrix} \underline{\mathbf{R}} & 0 \\ 0 & \underline{\mathbf{C}}_t \end{bmatrix} \begin{bmatrix} \beta \\ v \end{bmatrix} \tag{3.28}$$

A quasi-coordinate change of variables is thus:

$$\underline{\mathbf{T}} = \frac{1}{2} \begin{bmatrix} \omega' \\ v' \end{bmatrix}^T \begin{bmatrix} \underline{\mathbf{I}} & [r] \\ r & m\underline{\mathbf{E}} \end{bmatrix} \begin{bmatrix} \omega' \\ v' \end{bmatrix} \tag{3.29}$$

The transformation matrix[1] $\underline{\mathbf{C}}_t$ is the direction cosine matrix that relates the body-fixed components of the linear velocity vector $v'^T = [\dot{x}'\ \dot{y}'\ \dot{z}']$ to the inertial ones $v^T = [\dot{x}\ \dot{y}\ \dot{z}]$. $\vec{i}, \vec{j}, \vec{k}$ and $\vec{I}, \vec{J}, \vec{K}$ are the unity vectors in respectively the body-fixed frame and inertial-frame. The scalar products are thus $\vec{I} \cdot \vec{i} = |1| \cdot |1| cos(\vec{I} \cdot \vec{i}) = cos(\vec{I} \cdot \vec{i})$ and so on for the rest of the terms.

$$\begin{aligned} \begin{bmatrix} \dot{x}' \\ \dot{y}' \\ \dot{z}' \end{bmatrix} &= \begin{bmatrix} \vec{I} \cdot \vec{i} & \vec{I} \cdot \vec{j} & \vec{I} \cdot \vec{k} \\ \vec{J} \cdot \vec{i} & \vec{J} \cdot \vec{j} & \vec{J} \cdot \vec{k} \\ \vec{K} \cdot \vec{i} & \vec{K} \cdot \vec{j} & \vec{K} \cdot \vec{k} \end{bmatrix} \begin{bmatrix} \dot{x} \\ \dot{y} \\ \dot{z} \end{bmatrix} \\ &= \begin{bmatrix} cos(\vec{I} \cdot \vec{i}) & cos(\vec{I} \cdot \vec{j}) & cos(\vec{I} \cdot \vec{k}) \\ cos(\vec{J} \cdot \vec{i}) & cos(\vec{J} \cdot \vec{j}) & cos(\vec{J} \cdot \vec{k}) \\ cos(\vec{K} \cdot \vec{i}) & cos(\vec{K} \cdot \vec{j}) & cos(\vec{K} \cdot \vec{k}) \end{bmatrix} \begin{bmatrix} \dot{x} \\ \dot{y} \\ \dot{z} \end{bmatrix} \\ v' &= \qquad\qquad \underline{\mathbf{C}}_t \qquad\qquad v \end{aligned} \tag{3.30}$$

This transformation does not need to be explicitly determined since the velocities in the body-fixed frame are determined directly from the constitutive equations of the I-element.

The rotational quasi-Lagrange equation of motion is obtained by transforming Equation 3.26 by considering that $\underline{\mathbf{T}}$ in Equation 3.28 to be only a function of the angular velocity:

$$\frac{d}{dt}\frac{\partial T}{\partial \omega'} + [\omega']\frac{\partial T}{\partial \omega'} + [v']\frac{\partial T}{\partial v'} = \underline{\mathbf{R}}^{-1} Q_\beta \tag{3.31}$$

The translational quasi-Lagrange equation of motion is obtained by transforming Equation 3.27 by considering $\underline{\mathbf{T}}$ in Equation 3.28 to be only a function of the linear velocity:

$$\frac{d}{dt}\frac{\partial T}{\partial v'} + [\omega']\frac{\partial T}{\partial \omega'} - \frac{\partial T}{\partial r} = \underline{\mathbf{C}}_t^{-1} Q_r \tag{3.32}$$

Using the properties of skew matrices allows to rewrite Equations 3.31 and 3.32 in their final quasi-Lagrange form as:

$$\begin{aligned} \frac{d}{dt}\frac{\partial T}{\partial \omega'} + \omega' \times \frac{\partial T}{\partial \omega'} + v' \times \frac{\partial T}{\partial v'} &= \underline{\mathbf{R}}^{-1} Q_\beta \\ \frac{d}{dt}\frac{\partial T}{\partial v'} + \omega' \times \frac{\partial T}{\partial \omega'} - \frac{\partial T}{\partial r} &= \underline{\mathbf{C}}_t^{-1} Q_r \end{aligned} \tag{3.33}$$

---

[1] The direction cosine matrix is used only to derive the quasi-Lagrange equations, it must not be confused with the use of the rotation matrix to convert both the linear and angular velocities between the inertial-frame and the body-fixed frame as stated in Karnopp *et al.*[2]

the static imbalance is presented here in a general form, for a rigid body whose center of gravity G is displaced from its geometrical center S and rotating around its center with a velocity ω. The velocity v_G of the center of gravity is:

$$v_G = v_s + \omega \times r_G \tag{3.34}$$

Where v_s is the velocity of the body center.

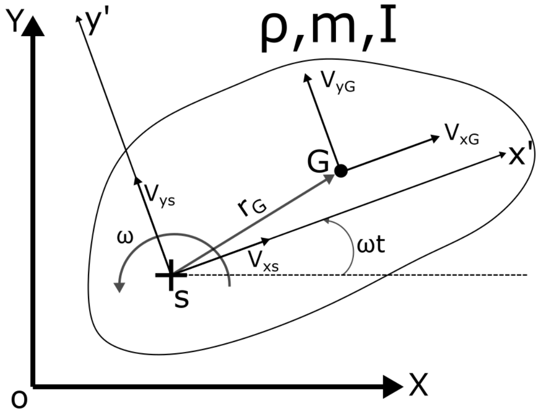

Figure 3.19: General plane motion of a rigid body.

Determining the momenta due to the shifted center of gravity is practical and necessary for their application in Bond Graph. The linear momentum p is thus:

$$\begin{aligned} p &= \int_V \rho(v_s + \omega \times r_G)dV \\ &= m(v_s + \omega \times r_G) \\ &= m v_G \end{aligned} \tag{3.35}$$

Where ρ is the density of the body. The angular momentum L:

$$\begin{aligned} L &= \int_V \rho r_G \times v_G dV \\ &= \int_V \rho r_G \times (v_s + \omega \times r_G)dV \\ &= \underline{I}\omega + r_G \times m v_G \end{aligned} \tag{3.36}$$

Where the first right-hand term is the spin or the rotation about the spin axis, and the second right-hand term is the angular momentum about G.

Using equation 3.34, the kinetic energy can be written as:

$$\begin{aligned} T &= \frac{1}{2}\int_V \rho(v_s+\omega\times r_G)^T(v_s+\omega\times r_G)dV \\ &= \frac{1}{2}mv_s\cdot v_s + v_s(\omega\times mr_G)+\frac{1}{2}\omega^T\underline{\mathbf{I}}\omega \\ &= \frac{1}{2}mv_s^2 + v_s(\omega\times mr_G)+\frac{1}{2}\omega^T\underline{\mathbf{I}}\omega \end{aligned} \tag{3.37}$$

Let the linear velocity be denoted as $v \equiv v_s$ and $r = r_G$. By considering the characteristics of a skew matrix mentioned earlier:

$$\begin{aligned} T &= \frac{1}{2}mv^2 + v(\omega\times mr)+\frac{1}{2}\omega^T\underline{I}\omega \\ &= \frac{1}{2}mv^2 + v(-[r]m\omega)+\frac{1}{2}\omega^T\underline{I}\omega \\ &= \frac{1}{2}mv^2 + v([\omega]mr)+\frac{1}{2}\omega^T\underline{I}\omega \end{aligned} \tag{3.38}$$

And

$$\frac{\partial T}{\partial v} = mv+[\omega]mr = mv+\omega\times mr = mv-m[r]\omega \tag{3.39a}$$

$$\frac{\partial T}{\partial \omega} = v(-m[r])+\underline{I}\omega = -m(v\times r)+\underline{I}\omega = m[r]v+\underline{I}\omega \tag{3.39b}$$

$$\frac{\partial T}{\partial r} = v[\omega]m \tag{3.39c}$$

Substituting and arranging equations 3.39 in the quasi-coordinates Lagrange's equations 3.33, this gives:

$$\begin{aligned} &\frac{d}{dt}\frac{\partial T}{\partial v}+\omega\times\frac{\partial T}{\partial v}-\frac{\partial T}{\partial r} \\ &\quad= \frac{d}{dt}(mv-m[r]\omega)+\omega\times(mv-m[r]\omega)+-v[\omega]m \\ &\quad= m\dot{v}-m[r]\dot{\omega}+\omega\times(mv)+\omega\times(-m[r]\omega)-v[\omega]m \\ &\quad= m\dot{v}-m[r]\dot{\omega}-m[v]\omega+\omega\times(m\omega\times r)-v[\omega]m \\ &\quad= m\dot{v}-m[r]\dot{\omega}-m[v]\omega+\omega\times m[\omega]r-v[\omega]m \\ &\quad= m\dot{v}-m[r]\dot{\omega}-m[v]\omega-m[[\omega]r]\omega-v[\omega]m \\ &\quad= m(\dot{v}-[r]\dot{\omega}-[v]\omega-[[\omega]r]\omega-v[\omega]) \end{aligned} \tag{3.40}$$

And:

$$\begin{aligned} &\frac{d}{dt}\frac{\partial T}{\partial \omega}+\omega\times\frac{\partial T}{\partial \omega}+v\times\frac{\partial T}{\partial v} \\ &\quad= \frac{d}{dt}(m[r]v+\underline{I}\omega)+\omega\times(m[r]v+\underline{I}\omega)+v\times(mv-m[r]\omega) \\ &\quad= m[r]\dot{v}+\underline{I}\dot{\omega}+\omega\times m[r]v+\omega\times\underline{I}\omega+v\times mv+v\times(-m[r]\omega) \\ &\quad= m[r]\dot{v}+\underline{I}\dot{\omega}+\omega\times mr\times v-[\underline{I}\omega]\omega-m[v]v+v\times(-mr\times\omega) \\ &\quad= m[r]\dot{v}+\underline{I}\dot{\omega}+\omega\times(-m[v]r)-[\underline{I}\omega]\omega-m[v]v+v\times m([\omega]r) \\ &\quad= m[r]\dot{v}+\underline{I}\dot{\omega}+m[[v]r]\omega-[\underline{I}\omega]\omega-m[v]v-m[[\omega]r]v \end{aligned} \tag{3.41}$$

Assembling the equations into matrix form:

$$\begin{bmatrix} m\underline{\mathbf{E}} & -m[r] \\ m[r] & \underline{\mathrm{I}} \end{bmatrix} \begin{bmatrix} \dot{v} \\ \dot{\omega} \end{bmatrix} + \begin{bmatrix} -m[\omega] & -m[v]-m[[\omega]r] \\ -m[[\omega]r]-m[v] & m[[v]r]-[\underline{\mathrm{I}}\omega] \end{bmatrix} \begin{bmatrix} v \\ \omega \end{bmatrix} = \begin{bmatrix} f_1 \\ f_2 \end{bmatrix} \tag{3.42}$$

$$\underline{\mathbf{M}}\,\dot{v} + \underline{\mathbf{C}}\,v = \underline{\mathrm{f}} \tag{3.43}$$

Is the general matrix form of the equations of motion, with $\underline{\mathrm{f}}^T = [f_1\ f_2]$ being the corresponding generalized forces. This form of the equations of motion can be directly applied in an IC-element in Bond Graph. Karnopp[2] emphasizes that using the IC-field is more practical in order to avoid several ramifications and algebraic loops in the Bond graph model and thus better depicts the conservation of energy in the system. To achieve that, the Lagrange's equations, which are essentially obtained by applying the calculus of variations for Hamilton's principle[16], need to be further written in the momentum form. The linear and angular momenta can be defined as $p = \partial T/\partial v$ and $L = \partial T/\partial \omega$, when applied in the quasi-Lagrange's equations 3.33, the constitutive law for the IC-element that couples the velocities and generalized momenta can be stated:

$$\begin{aligned} &p = \underline{\mathbf{M}}\,v + a,\ a = 0 \text{ for a constant velocity source} \\ &v = \underline{\mathbf{M}}^{-1} p \text{ (and } \omega = \underline{\mathbf{M}}^{-1} L) \end{aligned} \tag{3.44}$$

The inertia of the rotor using an IC-element can now be established. The mass matrix $\underline{\mathbf{M}}$ and the coefficients matrix of apparent forces $\underline{\mathbf{C}}$ as in equation 3.43 are stated here more comprehensively:

$$\underline{\mathbf{M}} = \begin{bmatrix} m & 0 & 0 & 0 & mr_z & -mr_y \\ 0 & m & 0 & -mr_z & 0 & mr_x \\ 0 & 0 & m & mr_y & -mr_x & 0 \\ 0 & -mr_z & mr_y & I_{xx} & I_{xy} & I_{xz} \\ mr_z & 0 & -mr_x & I_{yx} & I_{yy} & I_{yz} \\ -mr_y & mr_x & 0 & I_{zx} & I_{zy} & I_{zz} \end{bmatrix} \tag{3.45}$$

And:

$$\underline{\mathbf{C}} = \begin{bmatrix} 0 & m\omega'_z & -m\omega'_y & 0 & C & -B \\ -m\omega'_z & 0 & m\omega'_x & -C & 0 & A \\ m\omega'_y & -m\omega'_x & 0 & B & -A & 0 \\ 0 & C & -B & 0 & -F & E \\ -C & 0 & -A & F & 0 & -D \\ B & -A & 0 & -E & D & 0 \end{bmatrix} \tag{3.46}$$

$$\begin{aligned} \textbf{with } A &= m\dot{x}' + m(\omega'_y r_z - \omega'_z r_y) \\ B &= m\dot{y}' + m(\omega'_z r_x - \omega'_x r_z) \\ C &= m\dot{z}' + m(\omega'_x r_y - \omega'_y r_x) \\ D &= m(\dot{y}' r_z - \dot{z}' r_y) - (I_{xx}\omega'_x + I_{xy}\omega'_y + I_{xz}\omega'_z) \\ E &= m(\dot{z}' r_x - \dot{x}' r_z) - (I_{yx}\omega'_x + I_{yy}\omega'_y + I_{yz}\omega'_z) \\ F &= m(\dot{x}' r_y - \dot{y}' r_x) - (I_{zx}\omega'_x + I_{zy}\omega'_y + I_{zz}\omega'_z) \end{aligned}$$

Furthermore, the transformation to the inertial-frame is needed in order to detect the position of the rotor center. This transformation is achieved as follows. Let β be a set of the three Euler angles $\beta = [\varphi\ \vartheta\ \psi]^T$ that describe the orientation of the rotating frame with reference to the inertial frame. $\omega' = [\omega'_x\ \omega'_y\ \omega'_z]^T$ is the vector of the angular velocity in the body-fixed frame. $\underline{\mathbf{R}}(\beta)$ is the rotation matrix as such, that the angular velocity vector ω' can be expressed as a function of the Euler angles and their rate of change $\dot{\beta} = [\dot{\varphi}\ \dot{\vartheta}\ \dot{\psi}]^T$:

$$\omega' = \underline{\mathbf{R}}(\beta)\dot{\beta} \tag{3.47}$$

This transformation allows to determine the angular velocities in the body-fixed frame with respect to the inertial frame of reference[2]. It is also indispensable in order to achieve the conversion of linear velocities and forces between the inertial frame and the rotating frame. In order to achieve this mapping, intrinsic elementary rotations are applied in a definite sequence with the assumption that, initially, the axes of the body-fixed frame lay aligned with the axes of the inertial frame. Additionally, two intermediate coordinate systems $(O - x_1y_1z_1)$ and $(O - x_2y_2z_2)$ are defined. Secondly, assuming that the order of rotations occurs as follow:

- a rotation with an angle ϑ around y-axis transforming the coordinate system from $(O - xyz)$ to $(O - x_1y_1z_1)$,
- a rotation with an angle φ about the x_1-axis transforms the coordinate system from $(O - x_1y_1z_1)$ to $(O - x_2y_2z_2)$,
- and a rotation with the angle ψ around the z_2-axis transforms the coordinate system from $(O - x_2y_2z_2)$ to $(O - x'y'z')$.

These transformations are summarized in Figure 3.20. Moreover, the rate of change of the Euler angles $\dot{\vartheta}$, $\dot{\varphi}$, and $\dot{\psi}$ are respectively the instantaneous angular velocities about y-axis, x_1-axis and z_2-axis. In order to express the angular velocities ω'_x, ω'_y and ω'_z in terms of the rate of change of the Euler angles the following process should be applied:

- $\vec{\dot{\theta}}$ transforms its direction from being along y-axis to y_2-axis and then to y'-axis,
- $\vec{\dot{\phi}}$ transforms its direction from being along x_1-axis to x'-axis
- and the last rotation is the spinning around the z'-axis with the angular velocity $\dot{\psi}$, which, in the case of a constant rotor rotational speed Ω around z'-axis, can be simplified to $\dot{\psi} = \omega_z = \Omega$.

---

[2] It is important to note that the rate of change of Euler angles are not the same as the angular velocities in the inertial-frame. Some references define them however interchangeably. This is only correct for the case of infinitesimal Euler angles, which is assumed to be the case in this work. In both cases, due to the assumption that the rotor spins at a constant angular speed Ω, it is permitted to always consider $\dot{\psi} = \omega'_z = \omega_z = \Omega$.

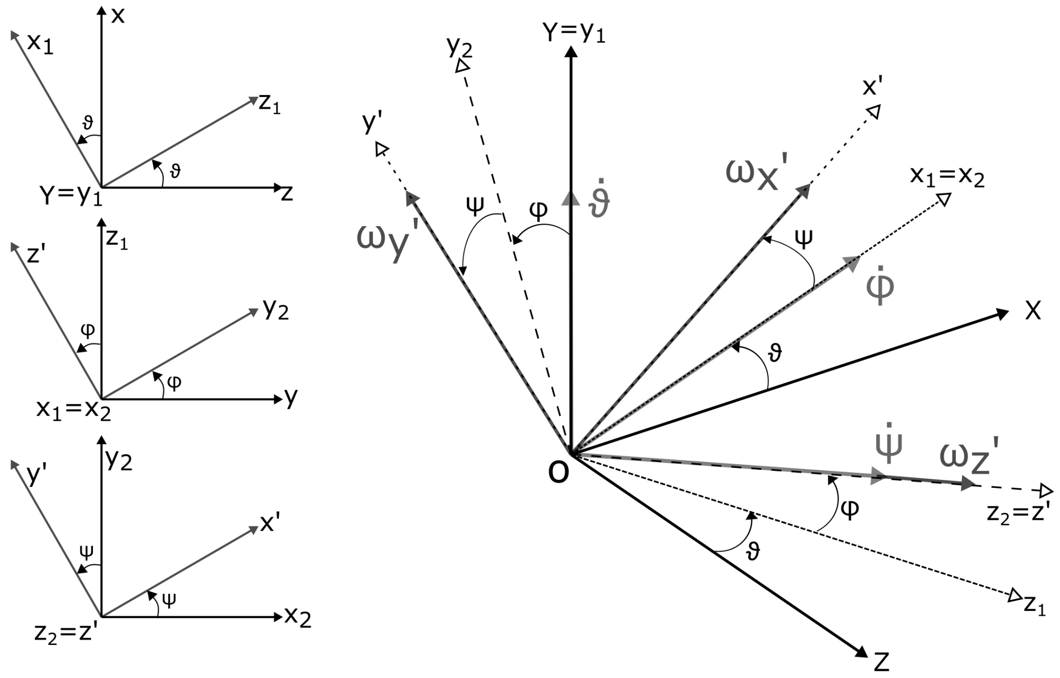

Figure 3.20: Elementary rotations and Euler angles.

Explained here briefly, is an elementary rotation of a rotating coordinate system with a constant angular velocity Ω around a fixed axis z. As seen in Figure 3.21, the displacement in the inertial frame in terms of the displacement in the rotating frame:

$$\begin{aligned} x &= x' cos(\Omega t) - y' sin(\Omega t) \\ y &= x' sin(\Omega t) + y' cos(\Omega t) \\ z &= 1 \end{aligned} \tag{3.48}$$

The transformation from the inertial frame to the body-fixed frame can thus be obtained in matrix form:

$$\begin{bmatrix} x' \\ y' \\ z' \end{bmatrix} = \begin{bmatrix} cos(\Omega t) & sin(\Omega t) & 0 \\ -sin(\Omega t) & cos(\Omega t) & 0 \\ 0 & 0 & 1 \end{bmatrix} \begin{bmatrix} x \\ y \\ z \end{bmatrix} \tag{3.49}$$

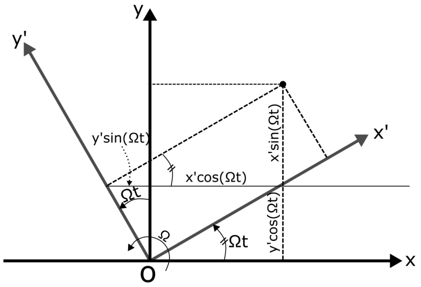

Figure 3.21: Relating the rotating frame and the inertial frame.

The sequence of transformations can be written in the following matrix form:

$$\begin{aligned}\begin{bmatrix}\omega'_x\\ \omega'_y\\ \omega'_z\end{bmatrix} = &\begin{bmatrix}cos(\psi) & sin(\psi) & 0\\ -sin(\psi) & cos(\psi) & 0\\ 0 & 0 & 1\end{bmatrix}\begin{bmatrix}1 & 0 & 0\\ 0 & cos(\varphi) & sin(\varphi)\\ 0 & -sin(\varphi) & cos(\varphi)\end{bmatrix}\begin{bmatrix}0\\ \dot{\vartheta}\\ 0\end{bmatrix}\\ &+\begin{bmatrix}cos(\psi) & sin(\psi) & 0\\ -sin(\psi) & cos(\psi) & 0\\ 0 & 0 & 1\end{bmatrix}\begin{bmatrix}\dot{\varphi}\\ 0\\ 0\end{bmatrix}+\begin{bmatrix}0\\ 0\\ \dot{\psi}\end{bmatrix}\end{aligned} \tag{3.50}$$

The transformation of the body-fixed angular velocities in matrix form:

$$\begin{aligned}\begin{bmatrix}\omega'_x\\ \omega'_y\\ \omega'_z\end{bmatrix} &= \begin{bmatrix}cos(\psi) & sin(\psi)cos(\varphi) & 0\\ -sin(\psi) & cos(\psi)cos(\varphi) & 0\\ 0 & -sin(\varphi) & 1\end{bmatrix}\begin{bmatrix}\dot{\varphi}\\ \dot{\vartheta}\\ \dot{\psi}\end{bmatrix}\\ \omega' &= \underline{\mathbf{R}}(\beta)\ \dot{\beta}\end{aligned} \tag{3.51}$$

The Euler angles can now be determined. First, the rate of change of Euler angles must be determined as functions of the angular velocities ω' in the body-fixed frame:

$$\begin{aligned}\dot{\beta} &= (\underline{\mathbf{R}}(\beta))^{-1}\omega'\\ &= \frac{1}{det(\underline{\mathbf{R}}(\beta))}\begin{bmatrix}cos(\psi)cos(\varphi) & -sin(\psi)cos(\varphi) & 0\\ sin(\psi) & cos(\psi) & 0\\ sin(\psi)sin(\varphi) & cos(\psi)sin(\varphi) & cos(\varphi)(cos^2(\psi)+sin^2(\psi))\end{bmatrix}\omega'\end{aligned}$$

$$\Rightarrow \begin{bmatrix}\dot{\varphi}\\ \dot{\vartheta}\\ \dot{\psi}\end{bmatrix} = \begin{bmatrix}cos(\psi) & -sin(\psi) & 0\\ \frac{sin(\psi)}{cos(\varphi)} & \frac{cos(\psi)}{cos(\varphi)} & 0\\ sin(\psi)tan(\varphi) & cos(\psi)tan(\varphi) & 1\end{bmatrix}\begin{bmatrix}\omega'_x\\ \omega'_y\\ \omega'_z\end{bmatrix} \tag{3.52}$$

which gives:

$$\begin{aligned}\dot{\varphi} &= cos(\psi)\omega'_x - sin(\psi)\omega'_y\\ \dot{\vartheta} &= \frac{sin(\psi)}{cos(\varphi)}\omega'_x + \frac{cos(\psi)}{cos(\varphi)}\omega'_y\\ \dot{\psi} &= \omega'_z + sin(\psi)tan(\varphi)\omega'_x + cos(\psi)tan(\varphi)\omega'_y\end{aligned} \tag{3.53}$$

This leads to directly determining the Euler angles in Bond Graph by integrating their rate of change over time:

$$\begin{aligned}\varphi &= \int^t \dot{\varphi}dt\\ \vartheta &= \int^t \dot{\vartheta}dt\\ \psi &= \int^t \dot{\psi}dt\end{aligned} \tag{3.54}$$

Consequently, the elementary rotations can be established. However, the elementary rotations presented in equation 3.50 cannot be directly applied. These rotations account for a precession around the z-axis, followed by a nutation around the x_1-axis and then the proper rotation or spin of the rotor about the z'-axis.

Nevertheless, the Euler angles can be used as Cardan-angles in order to form the elementary rotations. In this case, pitch around x_1-axis, yaw around y-axis and the roll around z'-axis. This is the sequence applied in order to determine the body-fixed angular velocities and it can be explained through equation 3.50 as follow:

$$\begin{bmatrix} 1 & 0 & 0 \\ 0 & cos(\varphi) & sin(\varphi) \\ 0 & -sin(\varphi) & cos(\varphi) \end{bmatrix} \begin{bmatrix} 0 \\ \dot{\vartheta} \\ 0 \end{bmatrix} \tag{3.55}$$

This transforms $\dot{\vartheta}$ direction from being along $y = y_1$-axis to y_2-axis.

$$\begin{bmatrix} cos(\psi) & sin(\psi) & 0 \\ -sin(\psi) & cos(\psi) & 0 \\ 0 & 0 & 1 \end{bmatrix} \begin{bmatrix} 1 & 0 & 0 \\ 0 & cos(\varphi) & sin(\varphi) \\ 0 & -sin(\varphi) & cos(\varphi) \end{bmatrix} \begin{bmatrix} 0 \\ \dot{\vartheta} \\ 0 \end{bmatrix} \tag{3.56}$$

This transforms it further to $y_3 = y'$-axis, which gives the direction of ω'_y.

$$\begin{bmatrix} cos(\psi) & sin(\psi) & 0 \\ -sin(\psi) & cos(\psi) & 0 \\ 0 & 0 & 1 \end{bmatrix} \begin{bmatrix} \dot{\varphi} \\ 0 \\ 0 \end{bmatrix} \tag{3.57}$$

This transforms the direction of $\dot{\varphi}$ from $x_1 = x_2$-axis to $x_3 = x'$-axis, which gives ω'_x. The spin of the rotor is finally accounted for by $[0\;0\;\dot{\psi}]^T$.
The elementary rotations are thus:

$$\begin{aligned} R_{\text{pitch}}(\varphi) &= \begin{bmatrix} 1 & 0 & 0 \\ 0 & cos(\varphi) & sin(\varphi) \\ 0 & -sin(\varphi) & cos(\varphi) \end{bmatrix} \\ R_{\text{yaw}}(\vartheta) &= \begin{bmatrix} cos(\varphi) & 0 & sin(\varphi) \\ 0 & 1 & 0 \\ -sin(\varphi) & 0 & cos(\varphi) \end{bmatrix} \\ R_{\text{roll}}(\psi) &= \begin{bmatrix} cos(\psi) & sin(\psi) & 0 \\ -sin(\psi) & cos(\psi) & 0 \\ 0 & 0 & 1 \end{bmatrix} \end{aligned} \tag{3.58}$$

There are two measures that can be performed or tested in order to check whether the Euler angles are appropriate for this defined case:

- First, by deriving the rotational kinetic energy of the rotor, under the assumption that the Euler angles are infinitesimal and thus correspond to the rotor angular velocities in the inertial-frame. The kinetic energy T_2 due to the inclination of the rotor in this case is:

$$T_2 = \frac{1}{2} m (I_{zz}\omega'^2_z + I_d\omega'^2_y + I_d\omega'^2_x) \tag{3.59}$$

By substituting equation 3.51 into equation 3.59, the kinetic energy due to the rotational motion becomes:

$$T_2 = \frac{1}{2}m(I_{zz}(\dot{\psi}^2 + \dot{\theta}^2 sin^2(\phi) - 2\dot{\psi}\dot{\theta}sin(\phi)) + I_d(\dot{\phi}^2 + \dot{\theta}^2 cos^2(\phi))) \tag{3.60}$$

Since these inclinations are presumed to be small enough, thus $sin(\phi) = \phi$, $sin^2(\phi) = 0$ and $cos(\phi) = 1$, and by applying $\dot{\psi} = \Omega$:

$$T_2 = \frac{1}{2}m(I_{zz}(\Omega^2 - 2\Omega\dot{\theta}\phi) + I_d(\dot{\phi}^2 + \dot{\theta}^2)) \tag{3.61}$$

Yields the proper rotational kinetic energy T_2 of this rotor configuration.

- Secondly, by running the simulation and plotting the rate of change of Euler angles over time, qualitatively they should have a similar course as in Figure 3.22.

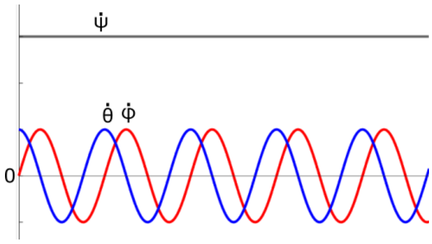

Figure 3.22: Qualitative plot of the Euler-angles rates.

- Thirdly, the formula of the Euler angle applied in Bond-graphs should be suitable for the iterative calculation, which means no denominator in Equation 3.53 should be zero at any iteration.

Due to the infinitesimal Euler angles φ and ϑ and at a constant spin speed, the rotation matrix can be defined interchangeably as such:

$$\underline{\mathbf{R}} = \underline{\mathbf{R}}(\beta) = R_{\text{pitch}}(\varphi)R_{\text{yaw}}(\vartheta)R_{\text{roll}}(\psi) \tag{3.62}$$

As dictated by Karnopp[2], the transformation can then be applied to the linear and angular velocities as well as the forces and torques:

$$\begin{aligned} v &= \underline{\mathbf{R}}\, v' \\ \omega &= \underline{\mathbf{R}}\, \omega' \\ \underline{\mathrm{F}}' &= \underline{\mathbf{R}}^T\, \underline{\mathrm{F}} \\ \underline{\tau}' &= \underline{\mathbf{R}}^T\, \underline{\tau} \end{aligned} \tag{3.63}$$

In the Bond Graph model, these transformations are instituted by using a modulated transformer (MTF). Eventually, the centripetal forces $-m \times \omega_z \times (\omega_z \times r_G)$, caused by the acceleration of the rotor center of gravity due to the radial forces at the bearings[18], are added in a simplified form through a modular source of effort element (**MSe**) such as, the output effort is:

$-m\cdot\omega_z^2[e\cdot cos(\omega_z t)\ \ e\cdot sin(\omega_z t)\ \ 0\ 0\ 0\ 0]^T$.
This element is connected directly to the scalar 1-element representing the velocities of the rotor center.
This entire modeling procedure is summarized in Figure 3.23.

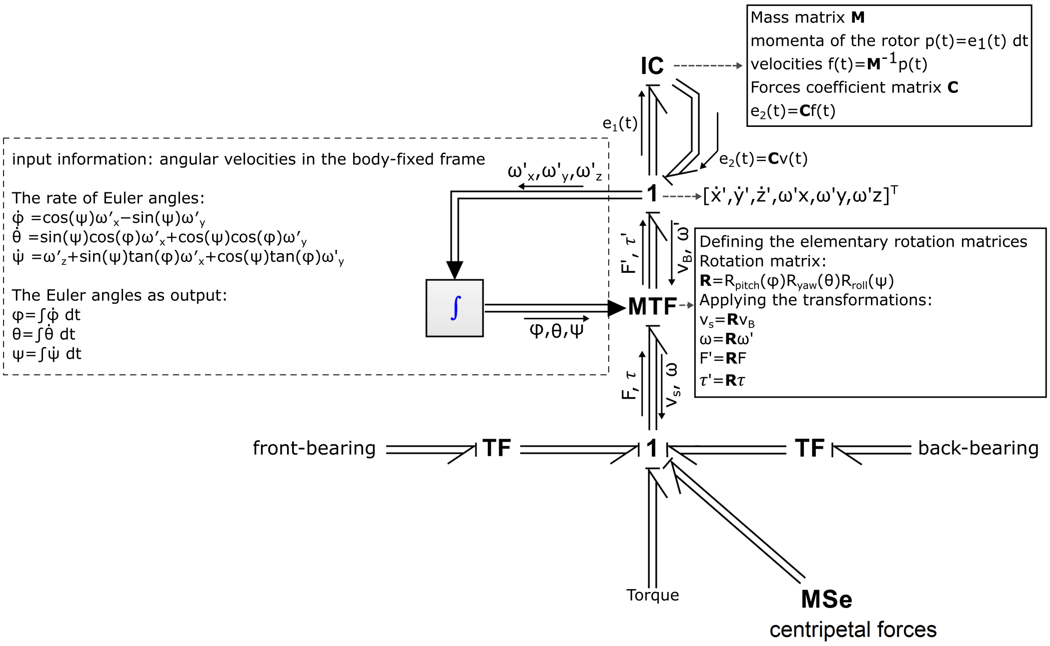

Figure 3.23: Model (D): Bond-Graph layout of the inertia element of the rotor center with regard of the transformation from the body-fixed frame to the inertial-frame (see Figure A.5).

Model variations

By observing how the quasi-Lagrange's equations are derived and then applied to obtain the EOM 3.42, a debate arises. It is argumented whether the frame transformation is required for the rotational DoF. Thus, considering a model variation of (D) denoted (E), where the only difference is that the frame transformation is exclusively used on the translational velocities and forces. Nonetheless, the Bond-graph layout of (E) remains unchanged from that of model (D) as can be seen in Figure A.5,

It is even further argued that a frame transformation might even be unnecessary, and that the 1-element defining the rotor center velocities should be directly connected to the IC-element determined in model (D), but by defining a rotating static unbalance, precisely $r_G^T = [e \cdot cos(\Omega t) \;\; e \cdot sin(\Omega t) \;\; 0]$. This variation is designated as model (F) where the MTF-element representing the frame transformation is completely removed.

This last variation present a conflict with the common knowledge of modeling a rotor in an inertial-frame of reference. Accordingly, another possibility of customizing the model (D) still stands. This is achieved by eliminating the fictitious or apparent forces when omitting any reference to the body-fixed frame. The mass matrix remain unchanged while the forces coefficient matrix $\underline{\mathbf{C}}$ is reduced in this case to include only the centrifugal and gyroscopic forces:

$$\underline{\mathbf{C}} = \begin{bmatrix} 0 & -m[[\omega]r] \\ 0 & m[[v]r] - [\underline{\mathbf{I}}\omega] \end{bmatrix} \tag{3.64}$$

Besides, the static eccentricity is now subjected to rotation, hence again $r_G^T = [e \cdot cos(\Omega t) \;\; e \cdot sin(\Omega t) \;\; 0]$. This variation is denoted as model (G). Despite the differences in the IC-elements, it has a similar Bond-graph layout to model (F) as presented in FigureA.6.
In table 3.1 is a brief comparison of the main distinctions between model (D) and its variations.

Model	includes (or not)				
	apparent forces			frame transformation	
	Euler forces	Coriolis forces	centrifugal forces	translational velocities and forces	angular velocities and moments
(D)	x	x	x	x	x
(E)	x	x	x		x
(F)	x	x	x		
(G)	x		x		

Table 3.1: Brief comparison of model (D) and its variations

Test models

First, the Bond-graph example of a Stadola-Green rotor presented by Pedersen[12] is directly tested to this study case. The used general equations of motion were applied in the body-fixed frame and are stated here for convenience:

$$\begin{bmatrix} m\underline{E} & -m[r] \\ m[r] & \underline{I} \end{bmatrix} \begin{bmatrix} \dot{v} \\ \dot{\omega} \end{bmatrix} + \begin{bmatrix} \underline{0} & -m[v] - m[[\omega]r] \\ -m[[\omega]r] - m[v] & m[[v]r] - [\underline{I}\omega] \end{bmatrix} \begin{bmatrix} v \\ \omega \end{bmatrix} = \begin{bmatrix} f_1 \\ f_2 \end{bmatrix} \tag{3.65}$$

This form of EOM was then utilized in the IC-element in model (D). As a matter of fact, this reference was basic to the modeling methodology of model (D).

Also, the Eulerian-junction structure as presented by Karnopp *et al.*[2] can, theoretically, be directly applied to test the model response at 0 (rpm). By considering the deviation of the center of gravity as presented for a general plane motion of a rigid body, and the obtained expression of the momenta, the net forces and torques acting on the body are:

$$\begin{aligned} F &= \frac{\partial p}{\partial t} + \omega \times p \\ \tau &= \frac{\partial L}{\partial t} + \omega \times L \end{aligned} \tag{3.66}$$

$$\begin{aligned} F_x &= m\ddot{x} + m\omega_y\dot{z} - m\omega_z\dot{y} \\ F_y &= m\ddot{y} + m\omega_z\dot{x} - m\omega_x\dot{z} \\ F_z &= m\ddot{z} + m\omega_x\dot{y} - m\omega_y\dot{x} \end{aligned} \tag{3.67}$$

$$\begin{aligned} \tau_x &= I_{xx}\dot{\omega}_x + \omega_y I_{zz}\omega_z - \omega_z I_{yy}\omega_y \\ \tau_y &= I_{yy}\dot{\omega}_y + \omega_z I_{xx}\omega_x - \omega_x I_{zz}\omega_z \\ \tau_z &= I_{zz}\dot{\omega}_z + \omega_x I_{yy}\omega_y - \omega_y I_{xx}\omega_x \end{aligned} \tag{3.68}$$

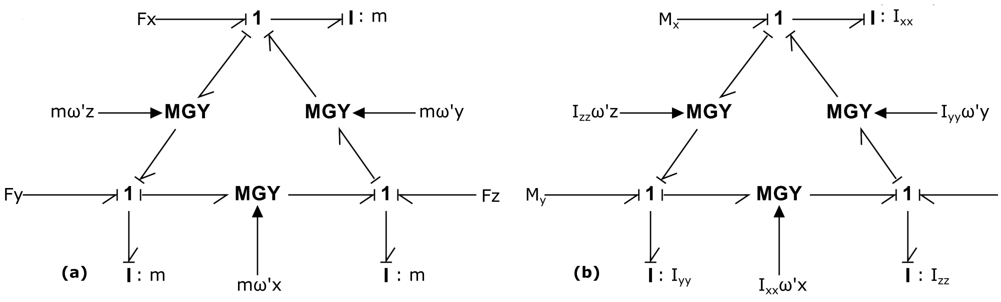

Figure 3.24: Bond-Graph model representing the gyrator ring constructions: (a) translation, (b) rotational Dof.

Additionally, for the purpose of comparison to the EOM derived from the quasi-Lagrange's equations, the Euler equations as presented can be exploited to reach the equations of motion in matrix form in a similar manner to equations 3.42.

$$\begin{aligned} p &= m(v+\omega\times r_G) \\ \Rightarrow F &= \frac{\partial p}{\partial t}+\omega\times p \\ &= m\dot{v}_G+\omega\times m(v+\omega\times r_G) \\ &= m\dot{v}-[r]m\dot{\omega}+\omega\times(mv-[r_G]m\omega) \\ &= m\dot{v}-[r]m\dot{\omega}+[\omega]mv-m[[\omega]r_G]\omega \end{aligned} \tag{3.69}$$

$$\begin{aligned} L &= \underline{I}\omega+r_G\times mv \\ \Rightarrow \tau &= \frac{\partial L}{\partial t}+\omega\times L \\ &= \underline{I}\dot{\omega}+[r_G]m\dot{v}+\omega\times\underline{I}\omega+\omega\times r_G\times mv \\ &= \underline{I}\dot{\omega}+[r_G]m\dot{v}-[\underline{I}\omega]\omega+[[\omega]r_G]mv \end{aligned} \tag{3.70}$$

Assembling the equations into matrix form:

$$\begin{bmatrix} m\underline{\mathbf{E}} & -m[r] \\ m[r] & \underline{I} \end{bmatrix}\begin{bmatrix} \dot{v} \\ \dot{\omega} \end{bmatrix}+\begin{bmatrix} m[\omega] & -m[[\omega]r] \\ m[[\omega]r] & -[\underline{I}\omega] \end{bmatrix}\begin{bmatrix} v \\ \omega \end{bmatrix}=\begin{bmatrix} f_1 \\ f_2 \end{bmatrix} \tag{3.71}$$

As can be seen, this leads again to the general matrix form of the equations of motion, however different, and can yet be tested again in the IC-element of the built model (D).

Throughout this section, several models were presented to describe the dynamics of a rotor by means of Bond-graphs. The focus points were implementing the unbalance forces and moments, as well as the gyroscopic effects. In the following, the models are evaluated and investigated by testing and comparing the outcome to the provided experimental results.

Study case parameters

The collected geometrical data and parameters needed for the modeling are summarized in the table below.
The CAD model of the rotor shows an axial deviation Z_G of the center of gravity G from the origin of an initially defined coordinate system along the z-axis such as $G(0,0,-4.4355234\cdot 10^{-2})$ mm. According to this the ideal inertia tensor $\underline{I}_0$ can be defined in two different manners. First, in reference to the center of gravity:

$$\begin{aligned}\underline{I}_0 &= \begin{bmatrix} I_{xx} & 0 & 0 \\ 0 & I_{yy} & 0 \\ 0 & 0 & I_{zz} \end{bmatrix} \\ &= \begin{bmatrix} 5.433619\cdot 10^{-7} & 0 & 0 \\ 0 & 5.4336191\cdot 10^{-7} & 0 \\ 0 & 0 & 6.5495134\cdot 10^{-7} \end{bmatrix} (\mathrm{kg}\cdot\mathrm{m}^2)\end{aligned} \tag{3.72}$$

Secondly, in reference to the defined coordinate system:

$$\underline{I}_0 = \begin{bmatrix} 5.4338246\cdot 10^{-7} & 0 & 0 \\ 0 & 5.4338248\cdot 10^{-7} & 0 \\ 0 & 0 & 6.5495134\cdot 10^{-7} \end{bmatrix} (\mathrm{kg}\cdot\mathrm{m}^2) \tag{3.73}$$

Description	Data	
Effective mass m of the rotor	0.010453015 kg	
Mass imbalances	static eccentricity	46.73 µm
	tilt angle	0.0344 rad
Front-bearing		
Distance to the rotor center L_1	12.45564477 mm	
Radial stiffness $K_{radial} = k_{y1} = K_{x1}$	990 N/m	
Axial stiffness $K_{axial} = k_{z1}$	1980 N/m	
Tilt stiffness $K_{tilt} = k_{R1}$	−0.53 N m/rad	
Magnetic eccentricities		
Initial lateral deflection e_S	x-direction	$e_{Sx} = -4\,\mu\mathrm{m}$
	y-direction	$e_{Sy} = 7\,\mu\mathrm{m}$
Radial deflection during operation e_R	66 µm	
Back-bearing		
Distance to the rotor center L_2	1.944355234 mm	
Radial stiffness $K_{radial} = k_{y2} = K_{x2}$	1210 N/m	
Axial stiffness $K_{axial} = k_{z2}$	2420 N/m	
Tilt stiffness $K_{tilt} = k_{R2}$	−0.17 N m/rad	
Magnetic eccentricities		
Initial lateral deflection e_S	x-direction	$e_{Sx} = 50\,\mu\mathrm{m}$
	y-direction	$e_{Sy} = 3\,\mu\mathrm{m}$
Radial deflection during operation e_R	13 µm	

Table 3.2: Modeling parameters and data.

4 Results and discussion

4.1 Natural free-frequencies and speed map

4.1.1 Natural frequencies obtained from the models

At first, the natural frequencies were determined. For that purpose, a numerical impact test was run by using an impulse signal-generator or by adding an unbalance or an initial force at time t_0 and recording the system response.
The models behaved similarly at 0 (rpm) and delivered almost identical response. After determining the numerical values, a Fast-Fourier transformation (FFT) was applied to the system response. A Fast-Fourier transformation is an efficient algorithm to calculate discrete- (DFT) and inverse discrete-Fourier transformation (iDFT). It allows to convert the signal or system response from time domain to frequency domain. Afterwards, the percentual relative error ϵ_r was then calculated for each value as $\epsilon_r = \left|1 - \frac{\omega_{0,numerical}}{\omega_{0,empirical}}\right| \cdot 100\%$.
By means of error and trial, the radial stiffness at the front-bearing had to be adjusted to a lower value $k_{y1} = K_{x1} = 790\,\mathrm{N/m}$ in order to reach fairly comparable natural-frequencies to the ones determined experimentally. This reduction was considered acceptable for the modeling. The results obtained are summarized in table 4.1. Although the response amplitudes were not examined, they are graphically presented in the amplitude-frequency plots along the Campbell-diagrams in Figures A.7-A.12.

Front radial stiffness (N/m)		$k_{y1} = K_{x1} = 990$	$k_{y1} = K_{x1} = 790$
Natural-frequencies (rpm)	Empirical	Numerical	
$\omega_{0,1}$	2690	2652	2584.482
relative error ϵ_r (%)	-	1.413	3.9226
$\omega_{0,2}$	4844	5454	4846.938
relative error ϵ_r (%)	-	12.593	0.06065

Table 4.1: Natural frequencies obtained from the models.

4.1.2 Natural frequencies speed-map: Campbell-diagrams

Principally, the natural-frequencies speed maps (Campbell-diagram) were established for each model. This was achieved by applying a Fast-Fourier transformation (FFT) to the model response over an array of rotational speed Ω ranging from 0 (rpm) to 5000 (rpm) with an increment of 100 (rpm), and for a measurement duration of 10 seconds each. These responses were obtained by implementing the static eccentricity to generate an unbalance force as an exciting source instead of using an impulse-signal. The experimentally determined Campbell-diagram

in the thin yellow plots overlap with the numerical ones that appear in the background with the color purple. This was accomplished, in such manner, with the intention to have a direct and more explicit graphical comparison or validation as exhibited in the following figures.
The Campbell-diagrams of the models (A) and (B) are identical as can be seen in Figures 4.1a and 4.1b. In fact, model (A) and (B) behave identically overall and accordingly, the results of their simulations will be presented combined.

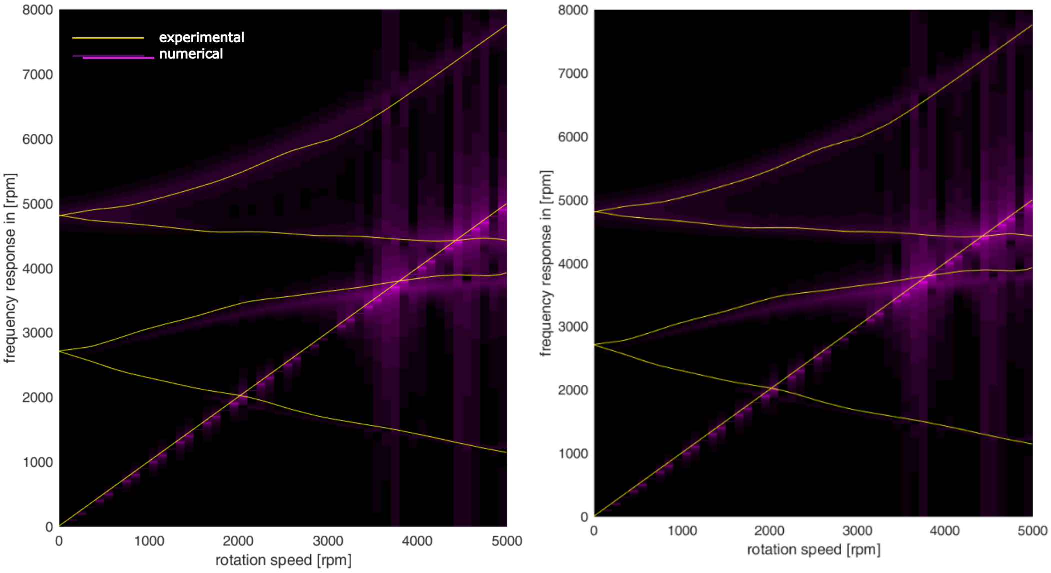

(a) Model (A).

(b) Model (B).

Figure 4.1: Campbell-diagrams obtained from model (A) and (B).

Model (C) delivered the following Campbell-diagram:

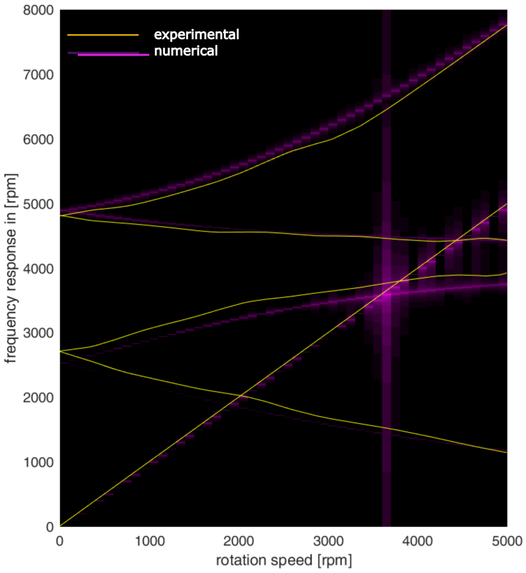

Figure 4.2: Campbell-diagram obtained from Model (C).

As for model (D), it can be noticed in Figure 4.3a that the FW of the first mode has an elevated frequency response starting at around 2500 (rpm) in comparison to the experimental plot. Several variations were tested in order to try identifying what might be contributing to this rise in the Forward-Whirling frequencies, essentially by alternating the expressions of the gyroscopic effect. This was achieved , for instance, by opting for the ideal inertia tensor or using a reduced gyroscopic matrix, or even by trying a combination of both. The obtained Campbell-diagram is viewed in Figure 4.3b.

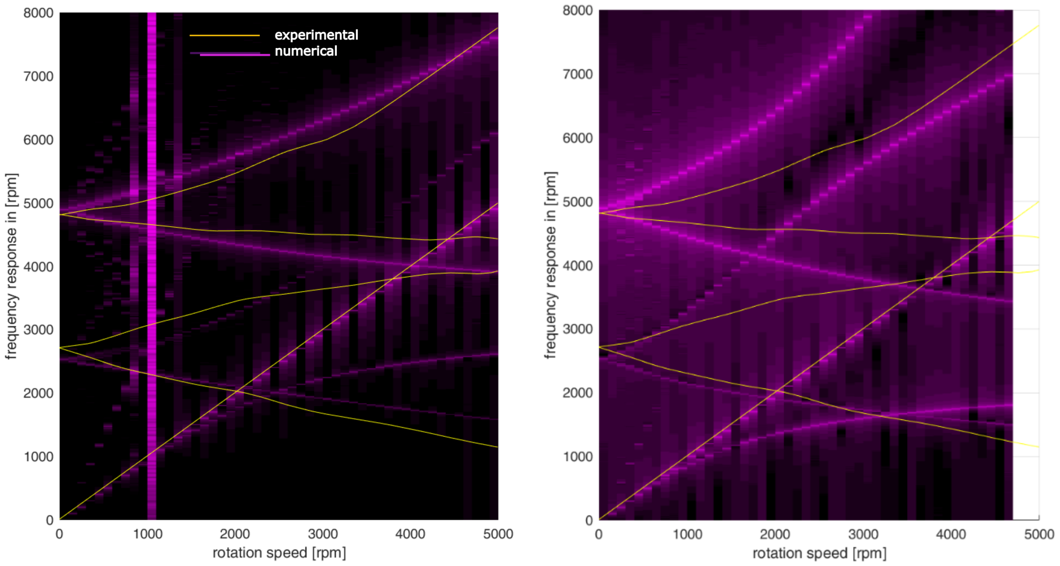

(a) Model (D).

(b) Testing model (D) using an ideal inertia tensor.

Figure 4.3: Campbell-diagrams of model (D) and test case.

As for the Campbell-diagram obtained from the model variation (E):

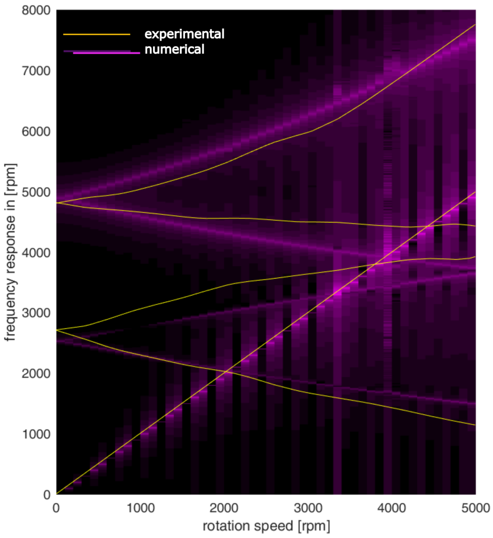

Figure 4.4: Campbell-diagram obtained from model (E).

Finally, the Campbell-diagrams that were obtained through models(F) and (G) are neatly identical and are displayed here below.

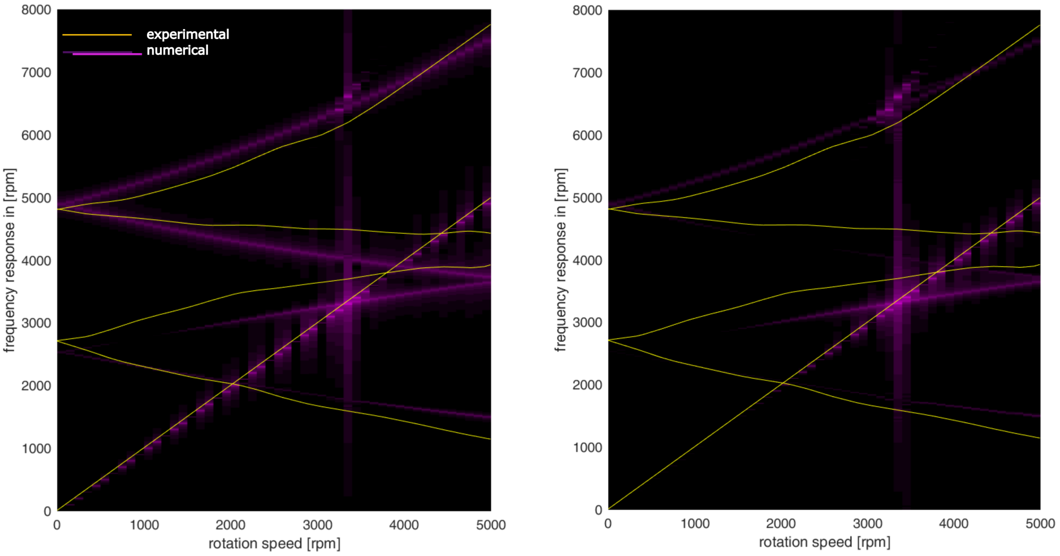

(a) Model (F). (b) Model (G).

Figure 4.5: Campbell-diagram obtained from Model (F) (similarly from model (G)).

Eventually, two modeling approaches that depend on using the derived frame transformation were tested based on the literature. Starting by deriving and applying the equations of motion exactly as provided in the work of Pedersen (2009) in the first trial. Then, the gyrator ring-construction as specified by Karnopp *et al.*[2] was directly employed in a second test model.

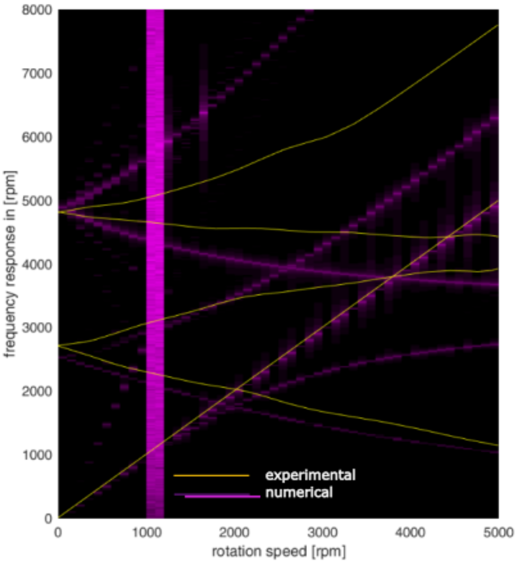

Figure 4.6: Campbell-diagram obtained from the test models.

These approaches yield Campbell-diagrams that are quite similar to each other, but nevertheless, with obvious and large deviation from the anticipated outcome as can be observed in Figure 4.6.

Unfortunately, applying the modeling approaches provided by Pedersen[12] and Karnopp *et al.*[2] resulted in rather a discouraging outcome. Nevertheless, the first reference[12] was further investigated to comprehend the limitations that causes such off results. By re-deriving the quasi-Lagrange's equations of motion, the term $-\frac{\partial T}{\partial r}$ in the quasi-Lagrange's equations should not be disregarded as it contributes to the Coriolis forces in the rotating body. This accentuates the importance of considering all the apparent forces acting in the rotating frame of reference. Based on this disclosure, opting to a similar approach as demonstrated in section 3.1.3 resulted in model (D). Still, and as observed in Figure 4.3a, the course of the forward-whirl of the first mode starts to increase abruptly at approximately 2500 (rpm). This suggests one of the following explanations:

- First, that one or the combination of these apparent forces, and due to their dependency on the rotational velocity, contribute energy to the forward-whirl of the first mode which causes its frequency ascent or deviation.
- Secondly, that bond-graph treats the frame-transformation other than expected. Actually, it is noticed that when applying the frame-transformation, the angular velocities around the x- and y-axes display a constant offset from zero at the start of the simulations. The angular velocities $\dot{\phi}$ and $\dot{\theta}$ oscillate then around this offset value.

Based on this perception, a model variation (E) is tested where the frame-transformation was applied only to the linear velocities and forces. A validated Campbell-diagram was then obtained as shown in Figure 4.4. At this stage and in a model variation (F), the frame-transformation was completely omitted. However, in such cases, the fictitious forces should be disregarded in the modeling. For this reason, a model (G) with a reduced forces-coefficient matrix, where only the gyroscopic and centrifugal forces were considered, was tested. These two models resulted also in validated and identical Campbell-diagrams as displayed in Figure 4.5. Approved natural-frequency diagrams were likewise accomplished through models (A) and (B) as presented in Figures 4.1a and 4.1b.

Another information that need to be mentioned, is that the sign of the term contributing to the gyroscopic matrix had to be inverted from a minus sign to a plus sign in model (D) and its variations, otherwise the model would not have functioned.

The critical speeds can then be read directly from the Campbell-diagrams at the intersections between $D : \Omega = \omega$ and the precessional frequencies of the FW and BW. These critical speeds were defined approximately at $\omega_{c1} = 1945.5$ (rpm), $\omega_{c2} = 3941.5$ (rpm) and $\omega_{c3} = 4456.5$ (rpm).

When determining the Campbell-diagram, a simple form of the correct layout of the models is sufficient. After all, it is only the natural free-frequencies that needs to be obtained by performing an impact test. However, this is obviously not the case when examining the unbalance responses of the rotor models. Here, all the unbalances present in the rotor should be implemented in addition to the adjusted damping coefficients provided in table 4.2, as well as the apparent forces or the centripetal forces depending on the used frame of references.

4.2 Orbit response

The simulations were set to run for 60 seconds and then compared to a run of 5 minutes, the resultant displacements converge fairly comparable in both cases. Thus opting for the first case, the orbits for the last revolution were generated at different speeds 1100, 2100, 3100, 4100 and 5100 (rpm). These speeds were chosen mainly below and above each of the critical speeds. The rotation is counterclockwise. The displacement orbits obtained from the models at the rotor center were plotted and are shown in the following figures.

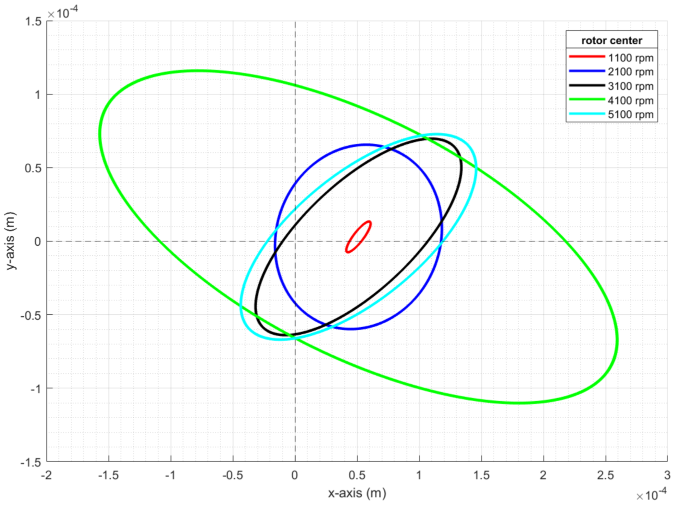

Figure 4.7: Model (A), (B): Displacement orbits at the rotor center.

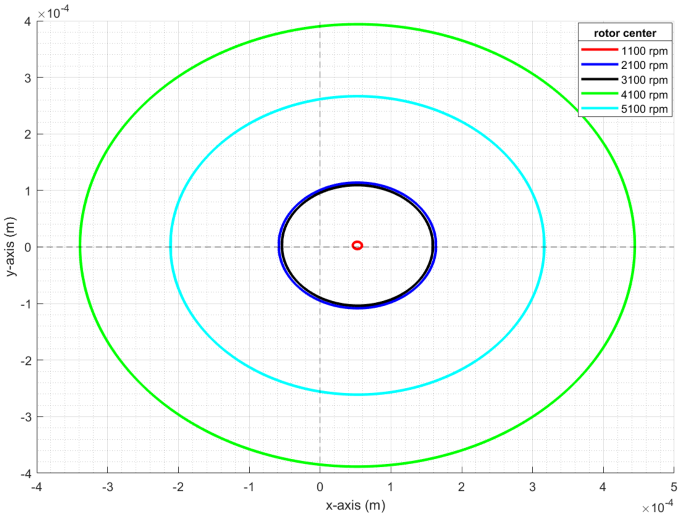

Figure 4.8: Model (C): Displacement orbits at the rotor center.

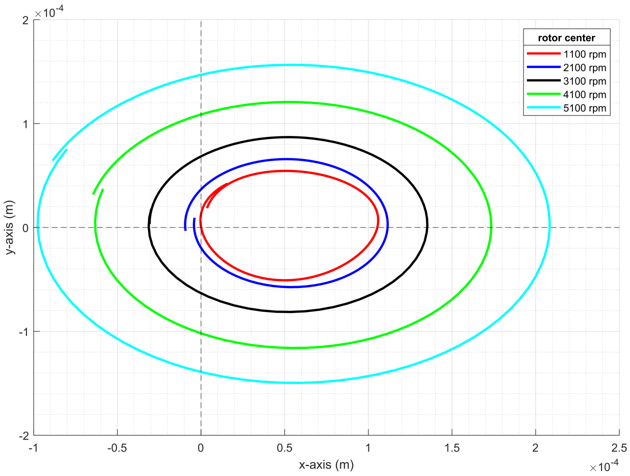

Figure 4.9: Model (D): Displacement orbits at the rotor center.

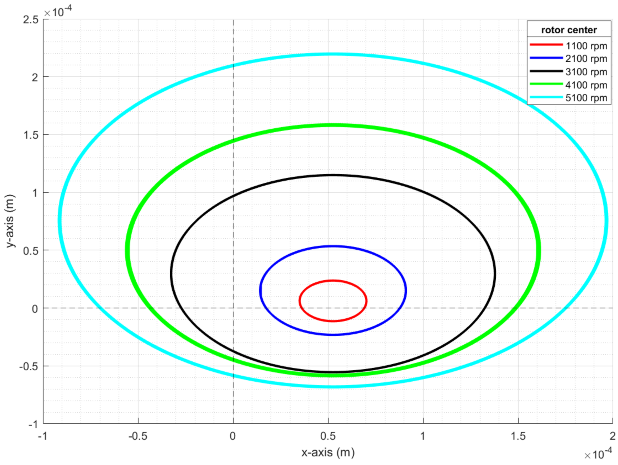

Figure 4.10: Model (E): Displacement orbits at the rotor center.

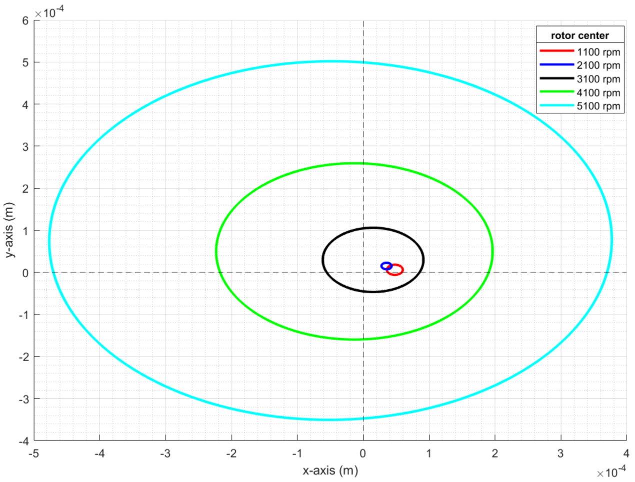

Figure 4.11: Model (F): Displacement orbits at the rotor center.

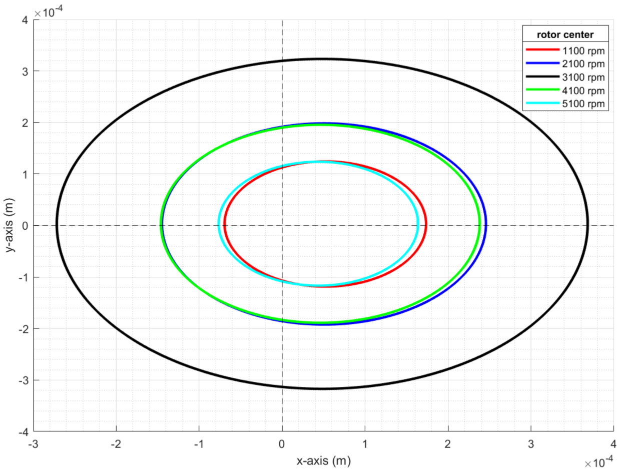

Figure 4.12: Model (G): Displacement orbits at the rotor center.

Initially, it can be noticed that the orbits are elliptical which emphasizes the asymmetry of the rotor. Moreover, when the rotor traverses a critical speed it should show a rise in amplitude and a shift in phase[11]. While the phase shift was not examined, the amplitude increase is mostly observed in the numerical models that exhibit resonance as presented in Figure 4.13. For instance, model (A) (simultaneously (B)) shows resonance at approximately 1900 and 3700 (rpm). Consequently, a rise in the orbital displacement when crossing from 1100 to 2100 (rpm), and from 3100 to 4100 (rpm) can be recognized. This can also be detected for the models (F) and (G) that show resonance respectively at around 2000 and 4200, and at 3000 (rpm). Model (C) exhibits however one orbit amplification when crossing over 2000 (rpm). Model (E) and (D) show rather monotonically increasing lines, thus in turn, their orbit plots appear to only increase in amplitude with the rotational speed as seen in Figures 4.9 and 4.10.

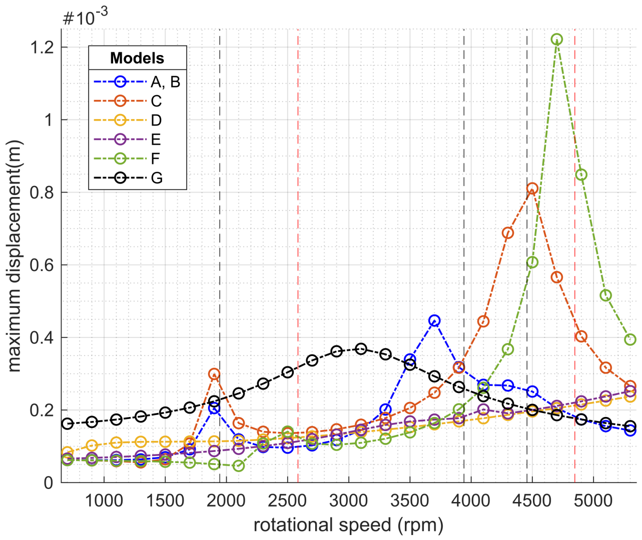

Figure 4.13: Maximum displacements obtained from the numerical models at the rotor center.

4.3 Unbalance response

In the following the unbalance response of the seven models were investigated by examining the mean and maximum displacements at two positions. Experimentally, the maximal displacements at two defined edges in the rotor were provided in addition to the mean displacement measurements along the x- and y-axes and their corresponding standard deviations. The front edge lies at the coordinate $z_f = -13.956$ mm displaced at 13.912 mm from the rotor center, and the back edge at $z_b = -1.046$ mm displaced at 1.00124 mm from the rotor center. The velocities and displacements at any position in the rotor can be detected in Bond-Graphs by joining a 1-element to the center through a TF-element with modulus the position of that edge relative to the center as shown in Figure 4.14. The values acquired from the numerical simulations were converging after 10 seconds. Thus, the mean and maximal displacements were determined directly using Matlab by omitting the initial phase of the displacements[1]. The simulations were recognized to run stable using the backward differentiation formula (BDF) as an integration method with a time step of 10^{-6} seconds and an output each 10^{-5} seconds.

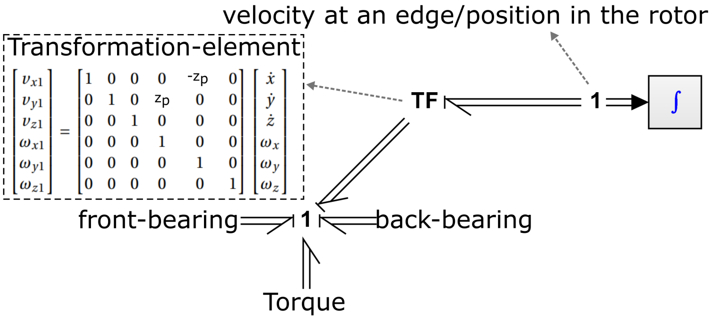

Figure 4.14: Locating a position in the Bond-graph model

The dimensionless proportionality damping coefficients at both bearings were adjusted through trial and error. The values that yield the most fitting outcome are presented in the table 4.2.

Model	(A), (B)	(C)	(D)	(E)	(F)	(G)
Damping coefficient μ	0.2	$2 \cdot 10^{-4}$	10^{-5}	$5 \cdot 10^{-4}$	10^{-4}	10^{-3}

Table 4.2: Fitted proportionality damping coefficients for each model.

Figures 4.15-4.18 show the mean displacement obtained from the models plotted against the experimentally determined ones along the x- and y-axes over the rotational speed at both the front- and back-edge. The vertical error bars account for the standard deviations determined from the experimental measurements.

---

[1] The values provided in tables A.1-A.6 were rounded to six decimal places

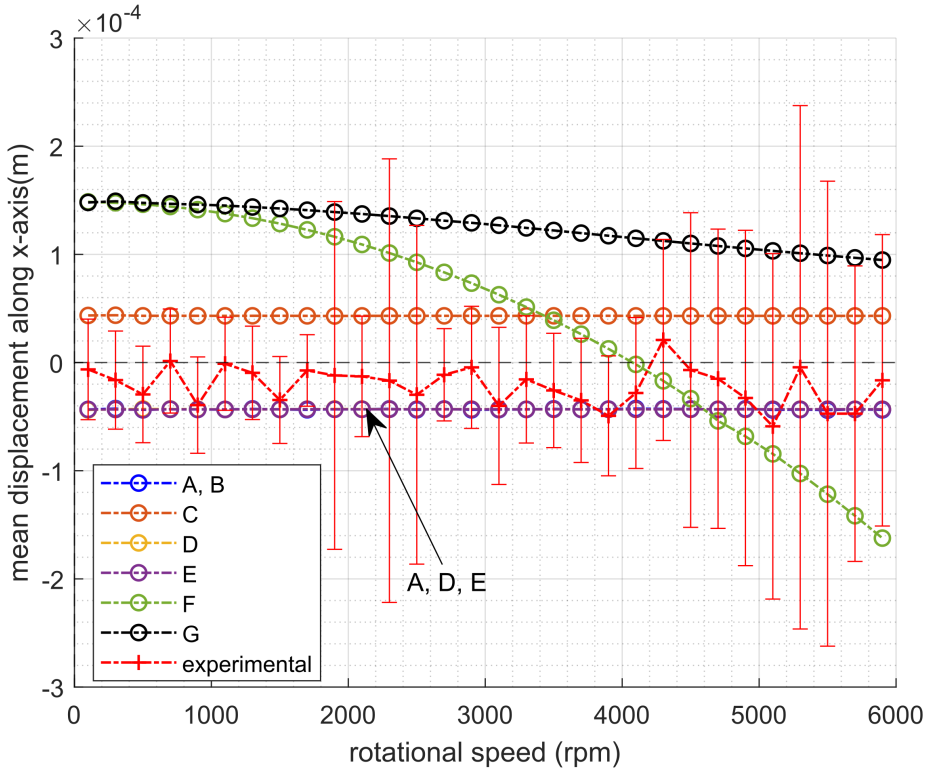

Figure 4.15: Mean displacement at the front-edge along the x-axis

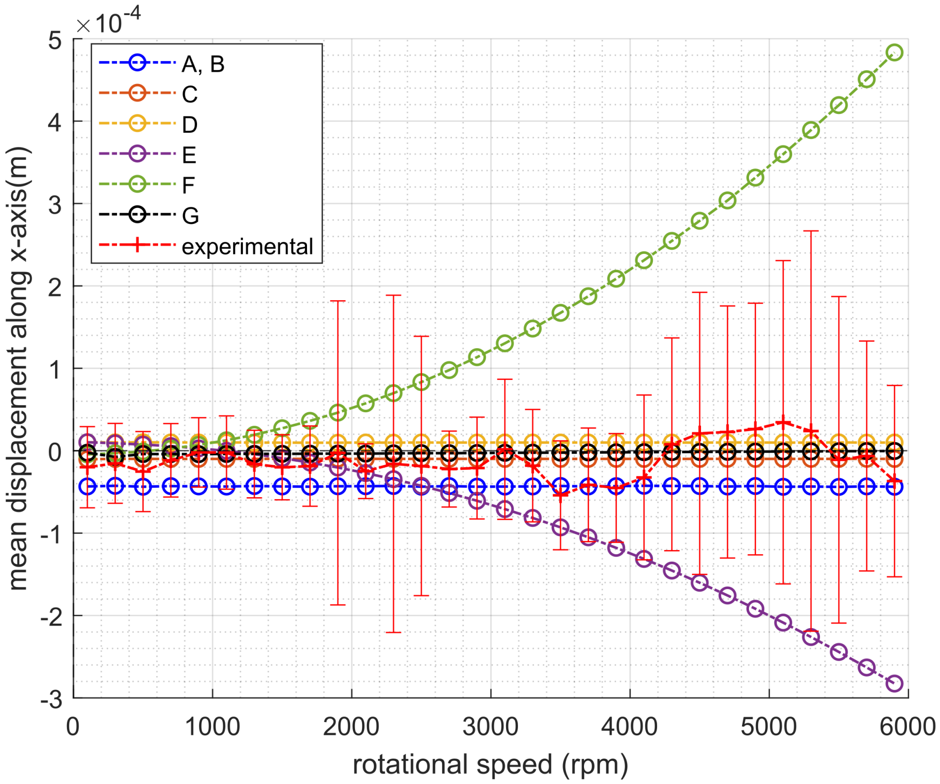

Figure 4.16: Mean displacement at the front-edge along the y-axis

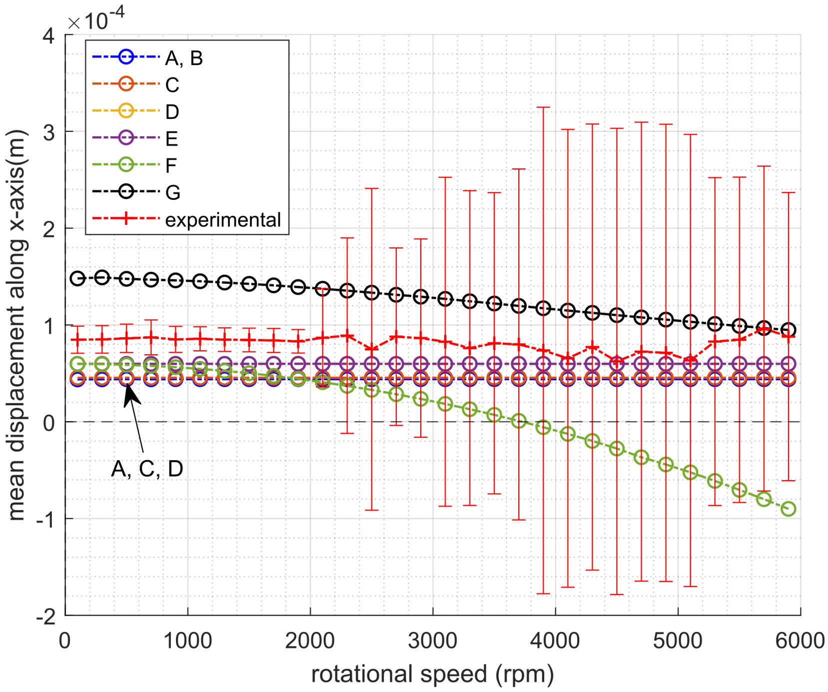

Figure 4.17: Mean displacement at the back-edge along the x-axis

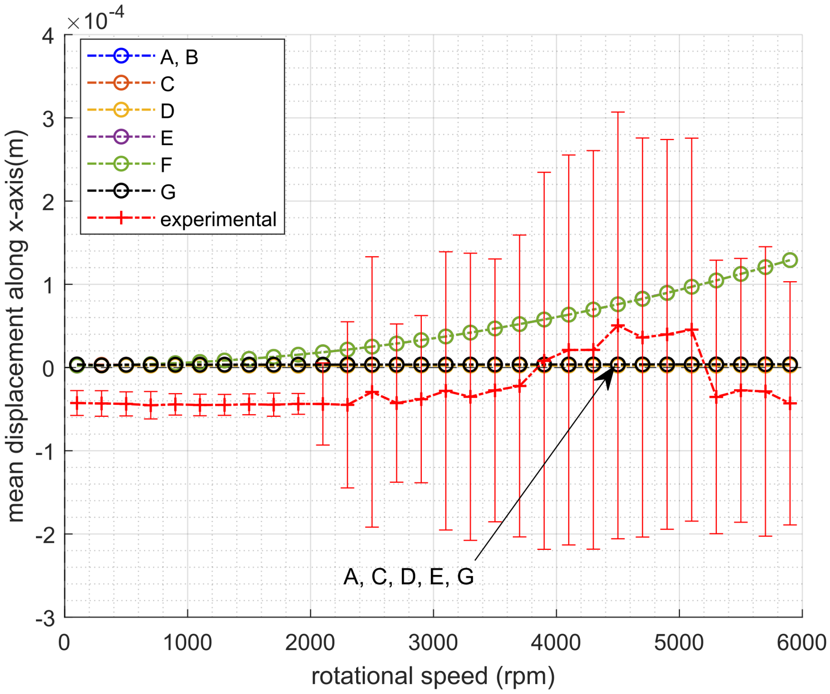

Figure 4.18: Mean displacement at the back-edge along the y-axis

In the following, the maximum displacements of the lateral motion obtained from each model were plotted against their experimental counterparts over the rotational speed. The vertical black dashed lines represent the critical speeds.

The numerical natural-free frequencies are as stated in table 4.1 $\omega_{0,1} = 2584.482$ (rpm) and $\omega_{0,2} = 4846.938$ (rpm) and added through the vertical red dashed lines.

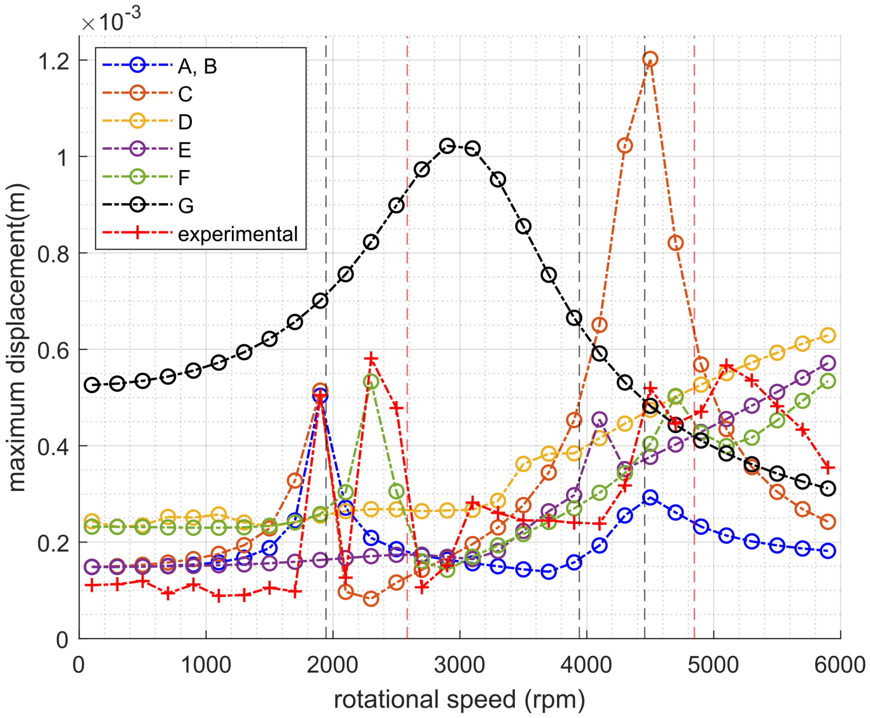

Figure 4.19: Maximum displacements at the front-edge

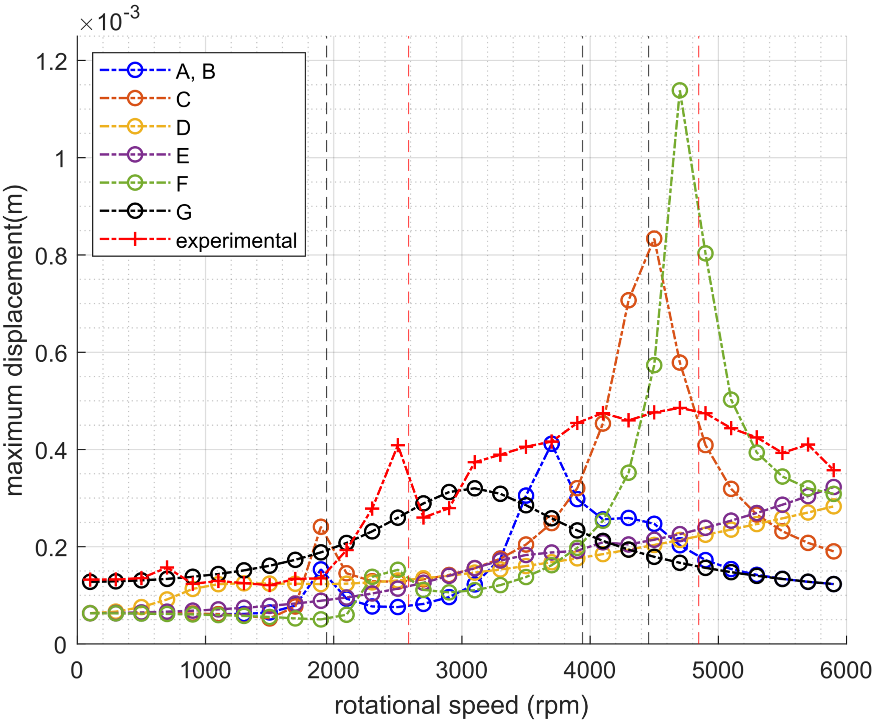

Figure 4.20: Maximum displacements at the back-edge

By observing the plots of the mean displacements, models (A), (B), (D) present the most satisfactory results in general. Apart from the obvious offset viewed at the front-edge along the x-axis, model (C) shows also a tendency to fit the experimental results. Similarly for model (E) that shows only a decreasing mean displacement at the front-edge along the y-axis. Besides, it can be noticed that model (F) delivers results that are rather divergent. The averaged displacement decreases with an increase in the spin velocity of the rotor along the x-axis while increasing along the y-axis at the front- and at the back-edge but by remaining in the range of the standard deviations for the latter. The mean displacements obtained from model (G) show a deviation from the experimental results along the x-axis in the front- and back-edge while delivering adequate results at the y-axis for both edges.
Most importantly, the maximum displacements or amplitudes of the responses were investigated in order to determine resonance sites and the modeled rotor behavior at the critical speeds. When it comes to the maximum displacements at the front-edge, relatively adequate results were obtained from model (A), (C) and (F), with (F) yielding the best fitting results to the experimental ones as can be observed from Figure 4.19. As for the maximum displacements at the back-edge presented in Figure 4.20, model (A), (C) and (F) delivered bearable results where an amplitude rise can be marked at two sites for each. Here, the course of the maximum displacement from model (F) tends to have a similar development to the experiment despite the non-matching amplitudes.
The most detectable aspect from the numerically obtained amplitude-frequency plots is the lack of amplitude rise and resonance sites in comparison to the experimentally provided ones.

Through the resultant unbalance responses that were determined from the models, it is evident that several deficiencies must be pinpointed. These limitations might explain in turn the inconsistency and disagreement between the numerical and experimental results. First of all, the magnetic bearings of the rotor were modeled as having linear dynamic behavior, this disproves the non-linear properties they manifest in reality. This linearization is to some degree responsible for the distinct outcome of the unbalance response[5]. Besides, the role of axial control ensured by the active magnetic bearings was not implemented and therefore not inquired to verify if it might largely influence the obtained results.

Moreover, since no information about the damping effects of the bearings were given, stiffness-proportional damping coefficients were used to describe the damping behavior of the bearings. The proportionality coefficients for each model were determined through error and trial, they were adjusted along the simulations in order to reach a relatively adequate response of the system over the rotational speed and were assumed to be equal for both bearings. However and as examined through the amplitude-frequency plots in Figures 4.19 and 4.20, a damping coefficient value that produces an acceptable response at one of the edges results simultaneously in an improper response at the other edge. Moreover, some controversial observations were noticed through these attempts to tune the damping coefficients for each numerical model, such as, an occasionally slight reduction in their values causes rather a large damping effect where the resonance is no longer observed. Whereas increasing the damping coefficients beyond a certain threshold causes substantial response instability. Altogether, varying the damping coefficients of the numerical models had little to no effect on the averaged displacements. Undoubtedly, these reports underline the necessity to perform a parametric study concerning the damping features of the bearing.

It is important to note that due to the existence of the tilt, the inertia tensor takes the unbalanced form, this cancels the assumption of the axis-symmetric rotor. This asymmetry of the rotor models is accentuated by the obtained elliptical shapes of the orbits responses[11]. This makes it troublesome to determine at which critical speeds does the resonance occur for the numerical models. The reason for that is, a backward whirling is unlikely to produce a critical speed[11], this premise is even reinforced in the case of an axial-symmetric rotor[18]. By acknowledging that and by noticing that the unbalance responses of the models show less resonance sites than expected, a detailed look into the experimentally determined maximum displacements might provide a better insight. On one side, three critical speeds can be extracted from the Campbell-diagram and its validated numerical counterparts. On the other side, the experimentally provided maximum displacements do not exhibit resonance or amplitude rise at all of the critical speeds. At the front-edge and on first sight, five resonance sites can be identified where the first and fourth ones occur consecutively at the first and third critical speeds. At the back-edge, the main resonance sites cannot be exactly enumerated, a first one occurs at the natural-free frequency of the first mode. Meanwhile, several adjacent resonance sites that cannot be graphically, explicitly characterized encompass the second and third critical speeds as well as the second natural-free frequency. This numerical-experimental discrepancy indicates again the need to resort to a better damping assessment method for the numerical models.

Furthermore, in an asymmetric spinning rotor with mass imbalance, non-conservative, circulatory and destabilizing effects occur due to the unbalance forces and moments and due to the gyroscopic couples. These effects are generally described through skew-symmetric matrices. In the case of an applied perturbation, the mass, stiffness and damping matrices acquire additional skew-symmetric components that are consequential[18] especially in the stiffness matrix. The skew-symmetric components in the mass matrix were included through the coefficients of the Euler forces in the Bond-graph model (D) and its variations, where an IC-element was implemented. However, all the restoring forces were considered to be conservative and were solely added through the stiffness matrix, in other words through the constant stiffness parameters of the bearings. However, even when the rotor is operating at dry, cross-coupled stiffness effects occur, even though these effects are most accentuated when a rotating liquid is flowing through the impeller.

Finally, the internal damping that normally occurs in an operating rotor is complicated and intricate to add to the models. In a rigid rotor, this internal damping is caused mainly due to friction along with structure and manufacturing restrictions. It is also time- and speed-dependent and thus often referred to as hysterectic damping and is considered to be a form of imbalance. When this internal damping reaches or exceeds the bearings' damping, it causes unstable response and might be responsible for the high-response amplitudes in some of the resonance points. Add to that, the rotor models were simulated at a constant rotational velocity. Thus, neglecting the initial operational phase that might trigger subsequent instabilities during operation.

Eventually, there is some criticism that should be addressed at the experimental parameters and results provided by a second party. To begin with, there was no proper description of the given parameters. Besides, a full assessment of the experimental results is missing. Apart from the standard deviation of the mean displacements in the x- and y-directions, no further interpretation of the experimental measurements was provided. A good communication of the experimental setups and parameters as well as an adequate results evaluation would had definitely helped investing more time on the modeling part and the evaluation of the numerical results, and less time on deciphering the data.

5 Conclusion and outlook

This thesis task focused on developing Bond-graph models that depict the characteristic phenomena observed in the dynamics of a dry-operating rotor by means of Bond-graph modeling implemented in the software 20-sim. The models presented were mostly based on applying either Newtonian mechanics, Newton-Euler equations or the energy method through Lagrangian dynamics. Besides, this work can be considered, partly, as a comparative study. Some of the models or exploited procedures were the result of applying modeling recommendations or existing methods from the literature. These models were expected to deliver ideal exemplaries or endorse setting a clear methodology for rotordynamics modeling in Bond-graphs. However and by comparing to the experimental results, the initial outcome obtained from these test models demonstrated the need to, not only to further improve them, but also to review and inspect the methods by which they were established.

Modeling the rotor in operation at dry should be extensively investigated and optimized. This task is actually crucial. The reason for that is the added complexity due to the hydrodynamic forces and the cross-coupled effects that have to be considered, when the pump is running at its operation points. In this sense, the rational of Bond-graph enables handling and adding the gyroscopic effects, as well as the unbalance forces and moments due to the existing mass imbalance and tilt. These are characteristic aspects in rotordynamics. Actually, Bond-graph, as a modeling approach, displayed a considerable flexibility and efficiency that can be witnesses throughout this study and other more sophisticated, published works.

Moreover, one of the main distinction between the models is opting solely to modeling in the inertial frame or implementing a frame transformation from the inertial-frame to the body-fixed frame. The latter investigates whether including the apparent forces occurring in a rotating coordinate system is more meaningful to the modeling of phenomena in rotating structures. Generally, modeling in the inertial-frame seemed to deliver validated natural frequency diagrams. Through the obtained unbalance responses, this study demonstrated that resorting to modeling in the inertial-frame, by applying the EOM determined through Newton's second law as is the case in model (A), or as in model (C) by using the full form of the unbalanced inertia tensor, yielded quite adequate results. Whereas, when modeling the motion in the rotating frame of reference, it is imperative to include not only the unbalance forces and moments but also all the apparent forces such as the Euler-, Coriolis and centrifugal forces. In this case, discarding the frame transformation and adding the centripetal forces seems so far to be the most promising approach as was the case of the presented model variation (F). While this arrangement requires a supplementary examination, it seemed as if Bond-graph treated the rotation matrix in a certain manner as a co-

efficient instead of a transformation matrix.
Nevertheless, it is very clear through this work and the limitations thereof, that several refinements must be performed. The lack of important data such as the damping properties of the magnetic bearings justify the potential to further test and enhance the models. Despite selecting a stiffness-proportional damping, and having the damping coefficients determined and adjusted through error and trial for seven models, a parametric study could not be carried out due to time constraints. Unless accurate damping and stiffness coefficients of the bearings are provided, an exhaustive parametric analysis that focuses on the damping behavior of the bearings should be performed. Such an analysis would be decisive especially when dealing with a type of supporting bearings that are identified to exert non-linear dynamic behaviors. So while modeling rotordynamics can be accomplished using Bond-graph, and since not all the modeling options were exploited due to the case specifications, it is still not conclusive to judge this approach's capability of precisely modeling magnetic levitation in rotors.

To the knowledge of the author, there is still no comprehensive research concluded aiming at a complete validation of a bond-graph rotor model. Out of the seven models that were presented along this work, three of them, which are models (A), (C) and (F), can be built upon and constitute a basis for further studies investigating rigid rotors with different types of supporting bearings. The parameters need then to be updated to fit the study cases. It is emphasized here, once again, that the experimental setups and results should be adequately described and evaluated.

Bibliography

[1] "A Dictionary of Physics."
Oxford University Press, sixth edition, 2009.
ISBN: 978-0-199-23399-1

[2] D. C. Karnopp, D. L. Margolis, R. C. Rosenberg. "System Dynamics, Modeling, Simulation, and Control of Mechatronic Systems ."
John Wiley & Sons Inc, 2012, 5th Edition.
ISBN 978-0-470-88908-4

[3] Werner Roddeck, "Bondgraphen, Modellbildung und Simulation dynamischer Systeme."
Springer Vieweg, 2019
ISBN 978-3-658-25921-1

[4] Graham Foster *et al.*, "Mechanical circulatory and respiratory support"
Elsevier Inc., Academic press, 2018.
https://doi.org/10.1016/B978-0-12-810491-0.00005-9

[5] J.C. Ji, Colin H. Hansen, Anthony C. Zander, ”Nonlinear dynamics of magnetic bearing systems.”
International journal of material systems and structures, Vol. 19, Issue 12, 2008, pp.1471-1491.
DOI: 10.1177/1045389X08088666

[6] Jeff Hillyard, ”Magnetic bearings.”
Joint advanced student school, TUM, 2006.
SlidePlayer.com Inc., 2021

[7] C Blaj, M Greconici, F Barvinschi, ”The influence of the permanent magnets materials on the restoring force of a bearing using magnetic liquid.”
8th International Conference on Electromagnetic Processingof Materials, 2015, Cannes, France.
ffhal-01336036.

[8] A. Mukherjee, R. Karmakar, A. K. Samantaray, "Bond Graph in modelling, simulation and fault identification."
I.K. International Publishing House Pvt. Ltd., 2006
ISBN 81-88237-96-5

[9] M.I. Friswell, J.E.T. Penny, S.D. Garvey and A.W. Lees. "Dynamics of rotating machines."
Cambridge; New York
Cambridge University Press, Cambridge aerospace series 2010.
ISBN 978-0-521-85016-2

[10] Y. Ishida, T. Yamamoto. "Linear and Nonlinear Rotordynamics,
A Modern Treatment with Applications."
Wiley-VCH Verlag I& Co. 2012, 2nd Edition.
ISBN 978-3-527-40942-6

[11] John M. Vance, Fouad Y. Zeidan, Brian Murphy "Machinery Vibration and Rotordynamics."
John Wiley & Sons Inc, 2010
ISBN 978-0-471-46213-2

[12] Eilif Pedersen, "Rotordynamics and bond graphs: basic models"
Mathematical and Computer Modelling of Dynamical Systems Vol.15, No.4, August 2009, pp.337–352
DOI: 10.1080/13873950903063116

[13] J. D.Turner, J. L. Junkins, D. T. Griffith, "Development of general-purpose quasi-coordinate Lagrangian-based multi-body dynamics tool using Automatic differentiation"
ASME International design engineering technical conference, 2005
Paper n°:DETC2005-85641

[14] Aron Wolf Pilaf, "Introduction To Lagrangian Dynamics."
Springer Nature Switzerland AG, 2020
ISBN 978-3-030-22377-9

[15] Roger D. Quinn, "Equations of motion for structures in terms of Quasi-Coordinates"
ASME, Journal of Applied Mechanics, 1990, Vol.57, pp745-749

[16] Leonard Meirovitch, "Fundamentals of vibrations."
McGraw Hill companies, Inc., 2001
ISBN 0-07-041345-2

[17] Lalanne,M. and Ferraris,G., "Rotordynamics prediction in Engineering."
2nd Edition,Wiley, 1997.

[18] Dr. Frederick Nelson, "Rotor Dynamics without Equations".
International Journal of COMADEM, 10(3), July 2007, pp. 2-10.

Indirect References

[19] San Andrés Luis, ”Introduction to Pump Rotordynamics.”
Design and Analysis of High Speed Pumps, 2006, paper 9, pp. 1-26.

[20] Christoph Woernle, "Eine Einfuehrung in die Kinematik und Dynamik von Systemen starrer Koerper."
Springer Berlin Heidelberg, 2011
ISBN 978-3-642-15981-7

[21] Masato Tanaka, Masao Kobayashi, Patrick Keogh, Hiroshi Kanki "Vibrations of rotating machinery."
Springer Berlin Heidelberg, 2019
ISBN 978-4-431-55452-3

[22] R. Gasch . R. Nordmann H. Pfuetzner "Rotordynamik."
second Edition, Springer, 2002
ISBN 3-540-41240-9

List of Figures

List of Tables

Appendices

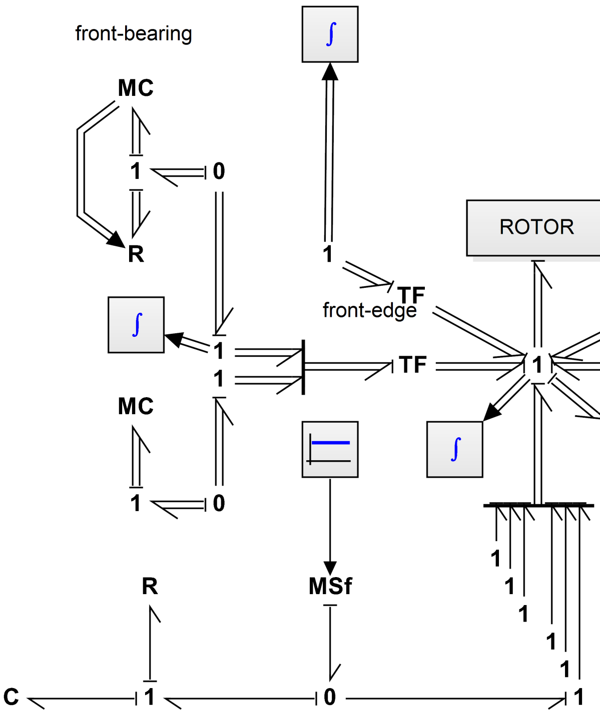

Figure A.1: Bond-graph layout of model (A) (simultaneously of model (B)).

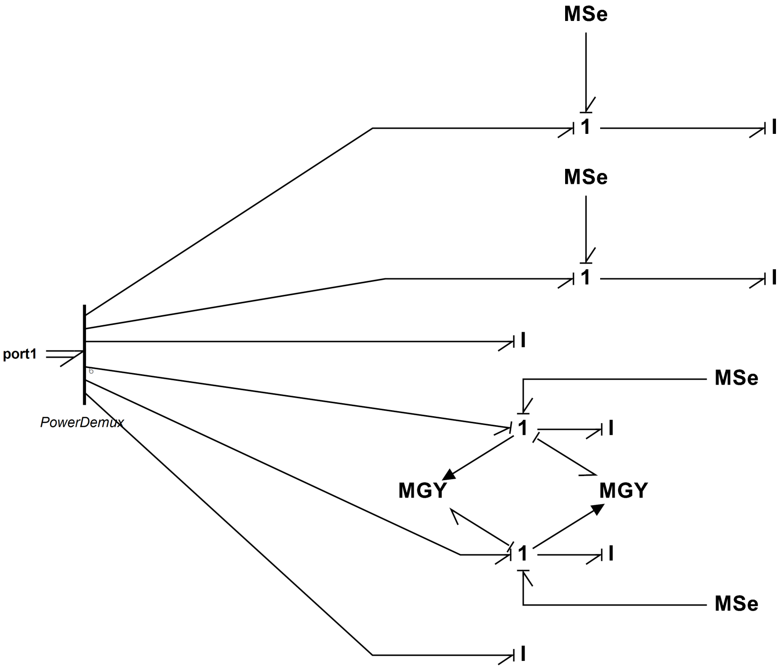

Figure A.2: Bond-graph layout of ”ROTOR” sub-model (A).

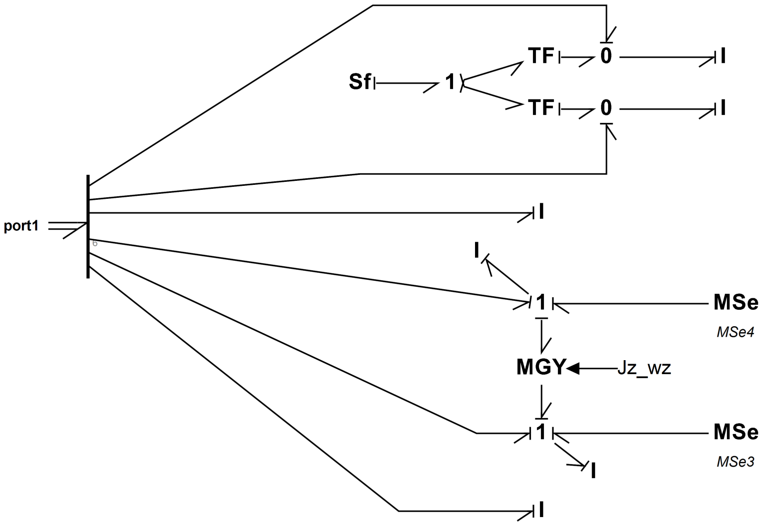

Figure A.3: Bond-graph layout of "ROTOR" sub-model (B).

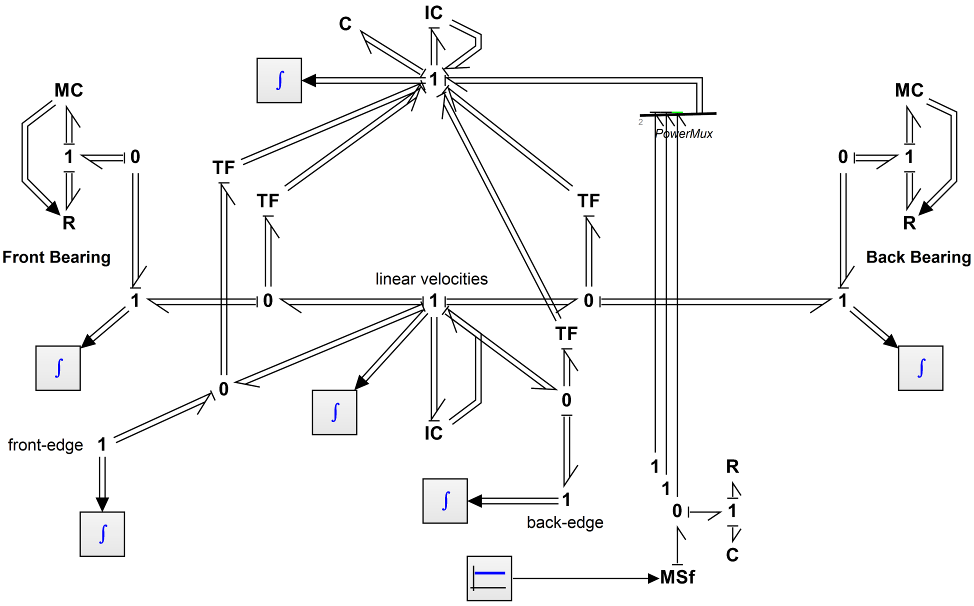

Figure A.4: Bond-graph layout of model (C).

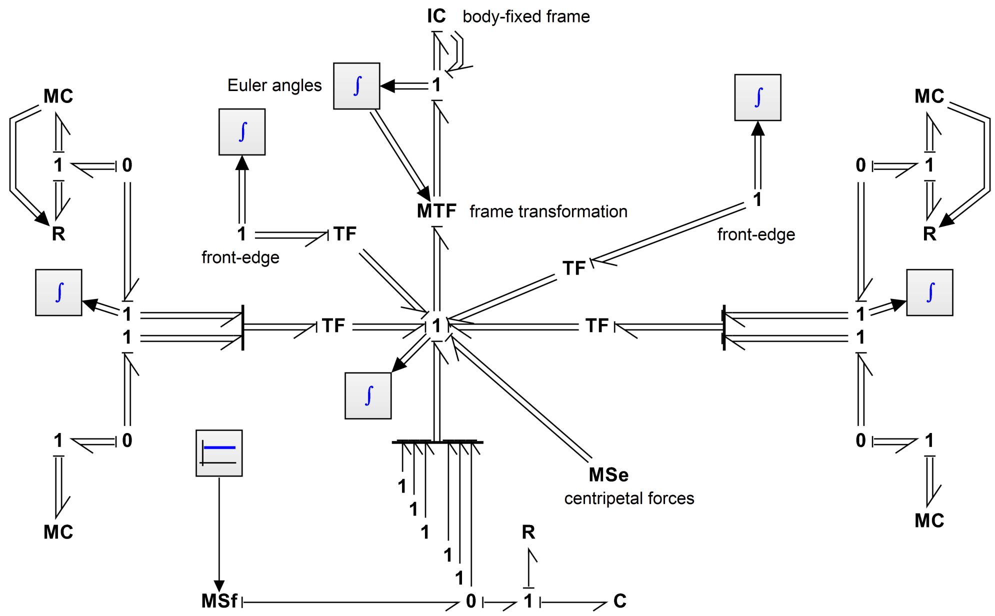

Figure A.5: Bond-graph layout of model (D) (simultaneously of model (E)).

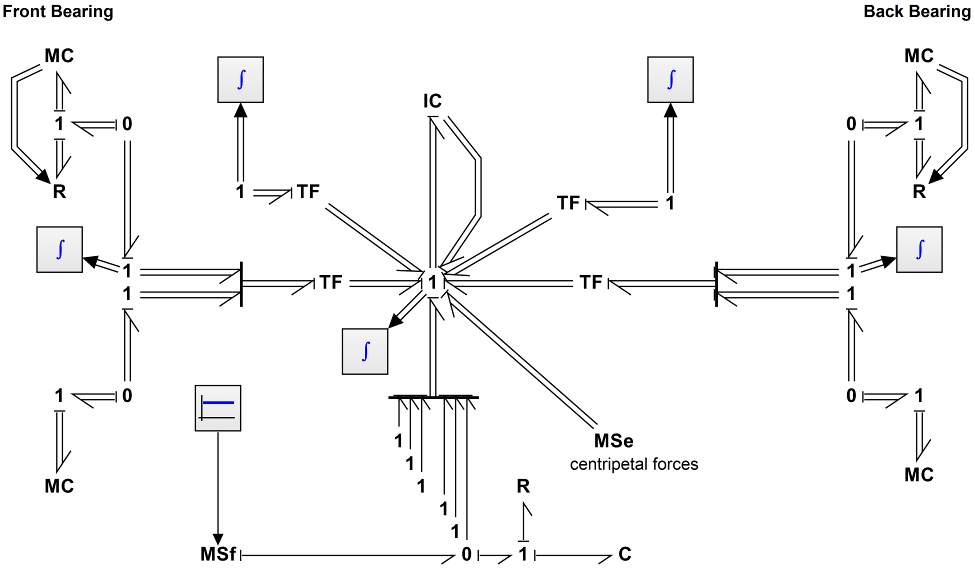

Figure A.6: Bond-graph layout of model (F) (simultaneously of model (G))

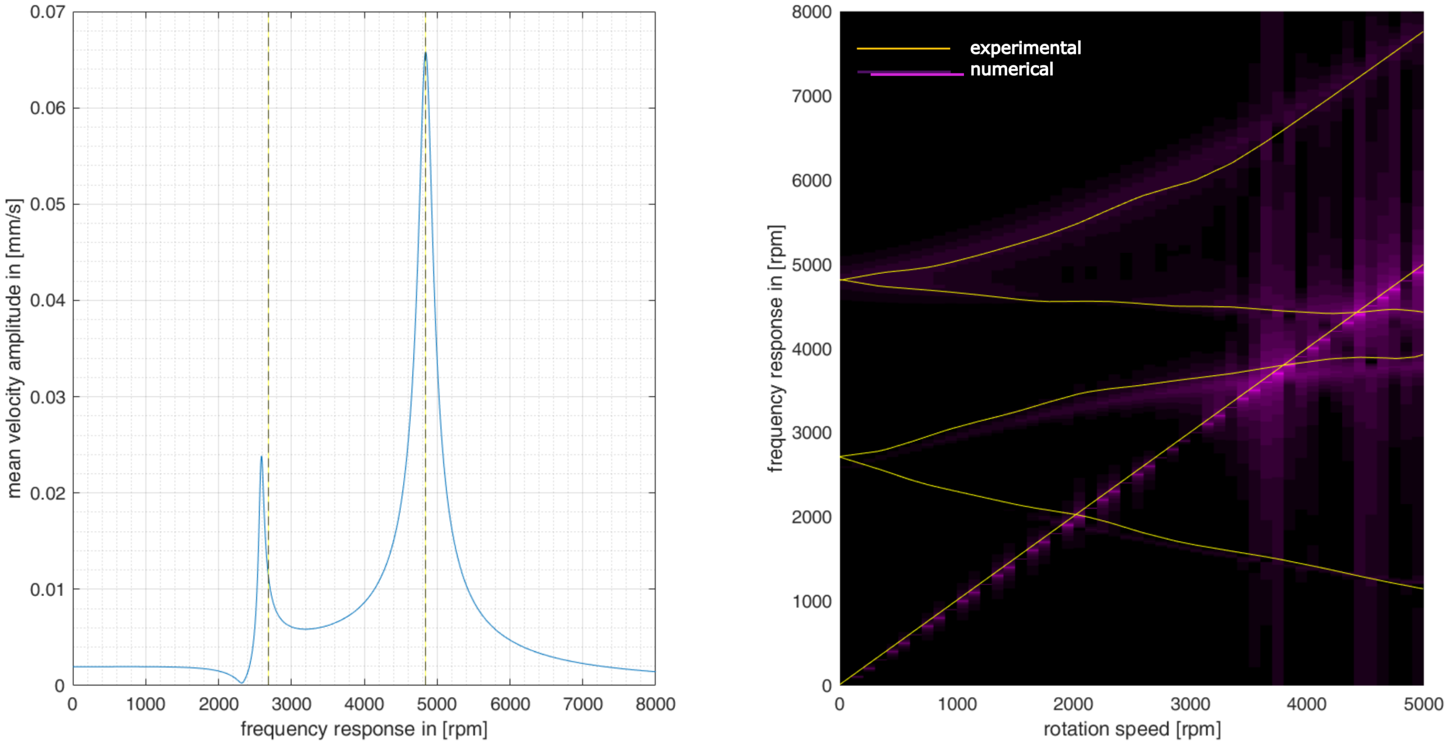

Figure A.7: Campbell-diagrams obtained from model (A).

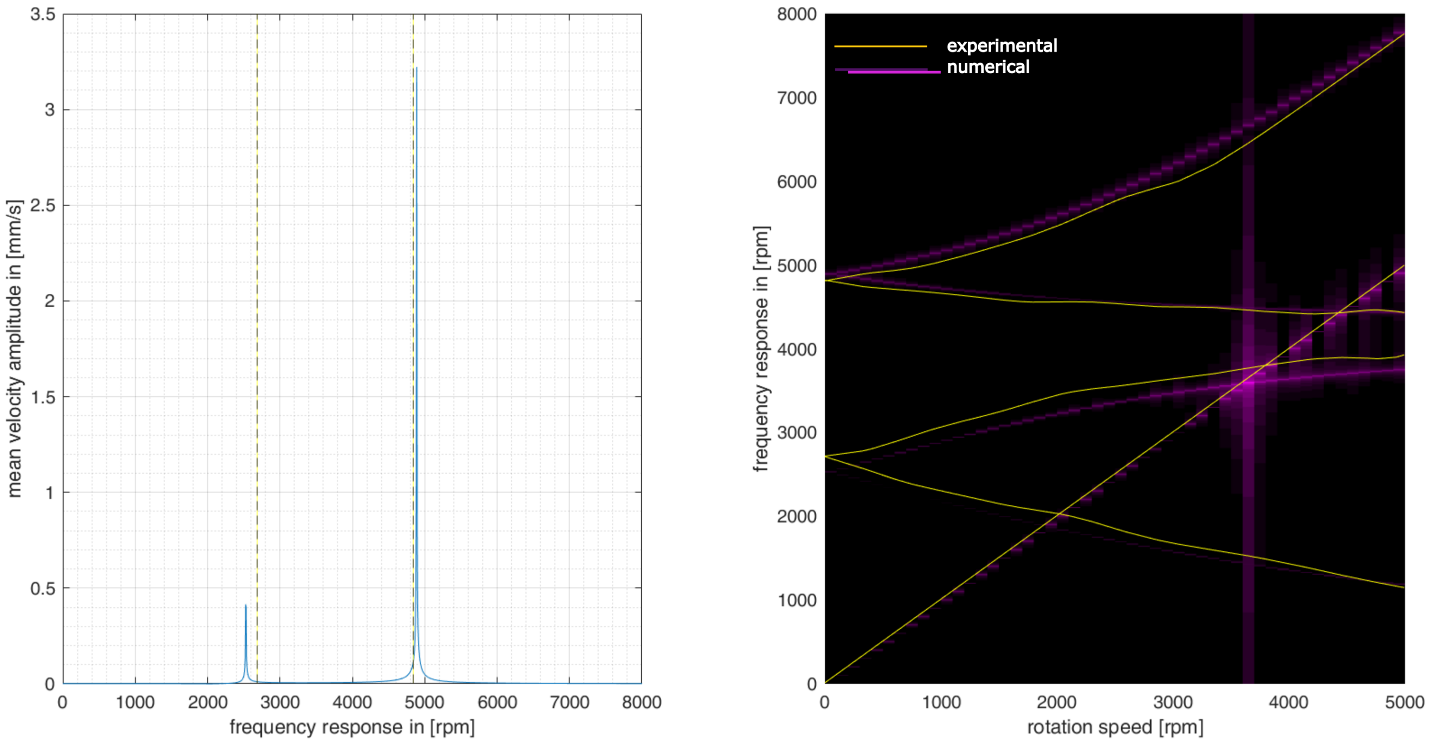

Figure A.8: Campbell-diagrams obtained from model (C).

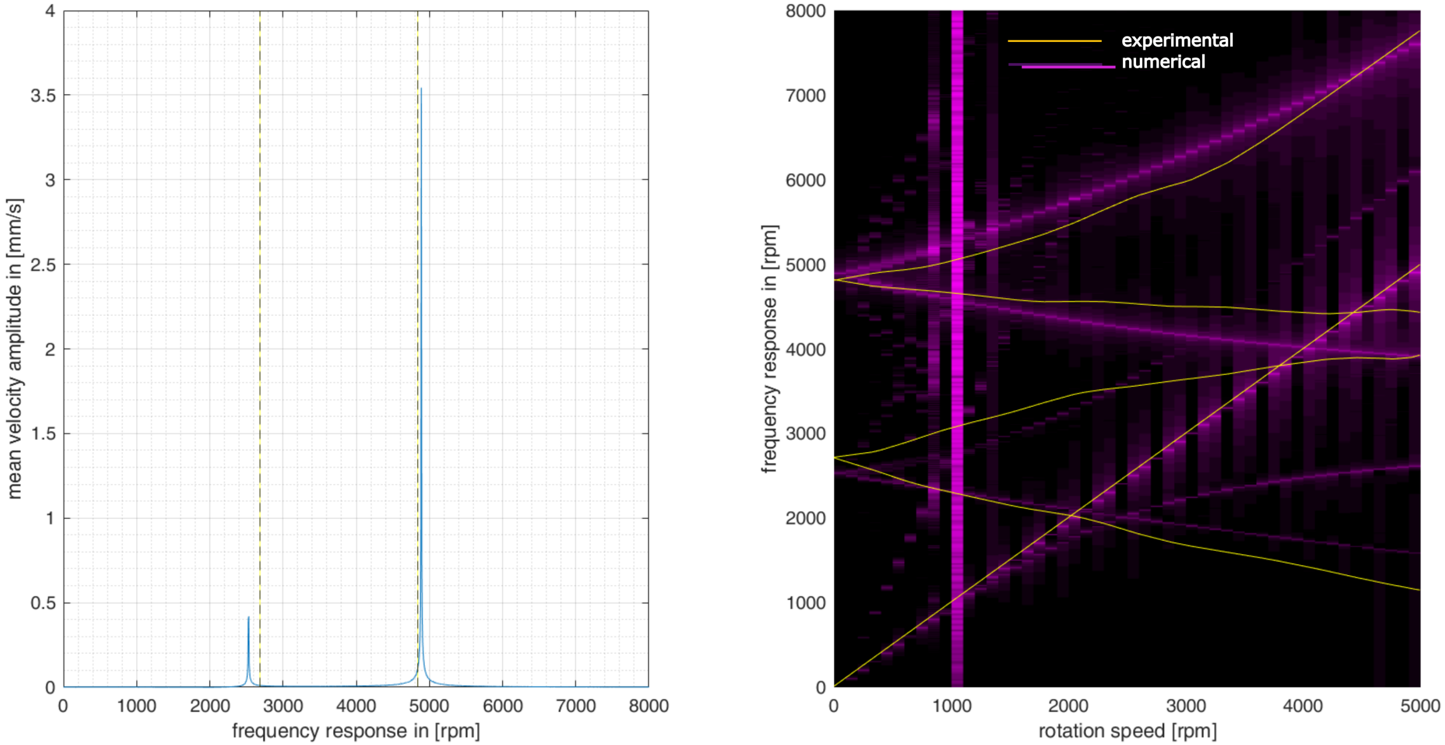

Figure A.9: Campbell-diagrams obtained from model (D).

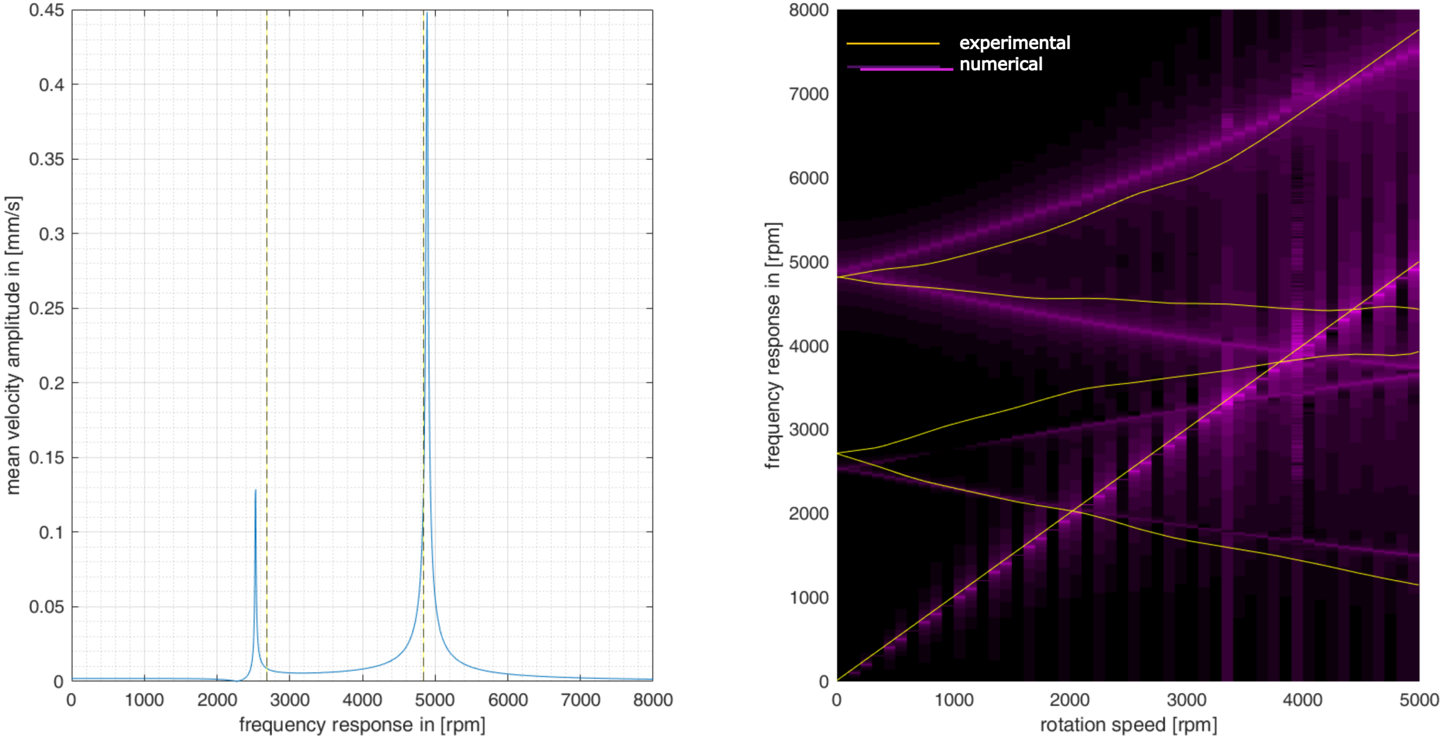

Figure A.10: Campbell-diagrams obtained from model (E).

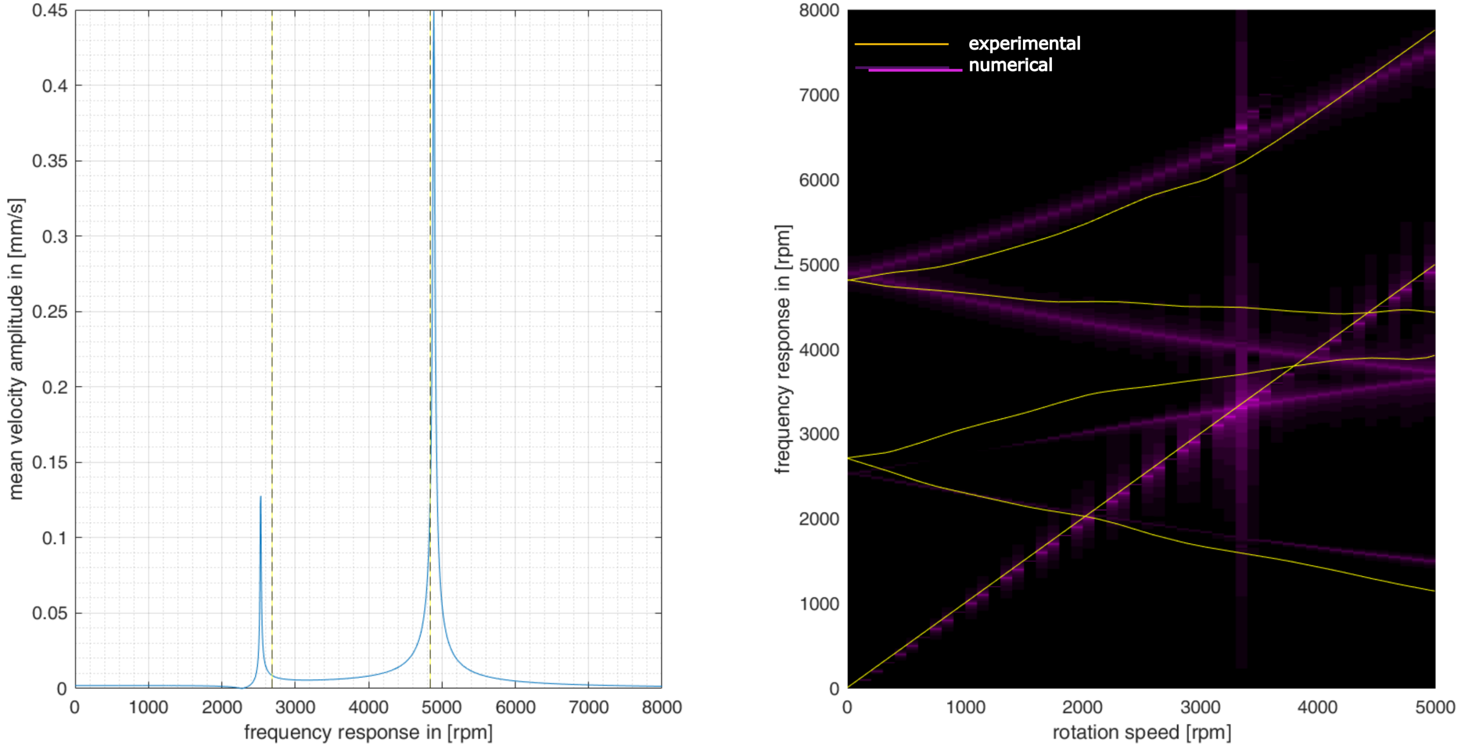

Figure A.11: Campbell-diagrams obtained from model (F).

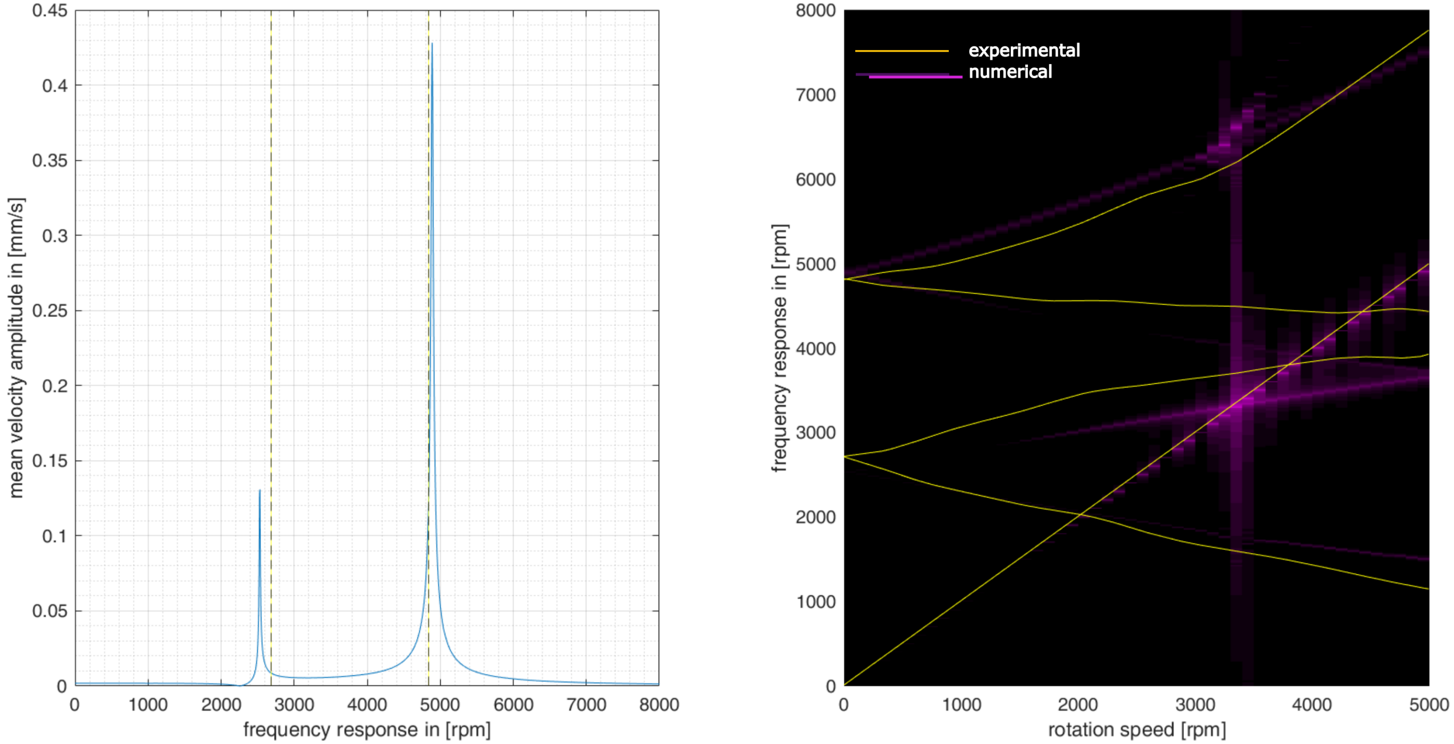

Figure A.12: Campbell-diagrams obtained from model (G).

n (rpm)	Experimental	A, B	C	D	E	F	G
100	-0.000006	-0.000043	0.000044	-0.000044	-0.000043	0.000149	0.000148
300	-0.000016	-0.000043	0.000043	-0.000043	-0.000043	0.000148	0.000149
500	-0.000029	-0.000044	0.000043	-0.000043	-0.000044	0.000146	0.000148
700	0.000001	-0.000043	0.000043	-0.000043	-0.000043	0.000144	0.000147
900	-0.000039	-0.000043	0.000043	-0.000043	-0.000043	0.000141	0.000146
1100	-0.000001	-0.000043	0.000043	-0.000043	-0.000043	0.000138	0.000145
1300	-0.000010	-0.000043	0.000043	-0.000043	-0.000043	0.000133	0.000144
1500	-0.000035	-0.000043	0.000043	-0.000043	-0.000043	0.000128	0.000142
1700	-0.000007	-0.000044	0.000043	-0.000043	-0.000043	0.000123	0.000141
1900	-0.000012	-0.000043	0.000043	-0.000043	-0.000043	0.000116	0.000139
2100	-0.000013	-0.000043	0.000043	-0.000043	-0.000043	0.000109	0.000137
2300	-0.000017	-0.000043	0.000043	-0.000043	-0.000043	0.000101	0.000135
2500	-0.000030	-0.000044	0.000043	-0.000043	-0.000043	0.000093	0.000133
2700	-0.000011	-0.000043	0.000043	-0.000043	-0.000043	0.000083	0.000131
2900	-0.000004	-0.000044	0.000043	-0.000043	-0.000043	0.000073	0.000129
3100	-0.000040	-0.000044	0.000043	-0.000043	-0.000043	0.000063	0.000127
3300	-0.000016	-0.000043	0.000043	-0.000043	-0.000043	0.000051	0.000124
3500	-0.000026	-0.000043	0.000043	-0.000043	-0.000043	0.000039	0.000122
3700	-0.000035	-0.000043	0.000043	-0.000043	-0.000043	0.000026	0.000120
3900	-0.000049	-0.000043	0.000043	-0.000043	-0.000043	0.000013	0.000117
4100	-0.000028	-0.000043	0.000043	-0.000043	-0.000043	-0.000002	0.000115
4300	0.000021	-0.000043	0.000043	-0.000043	-0.000043	-0.000017	0.000113
4500	-0.000007	-0.000043	0.000043	-0.000043	-0.000043	-0.000033	0.000110
4700	-0.000015	-0.000043	0.000043	-0.000043	-0.000043	-0.000054	0.000108
4900	-0.000033	-0.000043	0.000043	-0.000043	-0.000043	-0.000068	0.000106
5100	-0.000059	-0.000044	0.000043	-0.000043	-0.000043	-0.000084	0.000103
5300	-0.000004	-0.000043	0.000043	-0.000043	-0.000043	-0.000103	0.000101
5500	-0.000047	-0.000044	0.000043	-0.000043	-0.000043	-0.000122	0.000099
5700	-0.000047	-0.000043	0.000043	-0.000043	-0.000043	-0.000142	0.000097
5900	-0.000016	-0.000044	0.000043	-0.000043	-0.000043	-0.000162	0.000095

Table A.1: Mean displacements (m) at the front-edge along x-axis

n (rpm)	Experimental	A, B	C	D	E	F	G
100	-0.000020	-0.000043	-0.000010	0.000010	0.000010	-0.000004	-0.000002
300	-0.000015	-0.000043	-0.000010	0.000010	0.000009	-0.000003	-0.000007
500	-0.000025	-0.000044	-0.000010	0.000010	0.000007	-0.000001	-0.000004
700	-0.000012	-0.000043	-0.000010	0.000010	0.000006	0.000003	-0.000004
900	-0.000002	-0.000043	-0.000010	0.000010	0.000003	0.000007	-0.000004
1100	-0.000002	-0.000043	-0.000010	0.000010	-0.000000	0.000013	-0.000004
1300	-0.000016	-0.000043	-0.000010	0.000010	-0.000004	0.000019	-0.000004
1500	-0.000020	-0.000043	-0.000010	0.000010	-0.000009	0.000027	-0.000004
1700	-0.000019	-0.000044	-0.000010	0.000010	-0.000014	0.000036	-0.000004
1900	-0.000003	-0.000043	-0.000010	0.000010	-0.000020	0.000046	-0.000004
2100	-0.000025	-0.000043	-0.000010	0.000010	-0.000027	0.000057	-0.000004
2300	-0.000016	-0.000043	-0.000010	0.000010	-0.000035	0.000070	-0.000003
2500	-0.000019	-0.000044	-0.000010	0.000010	-0.000043	0.000083	-0.000003
2700	-0.000022	-0.000043	-0.000010	0.000010	-0.000051	0.000098	-0.000003
2900	-0.000021	-0.000044	-0.000010	0.000010	-0.000061	0.000114	-0.000003
3100	0.000002	-0.000044	-0.000010	0.000010	-0.000071	0.000130	-0.000003
3300	-0.000018	-0.000043	-0.000010	0.000010	-0.000082	0.000148	-0.000002
3500	-0.000054	-0.000043	-0.000010	0.000010	-0.000093	0.000167	-0.000002
3700	-0.000041	-0.000043	-0.000010	0.000010	-0.000105	0.000187	-0.000002
3900	-0.000045	-0.000043	-0.000010	0.000010	-0.000118	0.000209	-0.000002
4100	-0.000032	-0.000043	-0.000010	0.000010	-0.000131	0.000231	-0.000002
4300	0.000008	-0.000043	-0.000010	0.000010	-0.000145	0.000255	-0.000002
4500	0.000021	-0.000043	-0.000010	0.000010	-0.000160	0.000279	-0.000001
4700	0.000023	-0.000043	-0.000010	0.000010	-0.000176	0.000304	-0.000001
4900	0.000026	-0.000043	-0.000010	0.000010	-0.000192	0.000331	-0.000001
5100	0.000035	-0.000044	-0.000010	0.000010	-0.000209	0.000360	-0.000001
5300	0.000024	-0.000043	-0.000010	0.000010	-0.000226	0.000389	-0.000001
5500	-0.000011	-0.000044	-0.000010	0.000010	-0.000244	0.000419	-0.000001
5700	-0.000006	-0.000043	-0.000010	0.000010	-0.000263	0.000451	-0.000000
5900	-0.000037	-0.000044	-0.000010	0.000010	-0.000283	0.000483	-0.000000

Table A.2: Mean displacements (m) at the front-edge along y-axis

n (rpm)	Experimental	A, B	C	D	E	F	G
100	0.000085	0.000044	0.000045	0.000060	0.000060	0.000060	0.000148
300	0.000085	0.000044	0.000045	0.000060	0.000060	0.000059	0.000149
500	0.000086	0.000044	0.000045	0.000060	0.000060	0.000059	0.000148
700	0.000087	0.000044	0.000045	0.000060	0.000060	0.000058	0.000147
900	0.000085	0.000044	0.000045	0.000060	0.000060	0.000056	0.000146
1100	0.000086	0.000044	0.000045	0.000060	0.000060	0.000055	0.000145
1300	0.000085	0.000044	0.000045	0.000060	0.000060	0.000053	0.000144
1500	0.000085	0.000044	0.000045	0.000060	0.000060	0.000050	0.000142
1700	0.000084	0.000044	0.000045	0.000060	0.000060	0.000047	0.000141
1900	0.000083	0.000044	0.000045	0.000060	0.000060	0.000044	0.000139
2100	0.000087	0.000044	0.000045	0.000060	0.000060	0.000041	0.000137
2300	0.000089	0.000044	0.000045	0.000060	0.000060	0.000037	0.000135
2500	0.000075	0.000044	0.000045	0.000060	0.000060	0.000033	0.000133
2700	0.000088	0.000044	0.000045	0.000060	0.000060	0.000028	0.000131
2900	0.000086	0.000044	0.000045	0.000060	0.000060	0.000024	0.000129
3100	0.000083	0.000044	0.000045	0.000060	0.000060	0.000018	0.000127
3300	0.000076	0.000044	0.000045	0.000060	0.000060	0.000013	0.000124
3500	0.000081	0.000044	0.000046	0.000060	0.000060	0.000007	0.000122
3700	0.000080	0.000044	0.000045	0.000060	0.000060	0.000001	0.000120
3900	0.000074	0.000044	0.000045	0.000060	0.000060	-0.000006	0.000117
4100	0.000066	0.000044	0.000045	0.000060	0.000060	-0.000013	0.000115
4300	0.000077	0.000044	0.000045	0.000060	0.000060	-0.000020	0.000113
4500	0.000062	0.000044	0.000045	0.000060	0.000060	-0.000028	0.000110
4700	0.000072	0.000044	0.000045	0.000060	0.000060	-0.000037	0.000108
4900	0.000071	0.000044	0.000045	0.000060	0.000060	-0.000044	0.000106
5100	0.000063	0.000044	0.000045	0.000060	0.000060	-0.000052	0.000103
5300	0.000083	0.000044	0.000045	0.000060	0.000060	-0.000061	0.000101
5500	0.000085	0.000044	0.000045	0.000060	0.000060	-0.000070	0.000099
5700	0.000096	0.000044	0.000045	0.000060	0.000060	-0.000080	0.000097
5900	0.000088	0.000044	0.000045	0.000060	0.000060	-0.000090	0.000095

Table A.3: Mean displacements (m) at the back-edge along x-axis

n (rpm)	Experimental	A, B	C	D	E	F	G
100	-0.000043	0.000003	0.000003	0.000002	0.000002	0.000002	0.000004
300	-0.000043	0.000003	0.000003	0.000002	0.000003	0.000003	0.000003
500	-0.000044	0.000003	0.000003	0.000002	0.000003	0.000003	0.000003
700	-0.000045	0.000003	0.000003	0.000002	0.000004	0.000004	0.000003
900	-0.000044	0.000003	0.000003	0.000002	0.000005	0.000005	0.000003
1100	-0.000045	0.000003	0.000003	0.000002	0.000007	0.000007	0.000003
1300	-0.000045	0.000003	0.000003	0.000002	0.000008	0.000008	0.000003
1500	-0.000044	0.000003	0.000003	0.000002	0.000010	0.000010	0.000003
1700	-0.000045	0.000003	0.000003	0.000002	0.000013	0.000013	0.000003
1900	-0.000044	0.000003	0.000003	0.000002	0.000015	0.000015	0.000003
2100	-0.000044	0.000003	0.000003	0.000002	0.000018	0.000018	0.000003
2300	-0.000045	0.000003	0.000003	0.000002	0.000022	0.000022	0.000004
2500	-0.000029	0.000003	0.000003	0.000002	0.000025	0.000025	0.000004
2700	-0.000043	0.000003	0.000003	0.000002	0.000029	0.000029	0.000004
2900	-0.000038	0.000003	0.000003	0.000002	0.000033	0.000033	0.000004
3100	-0.000028	0.000003	0.000003	0.000002	0.000037	0.000037	0.000004
3300	-0.000035	0.000003	0.000003	0.000002	0.000042	0.000042	0.000004
3500	-0.000027	0.000003	0.000003	0.000002	0.000047	0.000047	0.000004
3700	-0.000022	0.000003	0.000003	0.000002	0.000052	0.000052	0.000004
3900	0.000008	0.000003	0.000003	0.000002	0.000058	0.000058	0.000004
4100	0.000021	0.000003	0.000003	0.000002	0.000064	0.000064	0.000004
4300	0.000021	0.000003	0.000003	0.000002	0.000070	0.000070	0.000004
4500	0.000051	0.000003	0.000003	0.000002	0.000076	0.000076	0.000004
4700	0.000036	0.000003	0.000003	0.000002	0.000083	0.000082	0.000004
4900	0.000040	0.000003	0.000003	0.000002	0.000090	0.000090	0.000004
5100	0.000046	0.000003	0.000003	0.000002	0.000097	0.000097	0.000004
5300	-0.000035	0.000003	0.000003	0.000002	0.000105	0.000105	0.000004
5500	-0.000027	0.000003	0.000003	0.000002	0.000112	0.000112	0.000004
5700	-0.000029	0.000004	0.000003	0.000002	0.000121	0.000121	0.000004
5900	-0.000043	0.000003	0.000003	0.000002	0.000129	0.000129	0.000004

Table A.4: Mean displacements (m) at the back-edge along y-axis

n (rpm)	Experimental	A, B	C	D	E	F	G
100	0.000111	0.000148	0.000149	0.000243	0.000149	0.000232	0.000526
300	0.000113	0.000149	0.000150	0.000232	0.000149	0.000232	0.000529
500	0.000119	0.000149	0.000153	0.000235	0.000149	0.000231	0.000535
700	0.000094	0.000151	0.000158	0.000252	0.000150	0.000231	0.000543
900	0.000112	0.000153	0.000165	0.000251	0.000151	0.000230	0.000556
1100	0.000089	0.000158	0.000176	0.000257	0.000152	0.000230	0.000573
1300	0.000090	0.000168	0.000194	0.000241	0.000154	0.000231	0.000594
1500	0.000105	0.000188	0.000229	0.000233	0.000156	0.000234	0.000622
1700	0.000098	0.000245	0.000328	0.000241	0.000159	0.000241	0.000657
1900	0.000505	0.000504	0.000514	0.000255	0.000163	0.000258	0.000701
2100	0.000126	0.000271	0.000097	0.000264	0.000167	0.000304	0.000756
2300	0.000581	0.000209	0.000083	0.000268	0.000171	0.000533	0.000823
2500	0.000478	0.000185	0.000116	0.000268	0.000174	0.000305	0.000899
2700	0.000106	0.000173	0.000143	0.000264	0.000174	0.000161	0.000973
2900	0.000152	0.000164	0.000168	0.000266	0.000170	0.000143	0.001022
3100	0.000282	0.000156	0.000196	0.000267	0.000165	0.000170	0.001017
3300	0.000261	0.000150	0.000231	0.000286	0.000182	0.000193	0.000952
3500	0.000245	0.000144	0.000277	0.000362	0.000223	0.000217	0.000855
3700	0.000245	0.000139	0.000345	0.000384	0.000264	0.000242	0.000755
3900	0.000240	0.000158	0.000453	0.000384	0.000297	0.000270	0.000665
4100	0.000238	0.000193	0.000651	0.000416	0.000455	0.000302	0.000591
4300	0.000318	0.000255	0.001023	0.000446	0.000351	0.000343	0.000531
4500	0.000519	0.000293	0.001202	0.000474	0.000377	0.000404	0.000483
4700	0.000446	0.000262	0.000821	0.000501	0.000403	0.000503	0.000443
4900	0.000471	0.000232	0.000568	0.000527	0.000429	0.000427	0.000411
5100	0.000567	0.000214	0.000435	0.000551	0.000455	0.000399	0.000384
5300	0.000535	0.000202	0.000356	0.000572	0.000483	0.000417	0.000361
5500	0.000482	0.000193	0.000304	0.000593	0.000512	0.000453	0.000342
5700	0.000433	0.000187	0.000269	0.000612	0.000541	0.000493	0.000326
5900	0.000355	0.000182	0.000242	0.000629	0.000572	0.000534	0.000311

Table A.5: Maximum displacements (m) at front-edge

	Experimental	A, B	C	D	E	F	G
100	0.000132	0.000063	0.000063	0.000063	0.000063	0.000063	0.000128
300	0.000133	0.000063	0.000063	0.000066	0.000064	0.000063	0.000129
500	0.000135	0.000063	0.000063	0.000076	0.000065	0.000062	0.000131
700	0.000157	0.000062	0.000063	0.000091	0.000066	0.000062	0.000134
900	0.000124	0.000062	0.000062	0.000113	0.000068	0.000061	0.000138
1100	0.000130	0.000061	0.000061	0.000123	0.000071	0.000059	0.000144
1300	0.000125	0.000062	0.000058	0.000125	0.000074	0.000058	0.000151
1500	0.000121	0.000065	0.000052	0.000124	0.000078	0.000055	0.000161
1700	0.000134	0.000079	0.000077	0.000124	0.000083	0.000053	0.000173
1900	0.000135	0.000153	0.000241	0.000123	0.000089	0.000050	0.000188
2100	0.000193	0.000093	0.000145	0.000124	0.000096	0.000060	0.000208
2300	0.000278	0.000077	0.000129	0.000127	0.000104	0.000138	0.000232
2500	0.000409	0.000076	0.000128	0.000130	0.000114	0.000152	0.000260
2700	0.000260	0.000082	0.000133	0.000135	0.000126	0.000111	0.000289
2900	0.000279	0.000096	0.000142	0.000140	0.000140	0.000106	0.000312
3100	0.000374	0.000122	0.000156	0.000147	0.000156	0.000110	0.000320
3300	0.000389	0.000176	0.000175	0.000153	0.000172	0.000121	0.000309
3500	0.000406	0.000305	0.000204	0.000160	0.000183	0.000138	0.000285
3700	0.000416	0.000412	0.000248	0.000168	0.000188	0.000162	0.000258
3900	0.000454	0.000298	0.000320	0.000176	0.000192	0.000198	0.000233
4100	0.000475	0.000256	0.000453	0.000185	0.000209	0.000253	0.000212
4300	0.000460	0.000259	0.000707	0.000194	0.000205	0.000352	0.000194
4500	0.000476	0.000247	0.000834	0.000204	0.000214	0.000573	0.000179
4700	0.000485	0.000203	0.000579	0.000214	0.000226	0.001139	0.000167
4900	0.000474	0.000172	0.000409	0.000225	0.000239	0.000803	0.000156
5100	0.000444	0.000154	0.000319	0.000235	0.000254	0.000502	0.000148
5300	0.000425	0.000142	0.000266	0.000247	0.000269	0.000394	0.000140
5500	0.000393	0.000134	0.000232	0.000258	0.000286	0.000344	0.000134
5700	0.000410	0.000128	0.000208	0.000270	0.000304	0.000320	0.000128
5900	0.000357	0.000123	0.000190	0.000283	0.000323	0.000309	0.000123

Table A.6: Maximum displacements (m) at the back-edge

The Bond-graph (20-sim) rotor models as well as the relevant results data are also provided digitally.

Structure of the digitally provided data

VADmodel_A.emx
VADmodel_B.emx
VADmodel_C.emx
VADmodel_D.emx
VADmodel_E.emx
VADmodel_F.emx
VADmodel_G.emx

BackEdge_max_amplitudes.xlsx
BackEdge_mean_x.xlsx
BackEdge_mean_y.xlsx
FrontEdge_max_amplitudes.xlsx
FrontEdge_mean_x.xlsx
FrontEdge_mean_y.xlsx

Raw data files.

Eidesstattliche Versicherung

Ich versichere eidesstattlich durch eigenhändige Unterschrift, dass ich die Arbeit selbständig und ohne Benutzung anderer als der angegebenen Hilfsmittel angefertigt habe.

Alle Stellen, die wörtlich oder sinngemäß aus Veröffentlichungen entnommen sind, habe ich durch Angaben der Herkunft kenntlich gemacht. Dies gilt auch für Zeichnungen, Skizzen, bildliche Darstellungen sowie für Quellen aus dem Internet.

Ich erkläre ferner, dass ich die vorliegende Arbeit in keinem anderen Prüfungsverfahren als Prüfungsarbeit eingereicht habe oder einreichen werde.

Die eingereichte schriftliche Fassung ist identisch mit der elektronisch eingereichten Fassung.

Ich weiß, dass bei Abgabe einer falschen Versicherung die Prüfung als nicht bestanden zu gelten hat.

Rostock am ………………….. ____

(Abgabe Termin) Unterschrift (Vor- und Zuname)